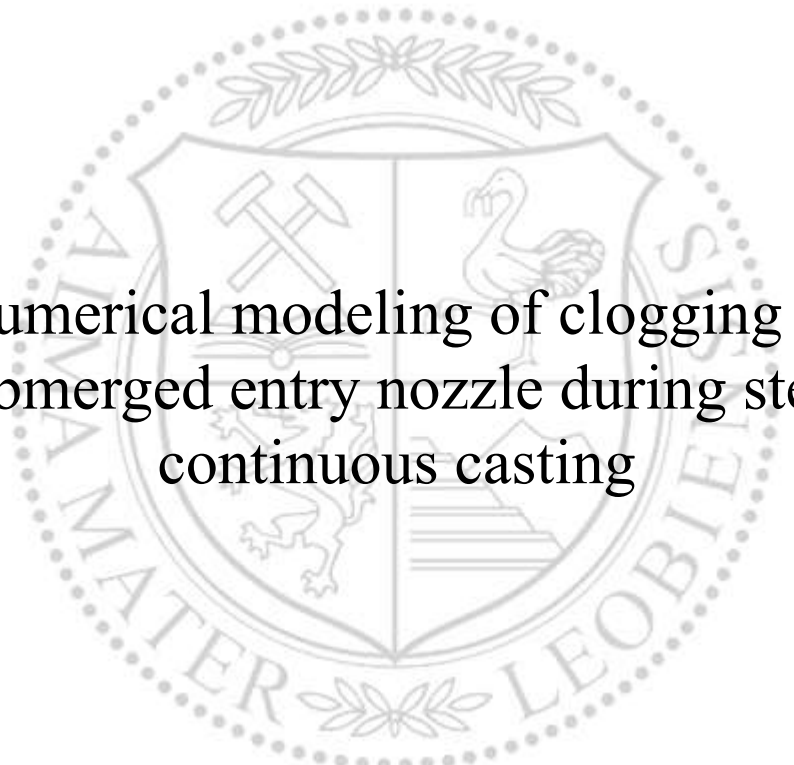Chair of Simulation and Modelling of Metallurgical Processes

Doctoral Thesis

Numerical modeling of clogging in submerged entry nozzle during steel continuous casting

Hadi Barati, Lis. Fogh-lis.

November 2018

MONTANUNIVERSITÄT LEOBEN
www.unileoben.ac.at

AFFIDAVIT

I declare on oath that I wrote this thesis independently, did not use other than the specified sources and aids, and did not otherwise use any unauthorized aids.

I declare that I have read, understood, and complied with the guidelines of the senate of the Montanuniversität Leoben for "Good Scientific Practice".

Furthermore, I declare that the electronic and printed version of the submitted thesis are identical, both, formally and with regard to content.

Datum 26.11.2018

Signature Author
Hadi, Barati
Matriculation Number: 01535615

Acknowledgements

Kurzfassung

Im Rahmen dieser Arbeit wurde ein numerisches Modell für den transienten Verstopfungsprozess („Clogging") durch nichtmetallische Einschlüsse (NME) im Eintauchausguss (ETA) während des Stranggießens entwickelt. Die folgenden drei Hauptschritte des Cloggings wurden berücksichtigt: (a) Transport von nichtmetallischen Einschlüssen durch turbulenten Schmelzfluss in Richtung der ETA-Wand; (b) Wechselwirkungen zwischen Schmelze und Wand und die Adhäsion des NME an der Wand; (c) Bildung und Wachstum der Verstopfung durch NME-Abscheidung. Die Strömung wurde für Regionen nahe und fern (Bulk-Region) der Wand unterschiedlich behandelt. Ein Euler-Lagrange-Ansatz wurde verwendet, um den Transport von NMEs durch die turbulente Strömung (Bulk-Region) zu berechnen; ein stochastisches Wandmodell wurde verwendet, um Partikel in der turbulenten Grenzschicht (nahe der Wand) zu verfolgen. Das Anfangsstadium des Cloggings wurde durch die dynamische Veränderung der Wandrauheit modelliert, während das spätere Stadium der Verstopfung durch Aufbauschichten von abgeschiedenen nichtmetallischen-Partikeln in poröser Struktur modelliert wurde. Diese poröse Struktur wird als "Verstopfung"bzw. „Clogging-Ansatz" bezeichnet, und sie wächst weiter, indem sich mehr NME-Partikel anhaften.

Um das Modell zu validieren, wurde ein Laborversuch simuliert [Janis et al., Steel Res. Int. 86 (2015) 1271-1278], welcher entwickelt wurde, um das Verstopfen von SEN während des Stranggießens von Stahl zu untersuchen. Es wurde nachgewiesen, dass das Modell das Experiment reproduzieren kann; der berechnete verstopfte Abschnitt der Düse ist qualitativ mit den verstopften Abschnitten in Laborexperimenten vergleichbar und der berechnete Massendurchsatz durch die Düse stimmt auch mit dem experimentell gemessenen überein.

Folgende neue Erkenntnisse konnten gewonnen werden: (1) Das Verstopfen des ETAs ist ein vorübergehender Prozess, der mit dem Schmelzfluss zusammenwirkt; und es umfasst das anfängliche Ablagern von nichtmetallischen Partikeln an der Düsenwand, die Entwicklung einer gewölbten Verstopfungsfront und dann die Entwicklung einer verzweigten Struktur. (2) Das Verstopfen des ETAs ist ein stochastischer und sich selbst beschleunigender Prozess.

Darüber hinaus wurden Unsicherheiten für die Wahl der Modellierungsparameter wie Maschenweite, Lagrange-Zeitskala (T_L) und Korrekturfaktor (n) bei der Interpolation der Verstopfung untersucht. Eine Maschenweite von weniger als 0,1 mm im wandnahen Bereich wurde empfohlen, um netzunabhängige Ergebnisse zu erhalten; Das Modellierungsergebnis der Partikelablagerung wird gegenüber T_L und n unempfindlich, wenn sie nahe an 6 µs bzw. 5 gesetzt werden.

Das Modell wurde auch für den Industrieprozess des Stranggießens von Stahl unter Berücksichtigung der Modellgenauigkeit und Berechnungseffizienz bewertet. Für die komplexe Geometrie des Eintauchausgusses, bei der es nicht möglich ist, eine Hexaeder-Vernetzung in der gesamten Domäne zu erzeugen, wurde ein Mischgittertyp empfohlen, d. h. eine Keil-Vernetzung für Bereiche neben ETA-Wänden und eine Tetraeder-Vernetzung für Innenbereiche. Eine weitere Herausforderung bei der Berechnung von echten ETA-Verstopfungen ist die große Anzahl von Partikeln, die in dem Industrieprozess involviert sind. Ein künstlicher N-Faktor, wobei N die Anzahl der NMIs ist, die jedes Partikel des Lagrange-Frames darstellt, muss eingeführt werden, um die Berechnungszeiten bzw. -kosten zu reduzieren. Ein zu großer N-Faktor führt zu einem Berechnungsfehler. Daher wurde ein Kriterium definiert, um den N-Faktor zu begrenzen und die Modellierungsgenauigkeit sicherzustellen.

Da die Erstarrung der Stahlschmelze infolge der Abkühlung an der ETA-Wand ebenfalls als möglicher Verstopfungsmechanismus angesehen wurde, wurde das Modell für die nicht-

isothermischen Bedingungen angepasst. Die Modellierungsergebnisse zeigen, dass keine Erstarrung im SEN auftreten sollte, wenn der geschmolzene Stahl eine ausreichende Überhitzung aufweist und mit relativ hoher Geschwindigkeit durch den SEN fließt. Ein Verstopfen fördert jedoch die Erstarrung innerhalb der porösen Ablagerungen.

Schließlich wurden die Fähigkeiten des aktuellen Modells hinsichtlich numerischer und praktischer Gesichtspunkte diskutiert. Ebenso wurden Verbesserungsmöglichkeiten aufgezeigt, welche für die zukünftige Weiterentwicklung des Modells von großer Bedeutung sind.

Abstract

The main objective of this PhD thesis is to develop a numerical model for the transient clogging process in submerged entry nozzle (SEN) during continuous casting. Three major steps of the clogging have been taken into account: (a) transport of non-metallic inclusions (NMIs) by turbulent melt flow towards the SEN wall; (b) interactions between melt and wall, and the adhesion of the NMI on the wall; (c) formation and growth of the clog by NMI deposition. The flow domain is treated differently for the bulk and near-wall regions. An Eulerian-Lagrangian approach is employed to calculate the transport of NMIs by the turbulent flow (bulk region); a stochastic near-wall model is adopted to trace particles in the turbulent boundary layer (near-wall region). The early stage of clogging is modeled by the dynamical change in wall roughness, while the late stage of the clogging is modeled by building layers deposited NMI particles in porous structure. This porous structure is called as 'clog', and it continues to grow by attaching more NMI particles.

To evaluate the model, a laboratory experiment [Janis et al., Steel Res. Int. 86 (2015) 1271–1278], which was designed to study the clogging of SEN during steel continuous casting, is simulated. It is verified that the model can reproduce the experiment: the calculated clogged section of the nozzle is qualitatively comparable with as-clogged sections in laboratory experiments; the calculated mass flow rate through the nozzle agrees with the experimentally-monitored one as well.

New knowledge is obtained. (1) Clogging is a transient process interacting with the melt flow; and it includes the initial coverage of the nozzle wall with deposited particles, the evolution of a bulged clog front, and then the development of a branched structure. (2) Clogging is a stochastic and self-accelerating process.

Moreover, uncertainties for choosing the modeling parameters such as mesh size, Lagrangian time scale (T_L), the correction factor (n) in the interpolation of clog permeability are studied and discussed. Mesh size smaller than 0.1 mm in the near-wall region is recommended to have mesh independent results; the modeling result on particle deposition becomes insensitive to T_L and n when they are set at close to 6 μs and 5, respectively.

The model is also evaluated for the industry process of continuous casting of steel, referring to the model accuracy and calculation efficiency. For the complex geometry of submerged entry nozzle (SEN), where it is not possible to create hexahedron mesh in the whole domain, a mixed mesh type is recommended, i.e. the wedge mesh for regions adjacent to SEN walls and the tetrahedron mesh for inner regions. Another challenge to the calculation of real SEN clogging is the huge number of particles as involved in the industry process. An artificial N-factor, where N is the number of NMIs each particle of Lagrangian frame represents, has to be introduced to reduce the calculation cost. A too large N-factor leads to calculation error. Therefore, a criterion is defined to limit the N-factor and ensure the modeling accuracy.

As solidification of the steel melt on the SEN wall is also considered as a possible mechanism for clogging, the model is upgraded to be applicable for the non-isothermal conditions. The modeling results indicate that solidification should not occur in a SEN if the molten steel has sufficient superheat and it flows with relatively high speed through the SEN. However, clogging promotes the solidification inside the porous structure of clog.

Finally, capabilities of the current state of the model from the numerical and practical point of views are discussed; the missing features or the functionalities which need future improvements are addressed.

Contents

Nomenclature

Symbol	Unit	Meaning
C_μ	-	turbulence constant
C_D	-	drag coefficient
D_ω	kg/(m^2.s^2)	cross-diffusion term of ω
D_{pore}	m	pore diameter in clog
d_p	m	diameter of particle
$\vec{F}_B$	kg.m/s^2	buoyancy force
$\vec{F}_D$	kg.m/s^2	drag force
$\vec{F}_L$	kg.m/s^2	lift force
$\vec{F}_{press}$	kg.m/s^2	pressure gradient force
$\vec{F}_{VM}$	kg.m/s^2	virtual mass force
f_{clog}	-	volume fraction of clog
f_l	-	volume fraction of liquid metal
f_p	-	volume fraction of solid particles
$\bar{f}_p$	-	average volume fraction of solid particles
f_s	-	volume fraction of solid metal
G	1/s	local velocity gradients
$\tilde{G}_k$	kg/(m.s^3)	generation of turbulence kinetic energy for k
G_ω	kg/(m^2.s^2)	generation of turbulence kinetic energy for ω
$\vec{g}$	m/s^2	Gravity
h	J/kg	enthaply
J	-	correction factor of the lift force

K	m/s$^{3/2}$	diffusion coefficient
K_{Br}	m/s$^{3/2}$	velocity diffusion term
K_{per}	m^2	Permeability
K_{s}	m	physical roughness height
K_{s}^{+}	-	non-dimensional roughness height
k	m^2/s^2	turbulence kinetic energy
m_{p}	kg	mass of particle
n	-	interpolation correction power
p	Pa	pressure of fluid
R_{a}	m	arithmetic average of distances from the average height
$\mathrm{Re_P}$	-	particle Reynolds number
S	-	parent process for stochastic model
S_k	kg/(m.s^3)	source term due to porous medium of clog for k
S_{ω}	kg/(m^2.s^2)	source term due to porous medium of clog for ω
$\vec{S}_u$	kg/(m^2.s^2)	source term due to porous medium of clog for $\vec{u}$
T_{L}	s	Lagrangian time scale
Th_{clog}	m	thickness of clog
t	s	Time
U_{s}	m/s	difference between instantaneous streamwise velocities for fluid and particle
$\vec{u}$	m/s	time averaged velocity of fluid
$\vec{u'}$	m/s	instantaneous velocity of fluid
$\vec{u}_{\mathrm{p}}$	m/s	velocity of particle
u_{s}	m/s	wall normal velocity of the fluid seen by the particle
u^{*}	m/s	velocity function
ΔV	m^3	volume of cell
W	-	Wiener process

Y_k	kg/(m.s^3)	dissipation of k
Y_ω	kg/(m^2.s^2)	dissipation of ω
α	-	volume dimensionless number
Γ_k	kg/(m.s)	diffusivity for k
Γ_ω	kg/m^2	diffusivity for ω
λ_1	m	primary dendrite arm spacing
μ	kg/(m.s)	viscosity of fluid
ξ	-	Gaussian distributed random number
ρ	kg/m^3	density of fluid
ρ_p	kg/m^3	density of particle
τ_p	s	particle relaxation time
ω	1/s	specific dissipation rate of turbulence kinetic energy

1. Introduction

1.1 Background

In continuous casting of steel, submerged entry nozzle (SEN) transports the molten steel from tundish to the mold. SEN protects the melt from oxidation and stabilizes the casting process. Clogging of SEN describes a phenomenon of the blockage of the flow passage which is due to a gradual build-up of solid materials on the SEN wall. This build-up of solid materials would disturb the fluid flow in the passage before the blockage. SEN clogging is a long-term problem in steel industry. It appears since early 1960s when continuous casting machines were implemented in steel plants. Examples of clean (new) and as-used (partially clogged) SENs from steel plant are shown in Figure 1.1.

Several undesired problems appear by clogging: productivity of the process decreases because of frequent substitution of clogged SENs; quality of the final product is reduced due to the fragmentation of clog material; random nature of SEN clogging leads to asymmetric flow and abnormal temperature distribution in the mold region; slag entrainment in the mold region can occur; stability and predictability of the casting process decrease since clogging sometimes appears randomly; finally, clogging leads to additional operational costs.

Despite of vast works conducted to study mechanisms of clogging in continuous casting, this phenomenon is not fully understood yet.
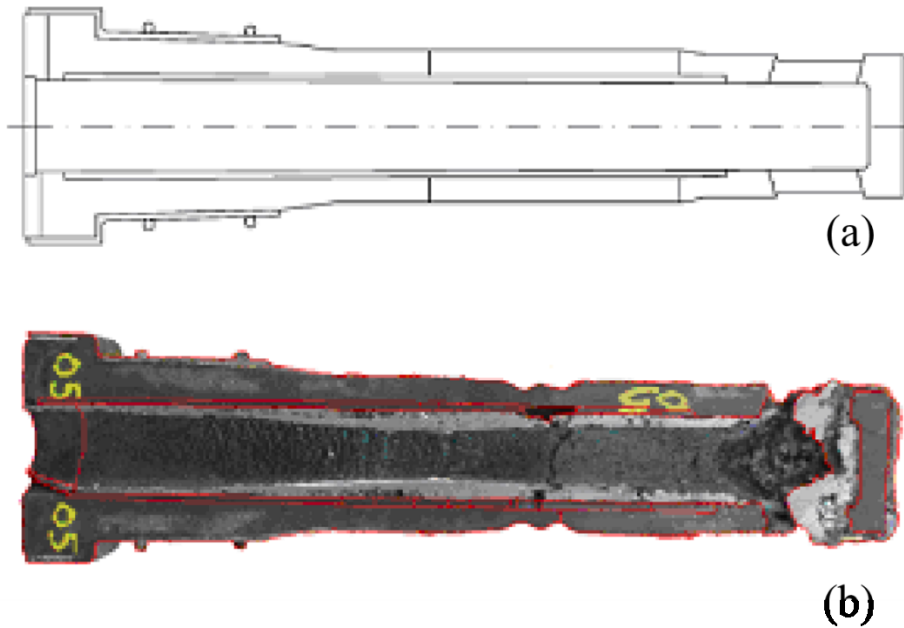
Figure 1.1 Samples of clean (a) and clogged (b) nozzles [1].

Various solutions have been suggested to reduce the clogging problem like argon injection, calcium treatment, improvement of SEN material, modification of SEN design, and apply electric current in SEN. However, none of the aforementioned solutions is known as the final remedy for clogging. SEN clogging is still an important challenge in steel plants.

The melt flow in SEN is multiphase and highly turbulent. Because of high temperature and opaque nature of the melt and the SEN, it is too difficult to study SEN clogging experimentally. Therefore, physical and numerical modeling approaches are vital to understand the melt flow and clogging in SEN.

1.2 Objective

The aim of this PhD thesis is to develop a numerical model for SEN clogging in steel continuous casting. SEN clogging is a complex process involving various phenomena like multiphase flow (steel melt, solid particles and gas bubble), chemical reaction, and possible

solidification. Developing a single model accurately mimics all phenomena is not possible due the high complexity. Another great challenge is different time and length scales for numerical models as suggested for different phenomena during SEN clogging. For example, Lagrangian time scale for non-metallic inclusion (NMI) tracking is in order of microsecond, while the industry process of SEN clogging happens in few hours; the NMI size is in the order of few micrometers, while the SEN diameter is in the order of 10 cm. Moreover, there is lack of knowledge about characteristics and behavior of NMIs in turbulent melt flow during the clogging process.

Therefore, in this research, the clogging phenomenon is divided into main steps and a numerical model is developed step by step to simulate major key features of SEN clogging. In Chapter 2, a state-of-the art overview of SEN clogging is given. Assumptions and simplifications are necessarily made, but they must be justified. Details of the numerical model are presented in Chapter 3. Chapter 4 presents validation of the clogging model against laboratory experimental data. Then, the developed model is tested for the SEN of industry scale in Chapter 5. Capabilities, key features and missing points of the model are discussed in Chapter 6.

2. State of the art

2.1 Continuous casting process

Continuous casting is the most common process in steel production. About 93% of the liquid steel in the world undergoes a continuous casting process. The rest is cast in so-called ingots [2]. In continuous casting process, liquid steel flows from a ladle, through a tundish into the mold, and solidifies into a semi-finished steel product for subsequent production procedure like rolling in the rolling mills. The continuous casting process basically comprises of the following sections.

(a) In the ladle, the melt is taped in and is transferred via a pipe/tube (called shroud) to the tundish.

(b) Tundish is a holding bath located between the ladle and the mold. Tundish receives the steel melt from the ladle and feeds it to the mold at a regulated rate through a submerged entry nozzle (SEN).

(c) In the water-cooled copper mold (primary cooling), a stable solid shell forms, which is sufficiently strong enough to maintain the strand shape.

(d) The secondary cooling is positioned below the mold. Water or water/air mixture is sprayed via nozzles onto the strand surface at high pressure for further solidifying of the steel.

Several interacting phenomena occur in the continuous casting. Figure 2.1(a) depicts some important phenomena in the mold region. The SEN conducts the melt from tundish to the mold region, as shown in Figure 2.1(b). The melt flowing through the SEN contains solid non-metallic inclusions (formed in tundish) and argon bubble (purged on the top of the SEN). Jets of steel melt from the SEN exit-ports carry non-metallic inclusions (NMIs) and bubbles into the mold cavity. A shell solidifies on the mold and is continuously pulled downward by rolls. The mold oscillates vertically to reduce the friction between the mold and the already solidified steel shell. A flux powder covers top of the melt pool (meniscus) and can penetrate as a viscous film in the gap between the solidified shell and the mold. The flux powder is melted in contact with the steel melt. The liquid flux may be entrapped in the melt due to the vortex in the melt flow and forms new liquid non-metallic inclusions. The solid NMIs and argon bubbles, exit from the ports of the SEN, can float up and be captured by covering flux. They also may reach the solidifying shell and be captured by dendrite of the mushy zone of steel.
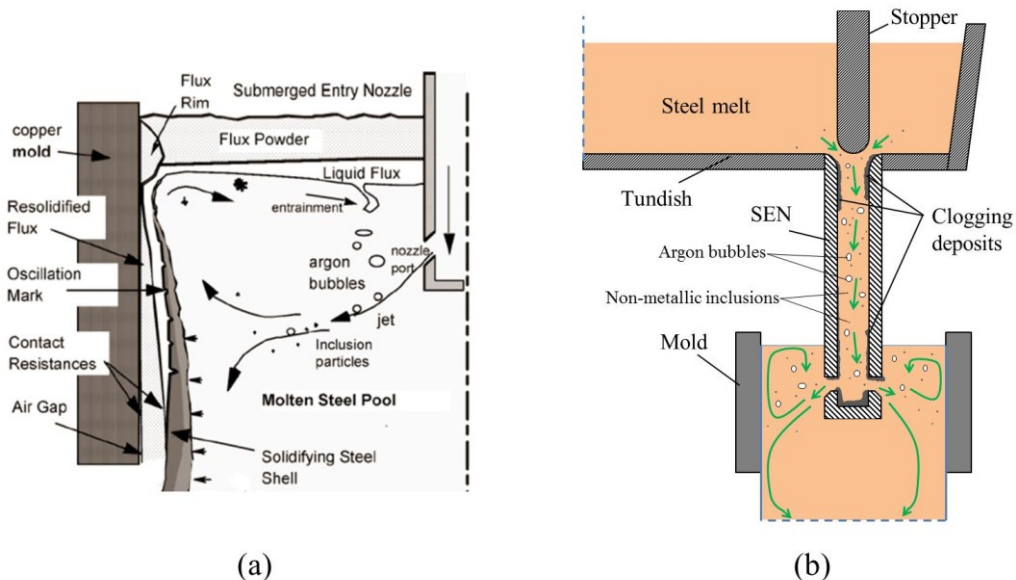
Figure 2.1 Schematic of phenomena (a) in the mold [3] and (b) in the SEN during continuous casting of steel.

2.2 Submerged entry nozzle

Submerged entry nozzle (SEN) conveys the melt from the tundish to the mold; it protects the melt from oxidation and stabilizes the process. The design of the SEN plays very crucial role in determining the flow pattern within the mold. Therefore, design of SEN affects the quality of the final product. Various designs of SEN have been used in steel plants. For example, typical flow controlling systems are shown in Figure 2.2: slide-gate [4–7], stopper rod [3,8–10], and refractory-funnel-nozzle semi-open-pouring [11]. Numerous works have been done to modify SEN with regard to design of exit-ports [5,10,12–16], stopper shape [17], SEN diameter [18], etc.
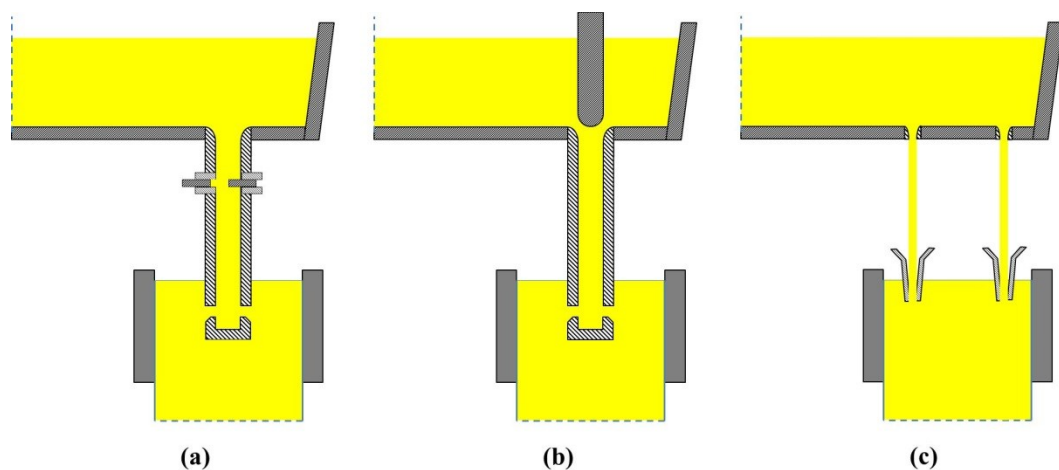
Figure 2.2 Typical SEN designs: (a) slide-gate, (b) stopper rod, and (c) refractory-funnel-nozzle semi-open-pouring.

The melt flow in SEN is complex and highly turbulent. Presence of solid non-metallic inclusions and injection of argon gas in SEN make a multiphase flow in the SEN. Due to the high temperature of steel melt and opaque nature of steel melt and the SEN material, study of the turbulent multiphase flow in the SEN is too difficult. Two approaches are mostly used by researchers to understand the flow pattern in the SEN: water model in transparent vessels [4,17,19–22] and computational fluid dynamics (CFD) [3,6,23–25].

In water model, everything is transparent and it is easy to figure out using particle image velocimetry (PIV) or tracking injected ink in the water. In this approach, Reynolds and Froud numbers of the water model process should be similar to those of the the molten steel during continuous casting. For instance, Ramirez et al. [20] studied 3D flow behavior inside the SEN by the PIV technique and using a 1/3-scale water model. PIV technique allows obtaining different parallel and perpendicular vector fields inside the internal volume without any disturbances in the flow behavior. The technique also allows observing and measuring the internal flow and could characterize the three-dimensional flow pattern inside the SEN. Sometimes, it is difficult to match accurate similarity between water model and casting process. For instance, in studying gas injection into liquid steel additional matching of the gas fraction and its distribution is also required.

In CFD approach, a proper turbulence model should be chosen to achieve reasonable results. Reynolds–Averaged Navier–Stokes (RANS) turbulent models are very popular in simulation of continuous casting. Among RANS models, k-ε model mostly has been utilized [4,5,15,26–29]. This model is easy to implement and is fast in convergence. However, the k–ε model is suitable only to find steady-state flow pattern and transient behavior of the turbulent flow is calculated hardly. Large eddy simulation (LES) models lead to prediction of the transient flow pattern very well but the calculation costs are higher due to fine mesh and small time-step [30]. By improvement of hardware, LES has been used in diverse studies for melt flow in the SEN [3,31–36]. Detached–Eddy Simulation (DES) model, which is a combination of RANS and LES models, is also adopted to simulate melt flow patterns and turbulence inside a SEN [6].

In addition to vertical turbulent flow in the SEN, swirling flow is also of interest [13,37–45]. The swirling flow in the SEN improves penetration depth of the SEN, outlet flow of the SEN, velocity distribution in the mold, and heat and mass transfer near the meniscus [42,45]. Three types of methods are used to produce swirling flow in the SEN: (i)

mechanical rotation [41–45], (ii) electromagnetic force [13,37], and (iii) change in tundish design [39,40].

The flow pattern and pressure distributions in the SEN are very important to steel product quality. The flow in the SEN significantly affects the mold flow and level fluctuations in the mold [17]. Single phase considerations of the flow in the region of the stopper rod result in a low or even negative pressure at the smallest cross-section. This can cause degassing of dissolved gases from the melt, evaporation of alloys, and entrainment of air through the refractory material (also named aspiration) [9]. In Figure 2.3, obtained by solving Bernoulli's equation, pressure is plotted as a function of the vertical coordinate for liquid steel in a SEN for both flow controlling systems slide-gate and stopper rod. In Figure 2.3(b), the pressure at the surface of the tundish is equal to the atmospheric pressure. Then, it rises due to the increasing hydrostatic pressure. Near the bottom of the tundish, the flow acceleration of the fluid causes a pressure drop. It reaches a minimum at the point of the smallest cross-section. Underneath the stopper a free jet forms, which causes the main pressure loss. In the SEN the pressure rises again due to gravity [8,9].

Similarly, in the slide-gate flow controlling system, Figure 2.3(a), the lowest pressure is found in the SEN just beneath the slide gate. If the minimum pressure falls below zero, a cavitation (or degassing) may occur in the SEN [4].
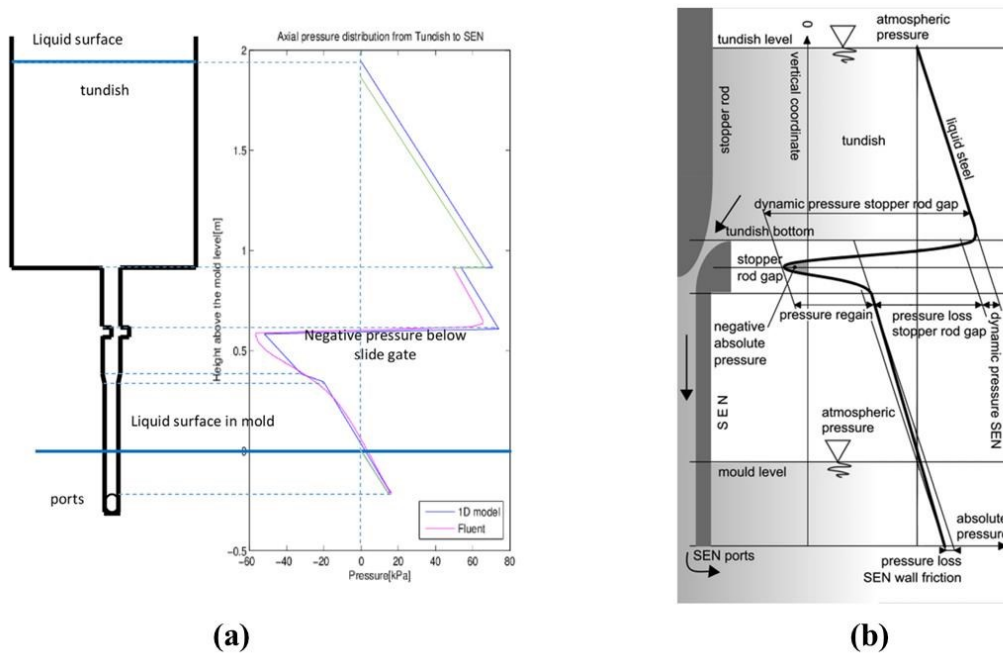
Figure 2.3 Pressure along a streamline from the tundish surface to the exit-ports of the SEN for liquid steel for slide-gate [46] (a) and stopper rod [9] (b) systems.

Argon gas is commonly injected in form of bubbles into the upper region of the SEN to collect non-metallic inclusions. When the argon bubbles enter the mold region, they can float up and be captured by the mold flux. However, some small bubbles may go with the melt flow downward in the mold region. In the slide-gate flow controlling system, argon gas diffuses through the porous medium of the nozzle refractory to exit the inner-bore surface of the SEN, as shown in Figure 2.4(a). Low pressure region below the slide gate can result in air aspiration into the SEN which causes severe reoxidation of the melt. Injection of argon gas increases the pressure in this region and prevents air aspiration [46]. In the stopper rod system, argon gas is typically injected through the tip of the stopper, as shown in Figure 2.4(b).
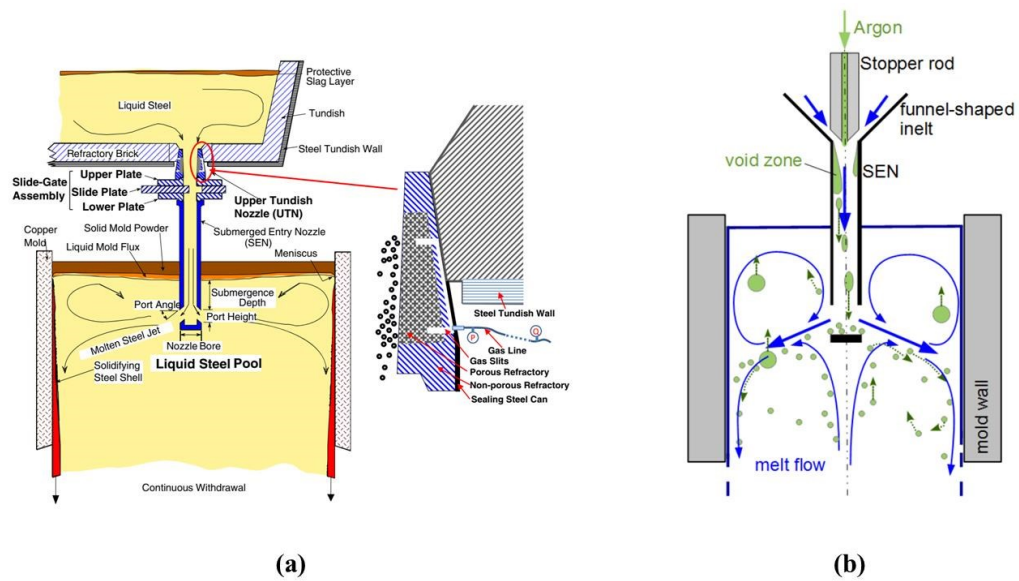
Figure 2.4 Schematic of argon gas injection in (a) slide-gate [47] and (b) stopper rod [48] flow controlling systems.

Argon bubbles exiting the SEN and entering the mold region have three possible destinations: (i) some reach the top surface, pass through the flux layer, and escape harmlessly into the atmosphere; (ii) some are captured near the meniscus and lead to surface defects in final steel product; (iii) some are captured by the solidifying steel shell and cause internal defects since these bubbles usually carry a layer of non-metallic inclusions [49,50]. Many researches have been conducted to study multiphase flow of argon gas, solid inclusions, and steel melt in the SEN and mold region using water models [22,51–54] or computational models [3,4,31,47,49,50,55–57].

The argon gas injection rate influences classic double-roll flow pattern in the mold region [55,56] and oscillations of the meniscus level [22]. To obtain more realistic results of numerical modeling of the multiphase flow, three-dimensional calculation should be performed and two-way coupling between argon bubble and melt flow should be considered, especially in the presence of large gas bubbles [27]. Several efforts have been made to study bubble-bubble interactions [22,58,59], bubble-inclusion interactions [50,60],

bubble/inclusion interactions with solidifying shell [23,27,49,61], and bubble size variation [4,57,62] in steel continuous casting.

2.3 Clogging of submerged entry nozzle (SEN)

2.3.1 Description

Nozzle clogging in continuous casting is a long-term problem which has been subject of discussion since early 1960s when continuous casting machines were implemented in steel plants [63]. Accretion of inner wall of submerged entry nozzle by buildup of non-metallic materials is called clogging which can result in complete blockage of the melt flow route. SEN clogging significantly lowers productivity, predictability, and energy efficiency of the casting process. It also decreases quality of the final product because parts of clogging materials may be fragmented and act as macro-inclusions entering the mold region. Clogging changes jet characteristics and flow pattern near the exit-ports of SEN leading to asymmetric flow and abnormal temperature distribution in the mold region. These phenomena cause entrapment of non-metallic inclusions or bubbles onto solidifying shell [61], entrapment of top liquid slag [28], and even breakouts [28]. Although many studies have been made to understand clogging, this phenomenon sometimes appears randomly. Therefore, clogging is a complex phenomenon which is not fully understood yet [63].

2.3.2 Mechanisms of clogging

Many researchers have investigated the clogging behavior; different mechanisms for SEN clogging were suggested, as illustrated in Figure 2.5 schematically:

(a) attachment of de-oxidation and re-oxidation products on the SEN wall [50,64,65];

(b) thermochemical reactions between the refractory and the melt at the SEN wall leading to in-situ formation of oxide products [66,67];

(c) negative pressure drawing oxygen through the SEN refractory pores into the inner SEN wall and reaction of oxygen with the steel melt to form oxides [68];

(d) temperature drop of the melt leading to lower solubility of oxygen in the steel melt and resulting in precipitation of alumina at SEN-steel interface [69,70]; and

(e) possible solidification of the steel melt on the SEN wall [1,71].

Although diverse opinions on the SEN clogging mechanisms exist, evidences show that the deposition of non-metallic inclusions (NMIs) of de-oxidation and re-oxidation products, e.g. Al_2O_3, on the SEN wall is still the primary cause of clogging [72]. For example, similar morphologies and chemical compositions of NMIs were observed in the melt, in the clog material, and in the as-cast product [73]. Moreover, results of investigation for nozzle materials did not find statistical difference in the mean rate of clogging for alumina, zirconia, magnesia, and zirconia-graphite nozzles [74].
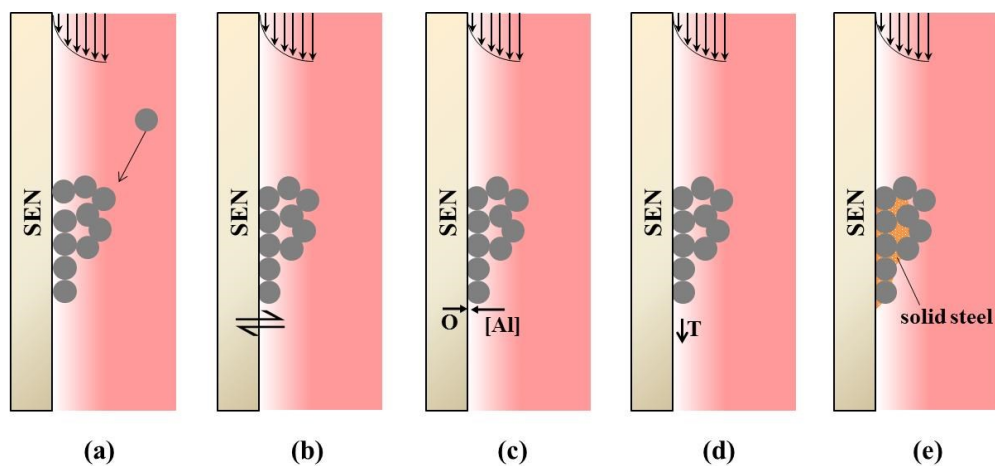
Figure 2.5 Illustration of different mechanisms suggested for the SEN clogging: (a) attachment of de-oxidation and re-oxidation products, (b) reaction in the melt at the SEN wall, (c) drawing oxygen through the SEN and reaction with the steel melt, (d) temperature drop leads to precipitation of alumina, (c) solidification of the steel melt on the SEN wall.

The main composition of clogging material is Al_2O_3 in aluminum killed steel. Depending on the steel grade, other NMIs such as TiN, TiO_2, ZrO_2, CaS, and rare earth oxides have

been observed [15,75]. They originate from the steel melt [65,76], and typical size of them is 2-10 μm [77,78]. The shapes of them are different: globular, cluster, dendrite, coral-shaped cluster, faceted particles, and even irregular plate [61,77–80]. However, major NMIs as found during the operation of steel plants are alumina and they are mostly in the shape of globular.

Owing to the fact that attachment of non-metallic inclusions on the wall is known as the common mechanism of clogging, a lot of researches have been conducted about adhering of a NMI to another one or to a wall in a steel melt [81–88]. It is believed that when a NMI approaches the SEN wall, it tends to adhere to the wall due to the interfacial contact force, called also capillary force or adhesion force, as shown in Figure 2.6. This kind of force is because of the low wettability of oxide, like Al_2O_3, by the steel melt. The bridge forms between NMI and SEN wall can be in the gas phase [82,87] or liquid phase [81]. The capillary force is much larger than other detaching forces, such as drag, buoyancy, or lift forces. To reduce the capillary force, an idea is changing the materials of the SEN wall. Change the refractory material of the wall from alumina-based to zirconia-based material is not enough to improve wettability characteristics and to permit detachment of NMI from the wall [89]. Using an MgO wall, the capillary force could be stronger than that when an alumina wall is used [90].

Sasai [83,84] measured the agglomeration force exerted between alumina particles in molten steel directly. Molten steel flow has no effect on the measurements. He found that the force between the alumina particles in aluminum-deoxidized steel melt derives not from the van der Waals force but from the cavity bridge force occurring due to the steel melt, which is unlikely to wet the alumina particles. When two alumina inclusions are approaching each other in molten steel, an agglomeration force is generated by the cavity bridge formation between two inclusions. The agglomeration force gradually increases to reach the maximum value in complete contact of two inclusions. However, the origination

mechanism of the cavity bridge between two inclusions is not explicitly clarified in these papers.
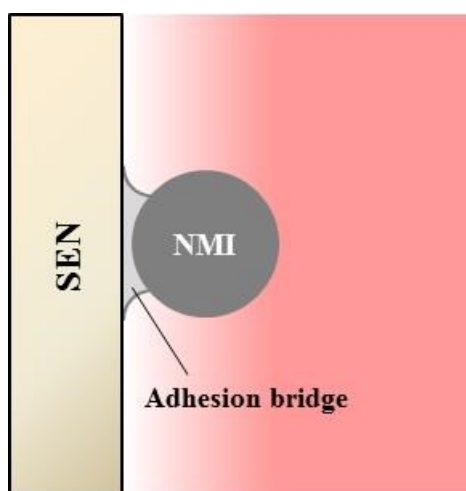
Figure 2.6 Adhesion bridge between an NMI and SEN wall.

2.3.3 Industry measures to prevent SEN clogging

The best way to avoid clogging is improving steel melt cleanness by reducing de-oxidation products like non-metallic inclusions before entering of the melt into the SEN. Despite of the various techniques employed to remove NMIs from the steel melt, such as optimization of the melt flow in tundish [91−96], a large number of microscopic NIMs remain in the melt and follow the melt through the SEN in the mold.

2.3.3.1 Argon injection

Argon injection into the SEN through SEN wall or stopper rod is extensively used to prevent or postpone clogging. By injection of argon through SEN, a film of argon may form on the SEN wall preventing SEN wall from contact and reaction with the melt. In addition, the pressure inside the SEN is increased by argon injection. This can compensate pressure drop in the SEN, reduces air aspiration, and consequently decreases oxidation on the SEN wall [71]. Argon injection also has some disadvantages like increased mold fluctuations,

bubble entrapment by solidifying shell, and nozzle cracking due to the high back pressure or decreased SEN thermal shock resistance [71].

2.3.3.2 Calcium treatment

Calcium treatment of aluminum-killed steels is a method that changes solid alumina inclusions to calcium-aluminates which has lower melting point and is in liquid state at the operating temperature [97–99]. Because liquid inclusions would not attach on the SEN wall, clogging is prevented. Nevertheless, sometimes clogging is observed after calcium treatment in industrial practices. When the refractory has big grain size and big cavities on the surface, liquid calcium aluminate inclusions can attach on the wall of SEN. If SEN has tiny grain size and smooth surface, no attachment of the liquid inclusions happens. Non-suitable calcium treatment causes solid calcium aluminates. Solid calcium aluminate phases tend to be agglomeratied and sintered like solid alumina particles. Hence, nozzle clogging can occur [98]. Excessive usage of Ca can cause operational issues (e.g. slide gate plate erosion) [99].

2.3.3.3 Improvement of SEN material

Using alternative refractory material for SEN has been subject of various researches to prevent clogging [74,100–103]. The rate of clogging was studied for zirconia, alumina, magnesia, alumina-graphite, and zirconia-graphite as nozzle refractory material. No statistical differences in the mean rate of clogging were observed between all of the pure oxide nozzles and zirconia-graphite nozzles. However, the alumina-graphite nozzles were clogged at a much higher rate than the other nozzles [74]. SEN materials containing calcium, like calcium titanate and calcium zirconate, showed better clogging resistance than typical industrial alumina graphite SEN due to formation of liquid calcium aluminates [101,102]. However, the effectiveness of calcium containing materials is limited by diffusion of calcium through the refractory to reach inner surface of the refractory.

Svensson et al. [103] used yttria-stabilised zirconia (YSZ) PVD-plasma-coated to prevent clogging in pilot and industry scales. Overall, clogging of the nozzles was not eliminated but the clogging tendency was reduced to some extent for the YSZ plasma-coated nozzles.

2.3.3.4 Modification of SEN design

Since the design of the SEN plays a very important role in the melt flow pattern and clogging, several designs have been proposed to reduce clogging. One idea is to modify melt flow entering SEN by changing stopper shape [17]. An oversized nozzle also was proposed as a possible solution for clogging [69]. A parabolic curve shaped bottom (instead of flat bottom) was designed for SEN to guide the liquid steel flow with reduced turbulence through exit-ports [15]. A swirl blade was inserted in the SEN to form swirling flow of the melt which may help productivity of process and quality of products [44,45]. The swirling flow prevents vortex formation and flow stagnation near the exit-ports that are responsible for the adhesion of non-metallic inclusions. Prevention of exit-port clogging makes the outlet flow stable during the entire casting period, which is effective in stabilizing the surface quality of final products [45].

2.3.3.5 Use of electric current

A recent remedy for preventing SEN clogging is considering electrically charging of SEN and NMIs. Due to the friction between SEN and flowing molten steel, an electric double layer may form on the interface of SEN. Similarly, an electric double layer can exist on the surface of NMIs. The interaction between electrostatic forces might affect SEN clogging [104–106]. However, this idea is still very rough and more deep investigations are required. Another related remedy is applying low-density electric current pulse to SEN which results in formation of dense inclusion buildup. Therefore, prolonged service life of SEN is expected. Based on this idea, SEN and stopper are connected to an electric current pulse power. Because of high content of graphite, the bodies of SEN and stopper have excellent

conductivity even at high temperature. So, the electric potential difference is mainly exerted on the inclusion buildup in the inner wall of SEN [107].

2.3.4 **Modeling of SEN clogging**

Occurrence of the clogging is a complex process. Assuming deposition of solid NMIs on the SEN wall is the dominant mechanism, clogging mainly concerns four steps, as depicted in Figure 2.7:

(a) the turbulent fluid flow and the transport of the suspension particles towards the wall;

(b) the interaction of the fluid with the wall and adhesion mechanism of the particles on the wall;

(c) formation and growth of the clog; and

(d) detachment of the clog material by the fluid flow to form fragments.

In some other cases, chemical reactions, electrostatic interactions at the fluid-wall interface, or even freezing (solidification) of the fluid on the wall might occur. Enormous efforts were made to understand the clogging mechanisms in different fields reviewed by [108]. High temperature of process, possible chemical reactions, possible phase change of the melt (solidification), and electrical conducting nature of molten steel might exhibit different clogging mechanisms in comparison with those as studied in other fields.
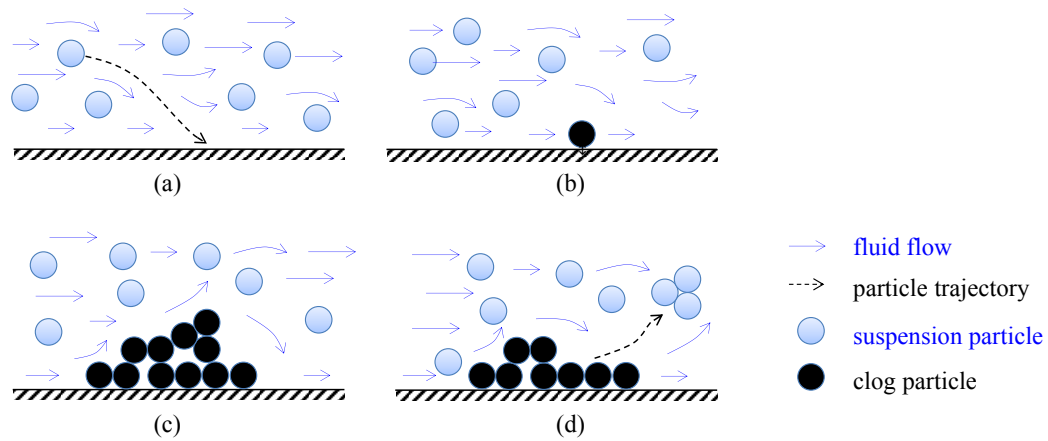
Figure 2.7 Schematic of clogging phenomenon (four steps).

Different numerical models were developed to simulate the clogging during steel continuous casting by emphasizing one or more critical steps of Figure 2.7. The simplest method is single-phase based Eulerian approach. The flow is solved, while the motion of the particles is not tracked explicitly. For example, by changing the geometry manually to mimic the build-up of the alumina clog on the inner wall of the nozzle, Bai and Thomas [26] studied the effect of the clog on the flow through a slide-gate nozzle. Because recirculation zones form in the vicinity of the slide-gate, clogging tends to build up, initially, in these recirculation zones. Four cases with different shapes of slide-gate and initial clogging, as shown in Figure 2.8(a), were simulated. In these cases, the clog material is assumed as a solid material with smooth interface with melt flow. Figure 2.8(b) shows the simulated flow pattern at the center plane. The clogging condition and edge roundness affect not only the flow pattern but also the pressure drop across the nozzle. The pressure drop across the gate plates decrease from case (i) to (iv). The simulation results also showed that the initial clogging around the slide gate enhances the melt flow rate at first due to a streamlining effect and after severe clogging the flow is eventually restricted, so the gate opening has to be increased to provide constant casting speed.
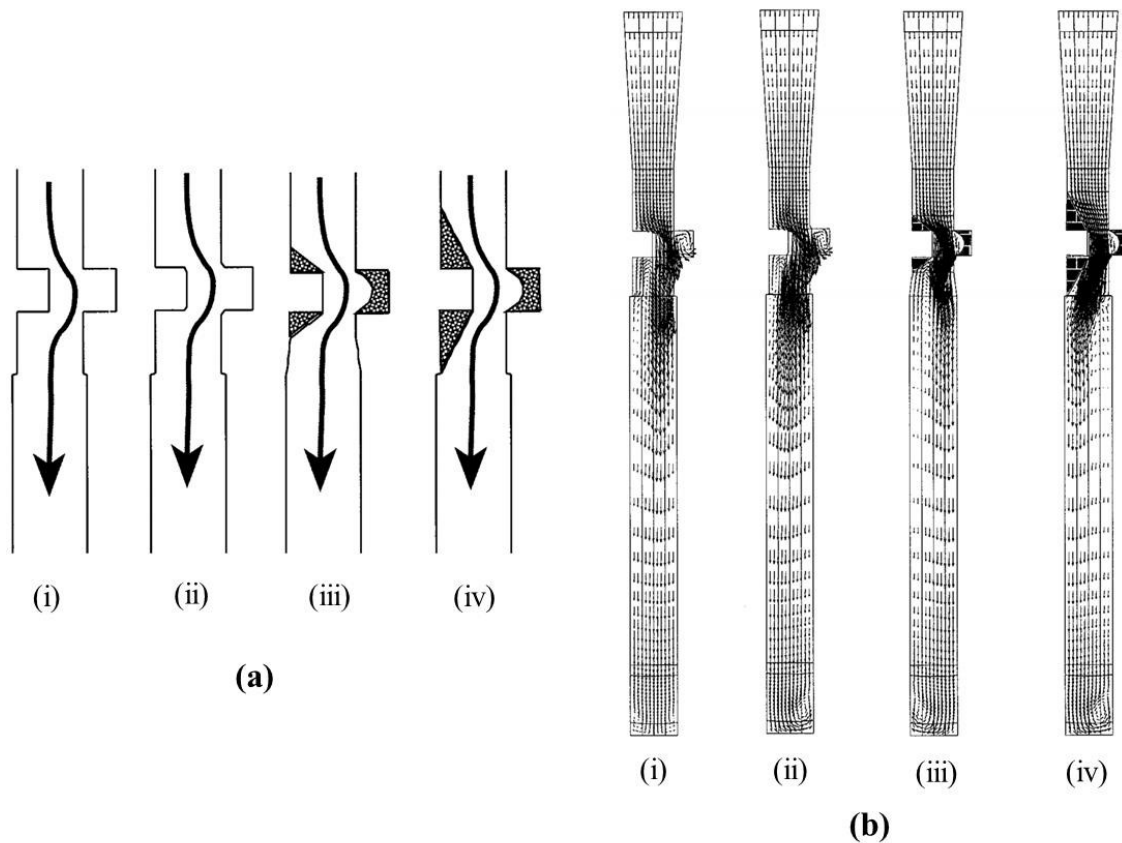
Figure 2.8 (a) Assumed shapes of slide-gate and initial clog: (i) sharp edges, (ii) rounded edge, (iii) sharp edges smoothed with initial clogging, and (iv) more initial clogging; (b) simulated flow pattern of case (i)-(iv) [26].

In such kind of simulations, only the flow pattern for a certain shape of the clog and at a certain time can be realized. Information about next time is missing.

Zhang and co-workers [28] used the similar method, e.g. by blocking half of one exit-port of the SEN manually, as shown in Figure 2.9(a), to study the clog-induced asymmetrical flow in the mold, the locally-superheated region and the increased risk of breakouts. They found that with SEN one-sided clogging, inclusions travel a much larger distance, on average, before they escape from the top or move to the bottom. Under these circumstances, more inclusions are carried by the flow to the top surface of the nonclogged side. The SEN one-sided clogging also generates an asymmetrical temperature distribution in the mold; it generates temperatures higher than the liquidus temperature at some locations of the solidified shell, which increases the risk of breakouts.
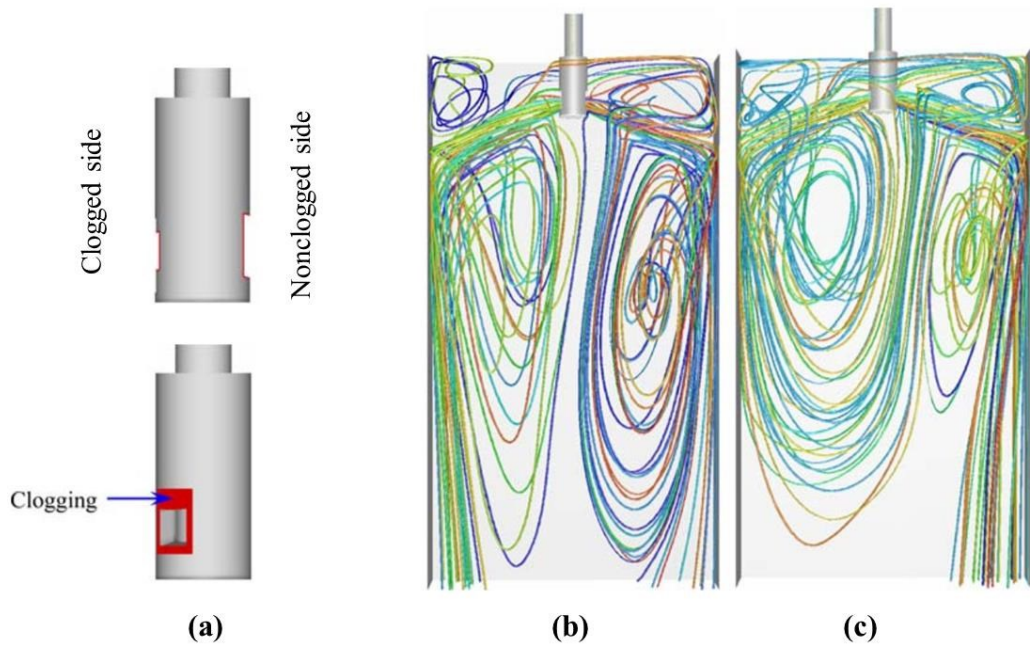
Figure 2.9 Assumed clogging condition at SEN exit-ports (a) and 3-D streamlines for clean (b) and one-side clogged (c) SEN [28].

Rackers and Thomas [71] assumed that clog on the SEN wall is in a rod shape attached perpendicularly to the wall. Then the minimum diameter and length of a rod made of alumina needs to withstand against the melt flow was estimated. They concluded that during clogging a fraction of rods has sufficient cross-sectional area to continue growing and the other rods fails by the drag force of the melt flow, i.e. fragmentation of the clog (Figure 2.7(d)). Similarly, Sambasivam [15] investigated a new SEN with curved bottom configuration and found that the power of the shear stress at the SEN bottom wall to wash away the inclusions is improved. Therefore, the curve bottom shows better anti-clogging characteristics. When the inclusion particle attaches to the SEN wall, it sinters quickly and forms a neck [87], as shown in Figure 2.10(a). If the shear stress at the neck is higher than the alumina sinter bond strength, the neck will be broken and the particle will be washed away. The shear stress at the neck of the sinters of the three bottom designs for various neck radii is plotted in Figure 2.10(b). The results show that the curved bottom SEN leads to break larger neck size; thus, removal of the attached alumina inclusions is easier [15].
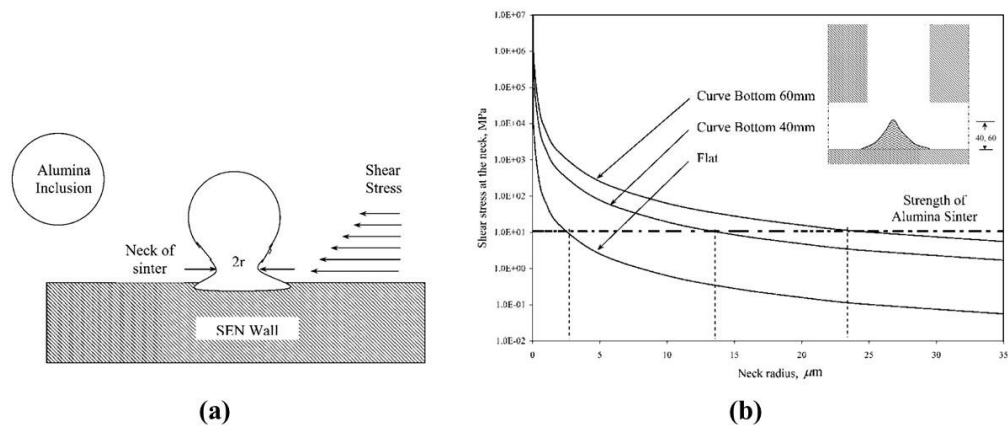
Figure 2.10 (a) Schematic representation of adhesion of inclusions onto wall; (b) comparison of shear stress on the neck of sinter for different SEN bottom profiles showing anti-clogging effectiveness [15].

Most frequently-used numerical method is the Eulerian-Lagrangian approach, with which both fluid flow and particle motion are calculated. The particles are treated as a discrete phase, for which the motion trajectories are calculated in a Lagrangian frame of reference, while the fluid flow is calculated with Eulerian approach [3,7,23,61].

Mohammadi-Ghaleni et al. [7] compared clog deposit thickness on the interior surface of a commercial clogged SEN with CFD predictions of melt flow in the SEN. They correlated melt flow pattern and particle-wall interaction to the deposit thickness on different cross sections of the SEN. Figure 2.11 indicates experimental results and CFD prediction of particle deposition. In Figure 2.11(a), particles inside the lower part of the nozzle (below the slide-gate) after 2 seconds of simulation are shown; the blue particles are attached to the nozzle wall; the red particles are moving in the steel melt. In Figure 2.11(b), an assembly of cut sections of the nozzle is shown. There are two convergence areas in this design of SEN. The experimental results show that the thickest deposit is between two convergence areas. Similarly, in the simulation results, highest particle attachment occurs between two convergence areas. However, this simulation presents a rough estimation of clogging area. The interactions between the melt flow and the growing clog, which is highly effective on the melt flow, is ignored.
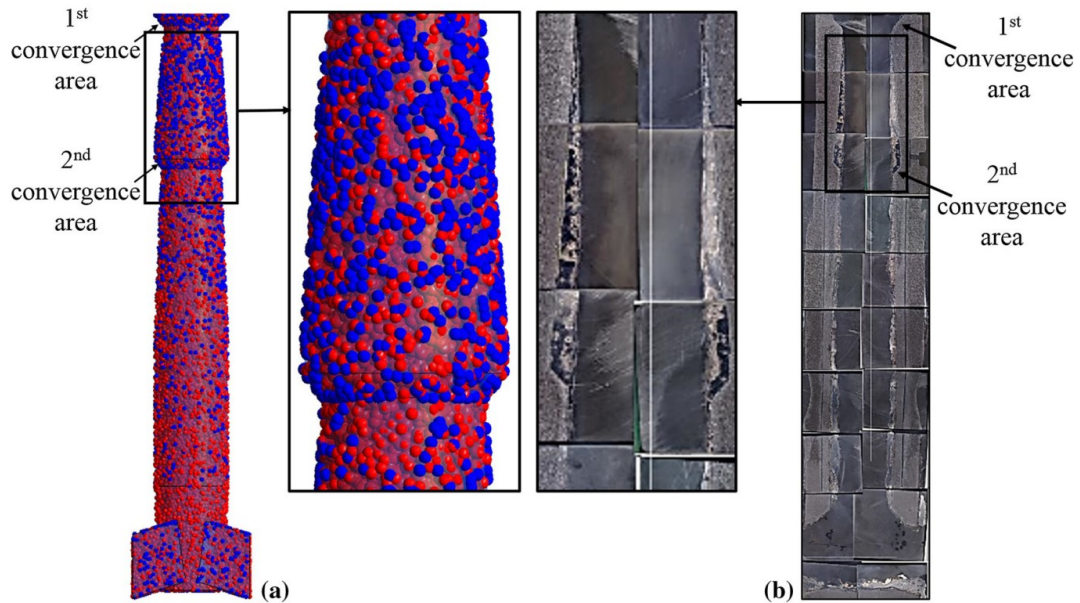
Figure 2.11 Particle deposition on the SEN walls: (a) simulations results and (b) experimental results. Only 20% of particles are shown in (a) with a particle size 110 times more than their actual size for better visualization of the results. Blue and red colors denote attached and moving particles, respectively [7].

Most studies based on Eulerian-Lagrangian approach focused only on the fluid flow and particle transport, i.e. step (a) of Figure 2.7.

Long et al. [75] developed a model in which the fluid region is divided to three zones: turbulent bulk zone, transition layer, and laminar sub-layer (Figure 2.12). A particle is supposed to be captured by the wall if it enters the laminar sub-layer. The thickness of the laminar sub-layer is defined based on classical empirical fluid flow velocity distribution in a pipe. Although some fluid-wall interactions were taken into account by wall roughness of the SEN and its influence on the flow, it is a fixed value and does not change during the process. Hence, here, the adhesion mechanism (step (b)) was neglected partly and the growth of the clog (step (c)) was ignored totally. Using this model, the effects of inclusion diameter on SEN clogging were quantitatively investigated. The results indicated that the inclusions with diameter larger than 100 μm are not able to be entrapped by the nozzle wall, and the entrapment probability will increase quickly with decreasing size of inclusions.
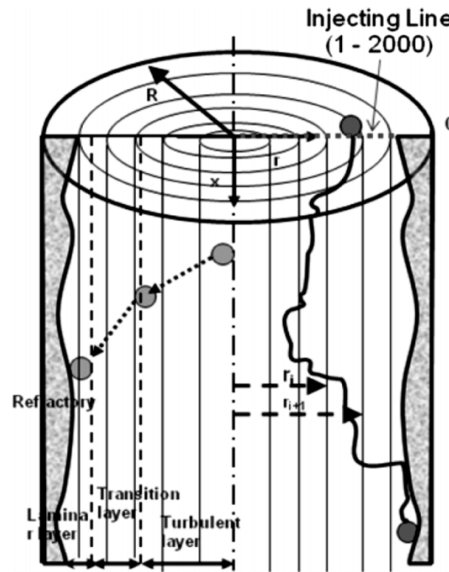
Figure 2.12 Schematic of the fluid flow and motion of inclusions in a pipe nozzle [75].

Gutierrez et al. [109,110] studied hydrodynamic factors involved in the inclusion deposition at the nozzle wall, such as different forces acting on the inclusions, in a coupled tundish–mold system domain. In this simulation, around 30% of the inclusions feed at the ladle shroud deposited along the upper tundish nozzle and the SEN exit-ports. These adhesion zones were related to low static pressure and high turbulence zones.

Eulerian-Eulerian two-phase approach was also used to study the clogging phenomenon. Here the particles are treated as a secondary Eulerian phase. Therefore, a great number of NMIs in the steel melt can be simulated. From this point of view, Eulerian-Eulerian approach is more time-saving than Eulerian-Lagrangian approach for NMI motion in complex steel flows. However, detailed information about particle tracking is lost.

Ni et al. [111,112] used Eulerian-Eulerian approach to predict the inclusion deposition rate in a SEN where Brownian and turbulent diffusion, turbophoresis, and thermophoresis as transport mechanisms were considered. Effects of different process parameters and materials properties, such as steel flow rate, particle diameter, particle density, wall roughness and temperature gradient near the wall, on deposition rate were also studied. It

was shown that the steel flow rate has a very important influence on the rate of deposition of large particles, for which turbophoresis is the main deposition mechanism. In turbophoresis mechanism, particle transport is caused by gradients in fluctuating velocities (i.e. turbulence). For small particles, both wall roughness and thermophoresis have a significant influence on the particle deposition rate [111]. A similar Eulerian-Eulerian model was developed by Eskin et al. [113] for the particle deposition in a vertical turbulent pipe flow. Again, the detailed adhesion mechanism of the particles on the nozzle wall (step (b)) cannot be considered and the growth of the clog (step (c)) has to be ignored.

The most promising model which can really cover clogging steps (a)-(c) in Figure 2.7 was proposed by Caruyer et al. [114]. They simulated multilayer deposition of particles with diameter of 80 μm on bore surface of a pipe using an Eulerian-Lagrangian method and studied fluid velocity modification by deposition over time. In their simulation, the deposited material is supposed to be a closely packed porous medium formed by same size spherical particles and incoming particles are always considered to deposit on wall or adhering particles.

A summary of the researches done about modeling of clogging in steel continuous casting is listed in Table 2.1. In this table, the numerical works related to clogging in SEN are considered.

Table 2.1 A summary of researches about numerical modeling of SEN clogging

Reference	Clogging steps					Key feature(s)
	(0)	(1)	(2)	(3)	(4)	
Bai and Thomas [26]	X					Flow pattern after clogging
Zhang et al. [28]	X	X				Flow pattern and inclusions trajectory after clogging
Rackers and Thomas [71]	X				X	Shear stress on the clog
Smbasivam [15]	X				X	Shear stress on the clog
Yuan et al. [3] and Pfeiler et al. [23]		X				Eulerial-Lagrangian approach and inclusion trajectory
Mohammadi et al. [7]		X				Detached–Eddy Simulation (DES) model for turbulent flow in the SEN
Long at al. [75]		X	X			Effects of wall roughness and prediction of service life of the SEN before clogging
Ni et al. [111,112]		X	X			Eulerial-Lagrangian approach and effects wall roughness
Ni et al. [115,116]		X				Eulerial-Lagrangian approach and effects of wall function in turbulence model
Gutierrez et al. [109,110]		X				Effects of different forces acting on an inclusion before attaching
(0) Manually change in the computational domain representing clogging (1) Transport of the inclusion towards the wall (2) Interaction of the fluid with the wall (3) Growth of the clog (4) Fragmentation of the clog						

2.4 Numerical modeling of clogging of other industry processes

In addition to steel continuous casting, clogging is a common problem in vast area of scientific fields and engineering applications [108] such as heat exchangers [117], petrochemical industry, automotive industry [118], food productions [119], and pharmaceutical industries [120]. This phenomenon is also termed as fouling. Here, a short

review of the numerical modeling efforts in various fields of research is presented. The chemical/physical mechanisms behind other processes may be different. However, the theoretical backgrounds would be helpful for understanding SEN clogging.

The models of fouling can be divided into two groups: single-layer deposition and multi-layer deposition. In single-layer deposition the interaction between particle and wall is considered, while in multi-layer deposition, both particle-wall and particle-particle interactions are taken into account. DLVO theory, which is based on the works of Deraguin-Landau [121] and Verwey-Overbeek [122], describes particle wall interactions considering van der Waals (VDW) and Electrostatic Double-Layer (EDL) forces. VDW forces are forces which occur between atoms or molecules of particle and wall. When a charged surface is in an electrolyte, one layer of charges forms on the particle surface and another layer is made of opposite ions in the solution, as shown in Figure 2.13(a). Depending on material properties, EDL forces can either be attractive or repulsive. Figure 2.13(b) indicates a typical DLVO interaction energy for a particle (1μm diameter) interacting with a plate in repulsive electrostatic conditions. DLVO interaction energy is sum of VDW interaction energy and EDL interaction energy. It can be seen that the VDW attraction is predominant at small separation distances and large separation distances, while the EDL repulsion dominates the interaction energy at intermediate separations. This peak in the DLVO curve corresponds to the so-called energy barrier, E_{barr}, which can prevent incoming particles from reaching the surface [108].

Using DLVO, particle-wall interactions can be treated with an energy-balance method: if wall-normal kinetic energy of the particle is high enough to overcome the energy barrier, the particle hits the wall; otherwise it rebounds.
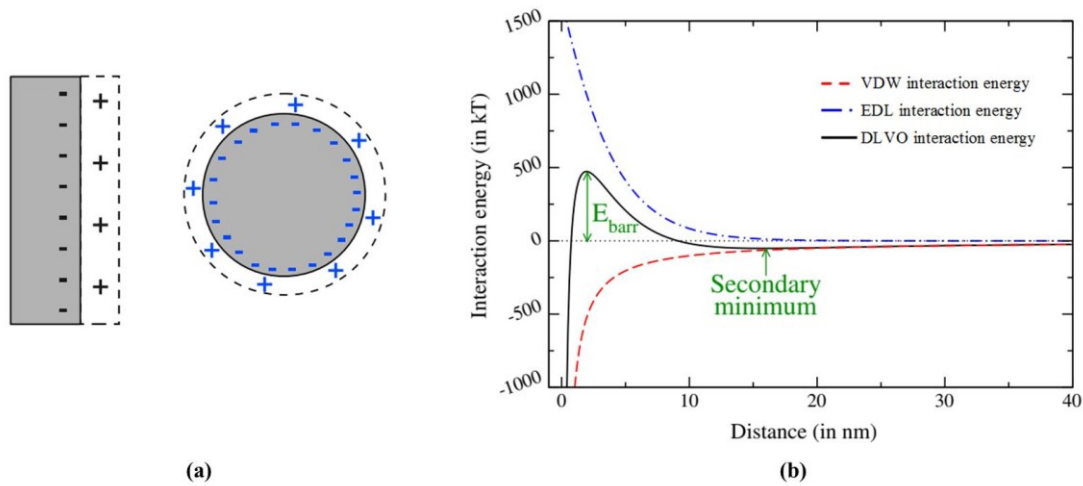
Figure 2.13 Representations of electrostatic double-layer forces (a) and DLVO interaction energy between a sphere and a plate (b) [108].

According to this theory, electrostatic properties of liquid plays important role in particle deposition on wall. A study on the transport and deposition of hematite particles on glass has shown the importance of ionic charge strength [123]: at very low ionic strength only monolayer deposition was observed, while at high ionic strength multilayer deposition became significant. This mechanism was further verified by another investigation on a microfluidic filtration device where fouling of the polymeric micro-channels by micron-sized (4.9 μm) latex particles occurred [124]: particles at low ionic strength (more hydrophilic conditions) did not lead to the blockage of the micro-channels by fouling, while particles at high ionic strength (more hydrophobic conditions) leaded to a fast fouling of the micro-channels.

The energy-balance method can be used for NMI particle and refractory wall. This method converts all effective parameters to energy. Therefore, it is easy to find an energy criterion for total attractive or repulsive interaction between wall and particle. A primary and simple energy-balance has been used by Heuzeroth et al. [86] for simulation of NMI filtration in liquid metal.

Surface roughness is of concern to particle-wall interactions. In some models, surface roughness is assumed as a collection of hemispherical asperities on a smooth surface, shown schematically in Figure 2.14. Surface roughness is identified by two parameters: the asperity radius and the number of asperities per unit area [125–127]. This idea gives more detailed information about interaction between the particle and the wall asperities. In models for Lagrangian NMI tracking and deposition on refractory wall, the wall roughness have been taken inti account by a constant roughness height, like [75].
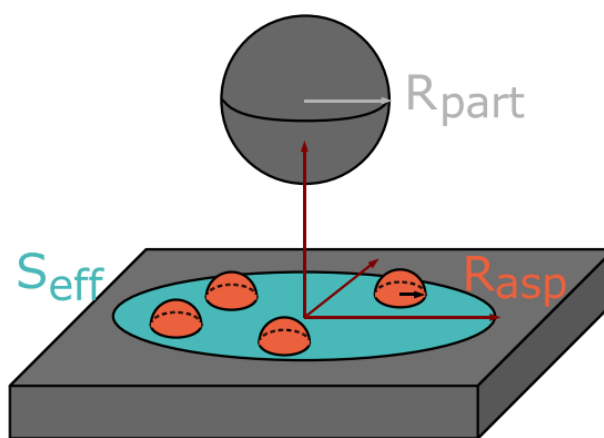
Figure 2.14 Description of surface roughness using hemispherical asperities placed randomly underneath each incoming particle [127].

Various Lagrangian models have been presented for multi-layer deposition of particles, like Langevin Dynamics [128], Brownian Dynamics [129], or Dissipative Particle Dynamics [130], which are interesting due to the detailed treatment of particle-wall and particle-particle interactions. To use such kinds of models for particle motion and deposition, fluid phase must be completely known, i.e. instantaneous quantities must be available at every location and time. To have such detailed information about fluid flow, fine scale CFD like Direct Numerical Simulation (DNS) is required. Therefore, the models are limited to very small region of the flow or simple situations. Henry et al. [108] suggested one-particle PDF (Probability Density Function) methods which are attractive candidates. These methods compromise between a fine enough level of description for both the fluid and the particles;

they have the ability to be applied to general inhomogeneous 3D turbulent flows (industrial situations). In one-particle PDF, all the interactions have to be expressed in terms of the properties attached to each particle (which defines the particle state vector). In such an approach, the particle equations of motion are generally described by using effective or modeled forces, which can rely on mean-fields like fluid pressure and velocity. A qualitative comparison has been carried out between modeling results and experiment of Bacchin et al. [124] for latex particles on polymer surfaces in a microfluidic device. In this experiment, surface properties of the micro-fluid channel were changed by rinsing with potassium chloride solution (KCl conditioning) and ultrapure water (water conditioning) before the filtration process. KCl conditioning resulted in less hydrophobic surface. Figure 2.15 shows the fouling results for two surface conditionings. Clogging of the micro-channels was induced by arches formed at the micro-channels entrance (Figure 2.15(c)) when water conditioning is performed. On the contrary, by KCl conditioning dendrites/columns were formed (Figure 2.15(b)) and there is no arc at the microchannel entrance.

(a) (b) (c)
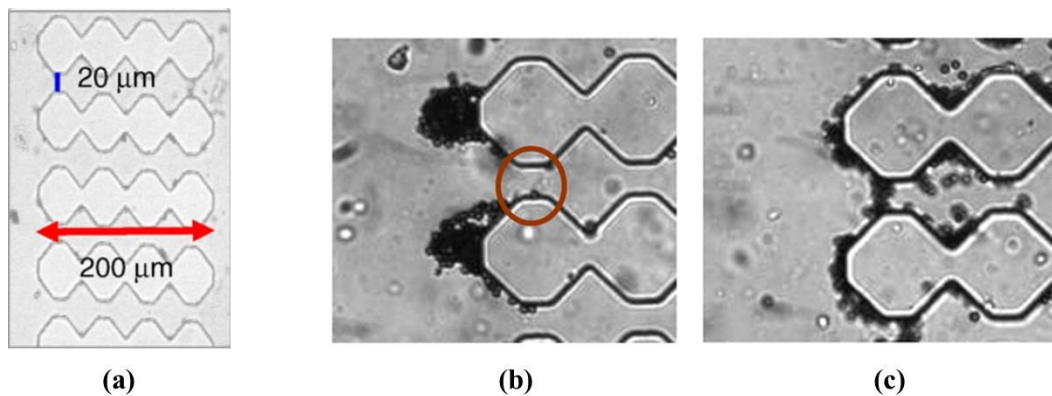
Figure 2.15 Dimensions of micro-channels (a); observation of particle capture after a conditioning of the micro-channels with KCl solution (b) and ultrapure water (c) [124].

Figure 2.16 indicates a typical simulation result of the model, representing fouling pattern corresponding to the induction effect. The induction effects appear when particle-surface

interactions prevent deposition except in some local areas while particle-particle interactions are weakly repulsive. These effects lead to the formation of surface clusters (like trees) that eventually merge to form arches [108]. In SEN clogging, this kind of model can be used to find clog structure for different NMI-melt systems. Currently, the knowledge about formation of clog structure is very limited. All information has been extracted from post mortem analysis of the clog material, like [78].
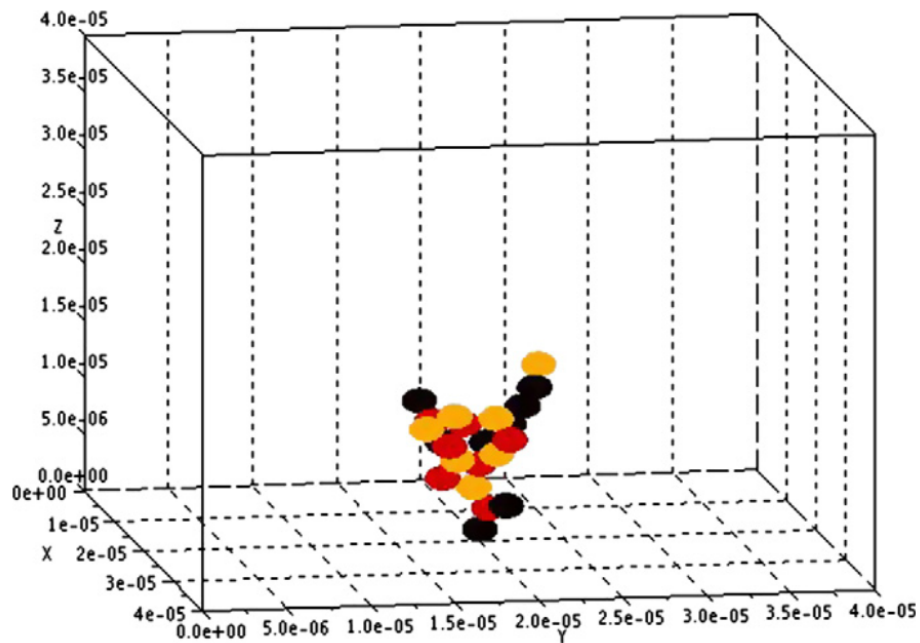
Figure 2.16 Predicted fouling patterns for the induction effect [108].

After multi-layer deposition, multi-layer resuspension (fragmentation) also may occur. A common reason of particle resuspension is hydrodynamic forces on the deposit, leading to a break-up of clusters where the cohesion forces that maintain particle-particle contact are small enough, as shown in Figure 2.17 schematically.
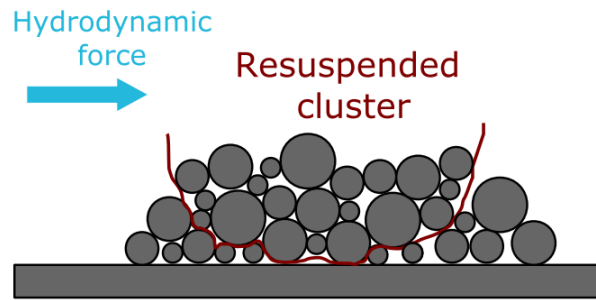
Figure 2.17 Drawing showing the weak cohesion forces inside a surface cluster, which can lead to the fragmentation of the cluster [108].

To model multi-layer resuspension, there are two main difficulties: the deposit morphology and the rupture mechanisms associated with the resuspension of large aggregates [131]. Friess and Yadigaroglu [132] proposed a force force-balance model for the resuspension of multilayer aerosol deposits considering the dependence of resuspension rates on the deposit structure, as well as the fact that particles are typically resuspended in clusters. They found that the resuspension rate depends on the porosity of the deposit. Resuspension in high porosity deposit is easier than that in less porous one where particle are compactly deposited. Figure 2.18 indicates time evolution of a deposit under resuspension. Stochastic models [133–135] and Discrete Element Models (DEM) [136] have been also developed for multilayer resuspension.

It is known that fragmentation of clog is a source of new macro-inclusions entering mold region [63]. Developing an accurate model, which estimates the fragmentation rate and the size of fragments, helps us to have most robust information about steel cleanness in the mold.
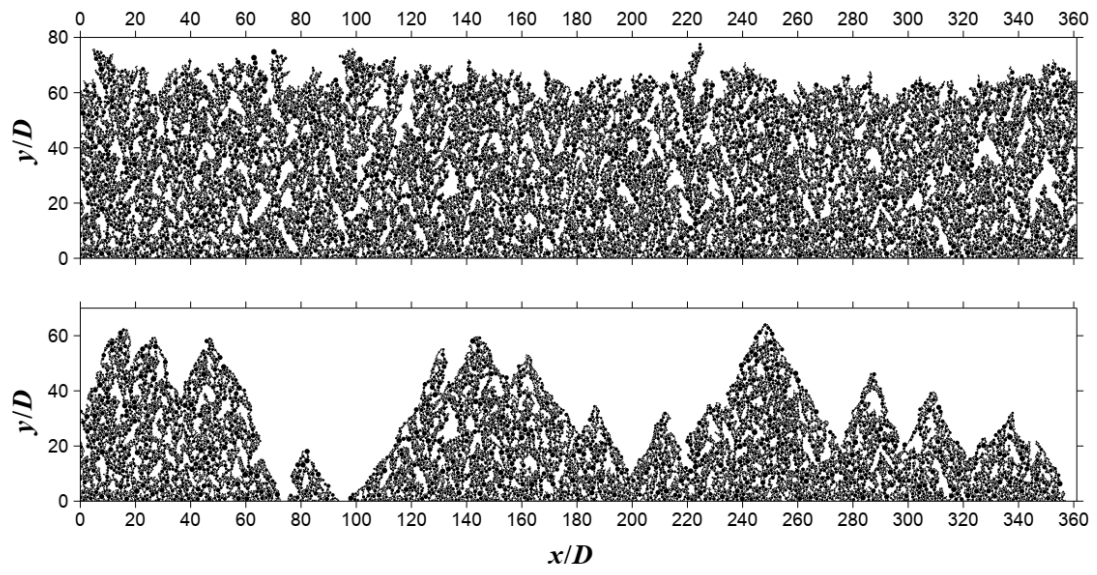
Figure 2.18 Time evolution of a deposit under resuspension; Top: initial state, Bottom: after simulated resuspension of 50% of the initial mass [132].

3. Numerical Model

3.1 General model description and assumptions

As shown in Figure 2.7, the clogging process is considered in four steps: (a) the turbulent fluid flow and the transport of the suspension particles towards the wall; (b) the interaction of the fluid with the wall and adhesion mechanism of the particles on the wall; (c) formation and growth of the clog; (d) detachment of the clog material by the fluid flow to form fragments. Correspondingly, the model should consider four parts. In the current version of the model, however, step (d) is neglected. General model assumptions for each step are listed below.

(a) Transport of the suspension particles by turbulent flow

- An Eulerian model is employed to calculate the turbulent flow.

- Steel melt behaves as an incompressible Newtonian fluid.

- To model turbulent flow, the shear-stress transport (SST) k-ω model is applied.

- Steel melt is isothermal; therefore, heat transfer and solidification do not occur (This assumption is removed in the updated version of the model).

- A Lagrangian model tracks the motion of the particles since the volume fraction of moving particles in the melt is much smaller than 0.1.

- Non-metallic inclusions are rendered as spherical particles which are chemically inert.

- Interactions between particles are neglected because of low concentrations of inclusions in the steel melt. Hence, there is no coagulation.

- Constant material properties of the steel melt and particles are applied.

- In the melt, the one-way coupling between particle motion and fluid flow is applied: flow influences particle motion, but particle motion does not influence the flow.

(b) Interaction of the fluid with the wall and adhesion mechanism of the particles

- The laminar sub-layer adjacent to the wall is neglected due to the wall's roughness.

- Particles mechanically stick when they reach the wall.

- No chemical reaction occurs on the wall.

- Van der Waals force between the wall and the particle is not taken into account; the explanation to this assumption is made in §3.3 .

- Particles carry no electrostatic charge because molten steel is electrically conductive.

- Equivalent sand-grain roughness is used to treat the initial stage of clogging, i.e. the deposition of particles in the SEN wall causes the change in the SEM wall roughness.

(c) Formation and growth of the clog

- The mechanism of deposition of particles on the clog front is the same as that of particle deposition on the SEN wall.

- The clog is a porous medium with open pores, which interacts with the melt flow.

- Clog porosity information is extracted from a post-mortem analysis of experimental clog samples.

- A volume-average scheme is used to define clog properties, e.g. porosity and permeability.

3.2 Flow and particle transport

3.2.1 Fluid flow

The melt flow as the primary continuous medium is described by the conservation equations of mass and momentum:

$$\nabla \cdot (\rho \vec{u}) = 0, \tag{3.1}$$

$$\rho \frac{\partial \vec{u}}{\partial t} + \nabla \cdot (\rho \vec{u} \vec{u}) = -\nabla p + \nabla \cdot (\mu \nabla \vec{u}) + \rho \vec{g} + \vec{S}_u, \tag{3.2}$$

where ρ is the density of fluid; $\vec{u}$ is the fluid velocity; t is the time; p is the static pressure; μ is viscosity; and $\vec{g}$ stands for gravity vector. $\vec{S}_u$ represents drag source terms due to the porous clog material and/or as-solidified steel.

To model the turbulent flow, shear-stress transport (SST) k-ω model is adopted. It effectively blends the robust and accurate formulation of the k-ω model in the near-wall region with the free-stream independence of the k-ε model in the far field [137]. In this turbulence model, equations for the transport of turbulent kinetic energy, k, and its specific dissipation rate, ω, are

$$\rho \frac{\partial k}{\partial t} + \nabla \cdot (\rho k \vec{u}) = \nabla \cdot (\Gamma_k \nabla k) + \tilde{G}_k - Y_k + S_k, \tag{3.3}$$

$$\rho \frac{\partial \omega}{\partial t} + \nabla \cdot (\rho \omega \vec{u}) = \nabla \cdot (\Gamma_\omega \nabla k) + G_\omega - Y_\omega + D_\omega + S_\omega. \tag{3.4}$$

$\tilde{G}_k$ is the generation of turbulence kinetic energy due to mean velocity gradients; and G_ω is the generation of ω. Γ, Y, and D represent diffusivity, dissipation, and cross-diffusion term for k or ω, respectively. S_k and S_ω are source term due to the presence of the clog material

and/or as-solidified steel . These source terms are expressed by equations (3.24) - (3.26), (3.32), and (3.33).

3.2.2 Particle transport in bulk fluid

Two different particle tracking models have been adopted in the present model: one for the particle transport in the bulk fluid and one for the particle transport near the wall.

The motion of particles in the bulk melt is calculated by solving the transport equations in a Lagrangian frame of reference. The solid non-metallic inclusions as particles of spherical shape are assumed as a discrete secondary phase. It is, in fact, a force balance of the buoyancy ($\vec{F}_{\text{B}}$), drag ($\vec{F}_{\text{D}}$), lift ($\vec{F}_{\text{L}}$), virtual mass ($\vec{F}_{\text{VM}}$), and pressure gradient ($\vec{F}_{\text{press}}$), respectively.

$$m_{\text{p}}\frac{d\vec{u}_{\text{p}}}{dt} = \vec{F}_{\text{B}} + \vec{F}_{\text{D}} + \vec{F}_{\text{L}} + \vec{F}_{\text{VM}} + \vec{F}_{\text{press}}. \qquad (3.5)$$

The buoyancy force is due to the gravity and the difference between fluid density (ρ) and particle density (ρ_{p}). This force on a particle with diameter of d_{p} is formulated as

$$\vec{F}_{\text{B}} = \frac{(\rho_{\text{p}}-\rho)\pi d_{\text{p}}^3}{6}\vec{g}. \qquad (3.6)$$

Drag force is applied on a particle due to the friction of fluid on the particle surface. This force is calculated as

$$\vec{F}_{\text{D}} = \frac{1}{8}\pi d_{\text{p}}^2 \rho C_{\text{D}}|\vec{u'} - \vec{u}_{\text{p}}|(\vec{u'} - \vec{u}_{\text{p}}). \qquad (3.7)$$

The drag coefficient (C_{D}) is expressed by

$$C_{D} = \begin{cases} \dfrac{24}{Re_{p}} & , \ Re_{p} < 0.1 \\[2mm] \dfrac{24}{Re_{p}}\left(1 + 0.15Re_{p}^{0.687}\right), & 0.1 \leq Re_{p} \leq 10^{3}, \\[2mm] 0.44 & , \ Re_{p} > 10^{3} \end{cases} \tag{3.8}$$

where the particle Reynolds number (Re_{p}) is defined by

$$Re_{p} = \frac{|\vec{u} - \vec{u}_{p}| d_{p}\rho}{\mu}. \tag{3.9}$$

The lift force appears when a local velocity gradient (G) exists across the particle. This force is calculated via the following equations.

$$\vec{F}_{L} = -\frac{9}{4\pi}\mu d_{p}^{2} U_{s} \operatorname{sgn}(G)\left(\frac{\rho}{\mu}|G|\right)^{\frac{1}{2}} J, \tag{3.10}$$

$$G = \frac{du_{x}}{dy}, \tag{3.11}$$

$$J = 0.6765(1 + \tanh[2.5\log(\varepsilon) + 0.191])(0.667 + \tanh[6(\varepsilon - 0.32)]), \tag{3.12}$$

$$\varepsilon = \operatorname{sgn}(G)\frac{\left(\frac{\rho}{\mu}|G|\right)^{\frac{1}{2}}}{U_{s}}. \tag{3.13}$$

G expresses the normal gradient of the streamwise fluid velocity; U_{s} is the difference between streamwise velocities for the fluid and the particle; J is a correction factor.

The virtual mass force, as also called added mass force, is consequence of acceleration of the fluid adjacent to the particle with respect to the surrounding fluid. This force actually is an additional drag force and is calculated as

$$\vec{F}_{VM} = \frac{\rho \pi d_{p}^{3}}{12}\frac{d}{dt}\left(\vec{u} - \vec{u}_{p}\right). \tag{3.14}$$

Since there is pressure and stress gradient in the fluid, another force should be considered. The hydrostatic component of this force is implemented in the buoyancy force, equation

(3.6), and the non-hydrostatic component is known as pressure and stress gradient force and calculated by

$$\vec{F}_{\text{press}} = \frac{\rho \pi d_{\text{p}}^3}{6} \frac{D\vec{u}}{Dt}.$$

(3.15)

Additionally, a random walk model is an auxiliary for treating the chaotic motion of particles due to the turbulence. Thus, the instantaneous fluid velocity, $\vec{u'}$, as calculated by the following equation, is implemented in drag force term as the fluid velocity:

$$\vec{u'} = \vec{u} + \xi \sqrt{\frac{2k}{3}}.$$

(3.16)

$\vec{u}$ is the time averaged velocity as calculated by the momentum equation, equation (3.2), and ξ is a Gaussian distributed random number. The second term on the right hand side denotes turbulent fluctuation.

The relative importance of these forces for particle inclusions in the bulk of the steel melt is reviewed in [61].

3.2.3 Particle transport in near-wall region

Direct Numerical Simulation (DNS) has shown that the flow in the turbulent boundary layer consists of quasi-stream-wise coherent vortices, called "coherent structure". Transport of particles towards or from the wall is controlled by these structures, and there is a strong correlation between the coherent structures near the wall and the particle deposition on the wall [138].

In turbulent boundary layers, particles moving towards and from the wall are mainly governed by interactions between particles and so-called 'coherent structures' of the flow. A coherent structure comprises some spatio-temporally compact region of the flow over which some macroscopic quantity (such as velocity, vorticity, or kinetic energy) is strongly

correlated. Figure 3.1 shows schematics of near-wall turbulent coherent structures for flow between two parallel plates. In coherent structure, quasi-streamwise vortices form, as shown in Figure 3.1. If a particle is between clockwise vortex and a counter-clockwise vortex, it is pushed away from the wall. This kind of particle motion is called 'ejection' and is linked to low-speed streak of the flow near the wall. The quasi-streamwise vortices also result in particle motion towards the wall (called 'in-sweep') which is correlated to the high-speed regions [138].
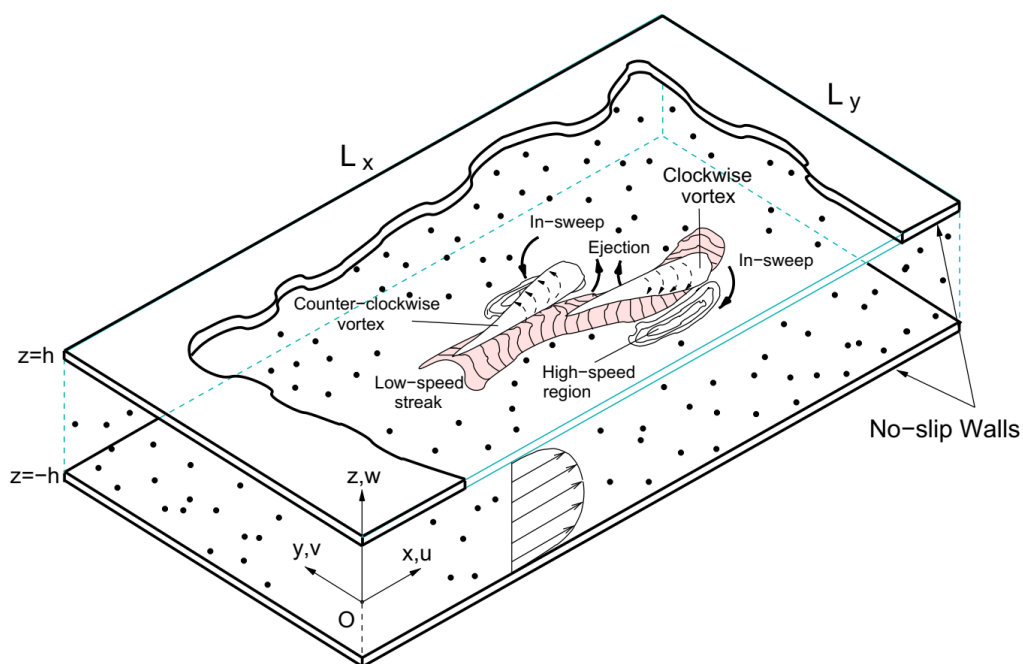
Figure 3.1 Schematics of near-wall turbulent coherent structures in a particle-laden turbulent gas flow between two parallel plates: ejection denotes particle motion away from the wall and in-sweep indicates particle motion towards the wall; low-speed streak and high-speed region close to the wall result in formation of quasi-streamwise vortices which are responsible for particle motion in wall normal direction [138].

To solve the coherent structures and their interaction with particles explicitly, it is crucial to conduct Direct Numerical Simulation (DNS) with superfine mesh [138]. The DNS calculation is not practical for engineering applications. Therefore, here an alternative near-wall model, taken from Guingo and Minier [139], has been applied to mimic particle

motion in the coherent structures by a stochastic approach. This model comprises a succession of simple sub-models instead of one complex model for the coherent structures. As shown in Figure 3.2 and described in the previous section (§3.2.2), transport of the particle in the bulk ($y^+ \geq 100$, according to the law of the wall) is treated by the random walk model. When a particle enters into the turbulent boundary layer ($y^+ < 100$), the near-wall stochastic model controls the particle motion. In the present work, the laminar sublayer is neglected due to the wall roughness. Further explanation of the wall roughness will appear in the next section (§3.3).
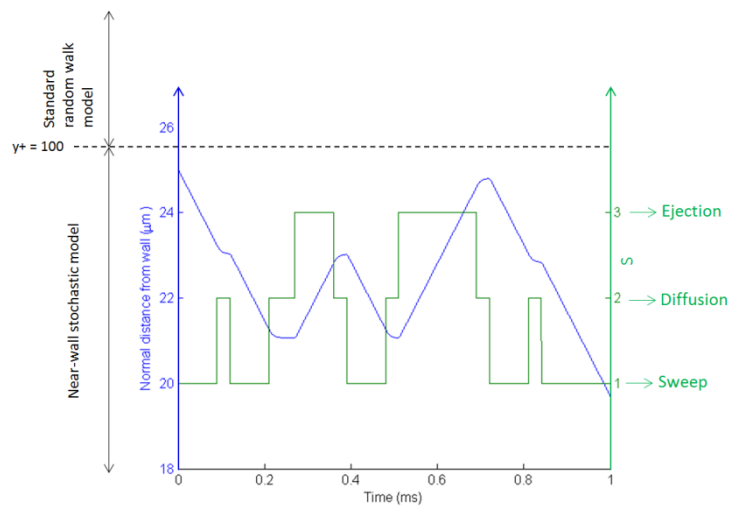
Figure 3.2 An example of alumina particle trajectory in steel melt flow in a near-wall region.

In the turbulent boundary layer, due to the interactions between the coherent structures and the particle, three states of particle motion are considered [139]:

    (1) going towards the wall, called 'sweep';

    (2) moving randomly along the wall direction as called 'diffusion', and,

    (3) escaping from the wall, called 'ejection'.

The state of particle motion is denoted by a S index ($S \epsilon \{1,2,3\}$): 1 for sweep, 2 for diffusion, 3 for ejection. The state of motion, i.e. S index, jumps randomly between 1, 2 and 3 with time corresponding to changes from one coherent structure to another. It means that

random S index is a function of time, $S(t)$. Currently, there is no robust function to define the lifetime for the state of motion, τ_s. According to the dimensionless values suggested by [139], the following equation is used to find τ_s.

$$\tau_s = \begin{cases} -9T_L\ln(r), & S(t) = 1, 3 \\ -3T_L\ln(r), & S(t) = 2 \end{cases}.$$

(3.17)

T_L is the Lagrangian time scale (10^{-6}-10^{-5} s), and dependency of the modeling result on this value will be analyzed in next sections. r is a random number between 0 and 1.

In the near-wall region, the velocity of fluid and particle is calculated in a local coordinate system where a component should be in wall normal direction. If the local coordinate system is not coincident with the global coordinate system of simulation, the results of near-wall region must be converted to the global system. The wall-normal component of the fluid velocity in the boundary layer seen by the particle is defined as 'velocity seen', u_s. A simple expression is proposed:

$$u_s = \begin{cases} -\sqrt{0.39k} & , \ S(t) = 1 \\ \frac{T_L}{T_L+dt}\left(u'_s + KdW(t)\right), & S(t) = 2. \\ \sqrt{0.39k} & , \ S(t) = 3 \end{cases}$$

(3.18)

u_s for the state of sweep and ejection is estimated according to the fluid velocity in the coherent structure $\sqrt{0.39k}$, where k is turbulence kinetic energy (personal communication with C. Henry, 2016). The velocity seen for the state of diffusion is progressively calculated, based on the value of the last (Lagrangian) time step, u'_s, by adding a noise term, KdW. The initial value of u'_s is taken as the fluid velocity. $K = 0.68\sqrt{k/T_L}$ is the diffusion coefficient and $W(t)$ is the Wiener process, whose increments $dW(t) = W(t + dt) - W(t)$ represent the effects of a noise term [140]. Here, $dW(t)$ is a Gaussian random number with mean value of 0, and variance equals particle time step.

Based on the u_s, the wall normal velocity of the particle, u_p, can be calculated as

$$\frac{du_p}{dt} = \frac{u_s - u_p}{\tau_p} + K_{Br} \frac{dW}{dt},$$ (3.19)

τ_p is the particle relaxation time, $\sqrt{4\rho_p d_p/(3\rho C_D |u_s - u_p|)}$. Again, a so-called *white-noise term* is considered according to the Wiener process, where K_{Br} is velocity diffusion term [139].

$$K_{Br} = \sqrt{\frac{2k_B T}{m_p \tau_p}},$$ (3.20)

where k_B is Boltzmann constant, m_p is the mass of the particle, and T is the fluid temperature.

There should be a thin laminar sub-layer adjacent to the wall. Here, this layer is neglected because calculation results using empirical equations of y+ show that the laminar sub-layer is very thin due to the wall roughness in this particular case.

3.3 Adhesion mechanism

Interaction between non-metallic inclusions (NMI) in molten steel and the SEN wall, made of refractory material or ceramic, is an important subject for metallurgists [81,82,86,87,89]. Findings show that capillary force, also termed adhesion force, is the main reason for particles adhering to the wall. Adhesion force is, in fact, due to the surface tension of the melt on a meniscus formed between the NMI particle and SEN wall. When the particle approaches the wall, a rupture of the disjoining liquid film between them occurs. Then, the fluid is drained out of the particle-wall contact because of the low wettability of alumina by steel melt and gas capillary forms [86]. A comparison of capillary force and other forces which might push the particle away from the wall, like drag force and lift force, shows that

capillary force is at least a few orders of magnitude larger. Therefore, one can conclude that once the capillary force is imposed, the particle remains attached to the wall [81,82,86,89]. Moreover, the sinter bond between the alumina particle and SEN wall (or attached particle) forms rapidly at high temperatures [87]. In another case, low pressure develops in the SEN (e.g. in the gap between the stopper rod and the top of the SEN). This low pressure probably leads to degassing of the liquid steel. Accordingly, cavities on the surface of the particle and pores of the SEN wall act as nucleation sites for gas bubbles [9]. Thus, when a particle comes into contact with the SEN wall, a gas bubble may already exist between them. This may raise the tendency towards clogging in the upper part of the SEN. Therefore, considering the aforementioned aspects, it is assumed that the NMI particles stick to the SEN wall as they are brought to the wall by the flow. This means that the rate-controlling step is the transport of particles from the bulk molten steel to the wall.

The surface roughness of the SEN wall plays a crucial role in the fluid flow near the wall; hence, it influences the transport of the particles to or from the wall. To model the wall roughness effects, the law-of-the-wall for mean velocity is modified using an additive term which depends on the nature and size of troughs and hollows causing the roughness. This term has been found to be well-correlated with the dimensionless roughness height, $K_s^+ = \rho K_s u^*/\mu$, for a uniform sand-grain roughness, as shown in Figure 3.3. K_s is the physical roughness height. u^* is a velocity function which is determined by the turbulence kinetic energy (k) with a relation, $u^* = C_\mu^{1/4} k^{1/2}$, where C_μ is a turbulence constant [137]. The wall roughness influences the turbulence kinetic energy (k) of the flow, which in turn influences particle motion in the boundary layer (§3.2.3).
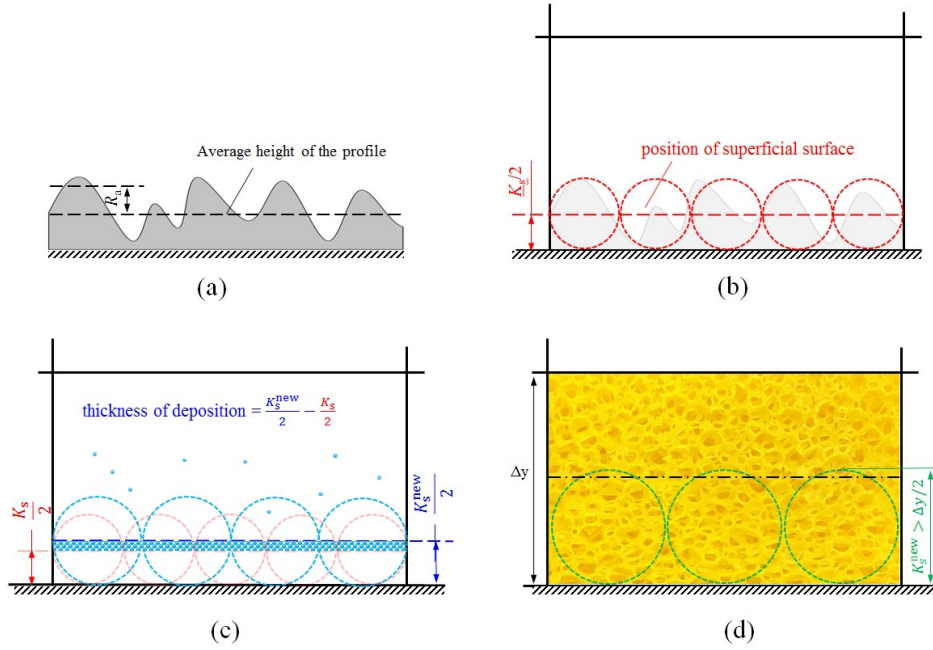
Figure 3.3 Change of roughness by particle deposition: (a) an arbitrary roughness profile, (b) equivalent sand-grain roughness, (c) increase in roughness height due to the particle deposition, (d) convert cell to a porous medium.

Deposition of particles on the wall alters the wall roughness. In the current model, the change of the wall roughness resulting from particle deposition is considered. The initial surface roughness profile, given by experimental measurements, should be converted to an equivalent sand-grain roughness. Adams et al. suggest a simple algorithm to relate the measured surface roughness to an equivalent sand-grain roughness [141], as shown in Figure 3.3.

$$K_s = 5.863\bar{R}_a, \tag{3.21}$$

where $\bar{R}_a$ is the arithmetic average of distances of the surface profile from the average height of the profile. An arbitrary roughness profile and the average height of asperities are plotted in Figure 3.3(a). The equivalent height as sand-grain roughness in the control volume (cell) is illustrated in Figure 3.3(b).

To implement the unsteady change of roughness due to the particle deposition, an increase of the deposited material is simply considered as an increase of sand grain height in each computational cell adjacent to the wall. The deposited particles are deleted from the calculation domain. As shown in Figure 3.3, in every time step the thickness of deposited material on the wall is calculated as K_s^{new}. It is noteworthy that the deposited material, here also named as 'clog', is porous, and the average solid volume fraction of the clog ($\bar{f}_p$) can be determined experimentally. Therefore, in the calculation of the thickness of the deposition ($(K_s^{new} - K_s)/2$) the porosity of the clog must be taken into account.

If K_s^{new} grows by more than half of the cell size ($\Delta y/2$), the current computation cell adjacent to the wall surface is treated as porous medium, marked in yellow (Figure 3.3 (d)). It is assumed that the whole SEN surface, which belongs to the current computational cell, is fully covered by the deposited particles. The change of the cell's status to yellow announces the termination of step (b) and the beginning of step (c) in Figure 2.7, i.e. the clog growth. Cell status is explained in the next section.

3.4 Clog Growth

Metallographic analysis (SEM) of the clogged nozzle of a pilot plant setup [80,142] has shown that clog material is porous (Figure 3.4). A large part of the clog is composed of non-metallic inclusions (NMIs), e.g. alumina, which forms a porous network. Furthermore, distribution of the NMIs in the clog is not homogenous. The clog is described with following parameters: the diameter of alumina particle d_p, the average solid volume fraction of the clog $\bar{f}_p$, and the diameter of large pores D_{pore}. As shown in Figure 3.4, some large pores with size of D_{pore} exist. All those parameters can be determined experimentally, and they are used as input parameters for building the clog growth model. The growth of the clog is governed by the deposition of NMI particles. One assumption is that particles

reaching the clog front completely stick (100% sticking probability), with no detachment and no fragmentation phenomenon occurring.
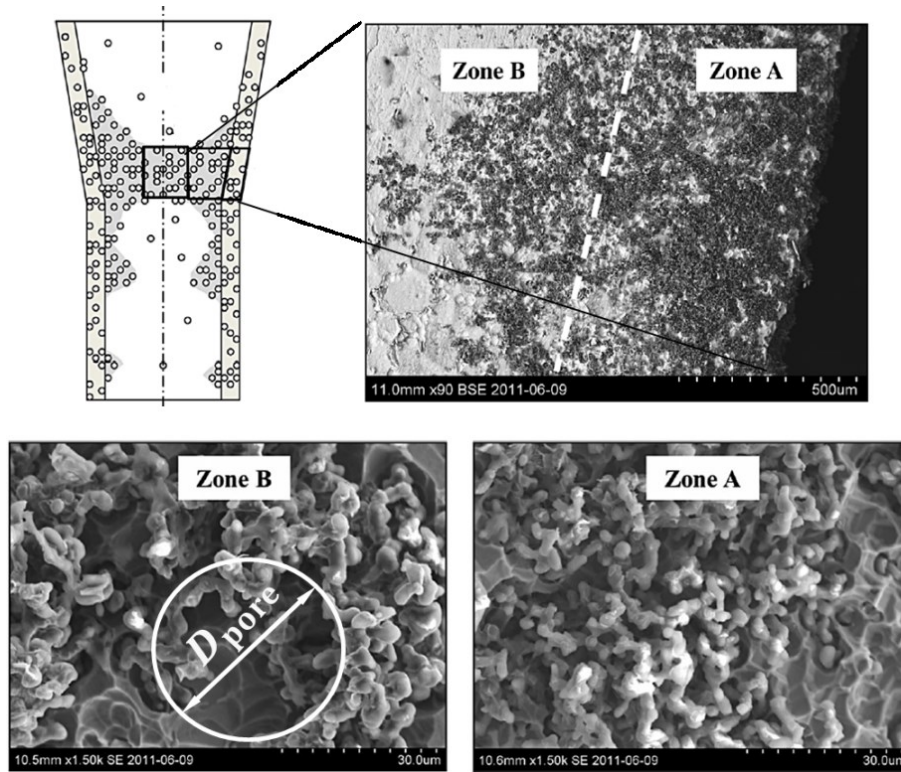
Figure 3.4 Metallographic analysis (SEM) of the clog material (alumina) in the nozzle of a pilot experiment [80].

In order to describe the algorithm of clog growth, another quantity is introduced: f_{clog}. As shown in Figure 3.5, f_{clog} describes the fraction of the volume which is occupied by the clog in the local computational cell. Additionally, following cell markers are defined:

1. All computational cells, including the boundary cells which are adjacent to the nozzle wall, are initially marked as 'white' cells. NMI particles can only possibly deposit on the wall (Figure 3.5(a)). The wall is gradually covered by the deposited particles, initiating the clog growth. f_{clog} is initialized as 0.0. The algorithm for the early stage of clogging, i.e. increasing the wall roughness, is described in §3.3

2. When the roughness height is larger than half of the cell thickness (i.e. $f_{clog} > 0.5$), the boundary cell is marked as 'yellow' (Figure 3.5(b)). Inside yellow cells, growth

of the clog occurs, and f_{clog} increases continuously with the progress of the deposition of NMI particles on the clog front. f_{clog} increases from the initial value of 0.5 to 1.0 in the boundary cells.

3. When f_{clog} reaches 1.0, the cell marker converts into 'red'. The face-bonded neighboring cells (Figure 3.5 (c)) are marked as 'yellow'. The clog continues to grow in the yellow cells. Inside the red cells, the average solid volume fraction of the clog ($\bar{f}_p$) remains constant.
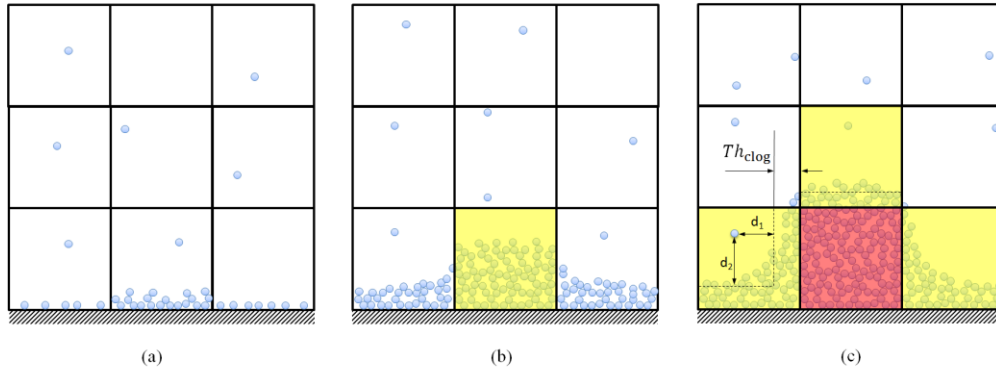
Figure 3.5 Origin and growth of the clog: (a) initial deposition of particles on the wall, (b) start the growth of the clog, (c) continuous growth of the clog into the bulk region.

Making a decision on how a particle adheres to the clog front in a yellow cell depends on its distance to the clog front (Figure 3.5(c)). The clog front (dash line) is calculated by assuming there is a uniform distribution of clog on mutual faces with neighboring red cells or nozzle-wall in a yellow cell. In other words, the clog volume in a yellow cell is divided by the total area of mutual faces with a neighboring red cells or wall. Thus, uniform thickness of the clog in a yellow cell is assumed, as in the following equation:

$$Th_{clog} = \frac{f_{clog}\Delta V}{\sum A_{face}}, \tag{3.22}$$

where ΔV is the volume of the cell, and A_{face} is the clog face area of the cell.

After a particle enters a yellow cell, its distances from the clog front are calculated. If the minimum distance is smaller than the radius of the particle ($d_p/2$) it will adhere to the clog front. The volume of the clog increases by $\pi d_p^3/(6\bar{f}_p)$ in the yellow cell and the particle is no longer considered in further calculations. In the numerical calculation, the volume increase of the clog can be multiplied by an artificial factor (N-factor), explained in §5.1.2 This procedure is shown in the flowchart of Figure 3.6.
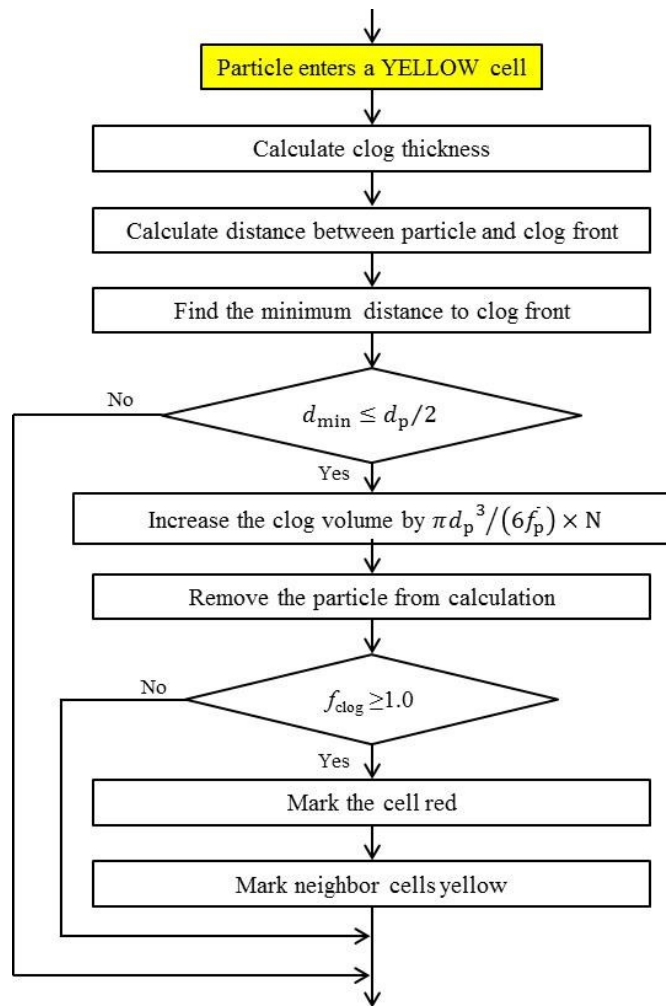
Figure 3.6 Flowchart for clog growth.

To incorporate the porous structure of the clog in flow calculations, the permeability of the clog is required. The permeability is treated as a function of the average solid volume fraction of clog $\bar{f}_p$, the diameter of large pores D_{pore} and the fraction of clog in the considered cell f_{clog}.

$$K_{\text{per}} = \frac{\left(1-\bar{f}_{\text{p}}\right)\left(1-\bar{f}_{\text{p}}^{1/3}\right)}{108\left(\bar{f}_{\text{p}}^{1/3}-\bar{f}_{\text{p}}\right)} D_{\text{pore}}^2 \frac{1}{f_{\text{clog}}^n}, \tag{3.23}$$

where n is an interpolation correction power. The above expression is a modified equation of what was presented by Yang [143] for isotropic porous media with large open pores. For denser porous clog conventional Kozeny–Carman equation for packed bed of spheres, $K_{\text{per}} = d_{\text{p}}^2/180 \cdot \left(1-\bar{f}_{\text{p}}\right)^3/\bar{f}_{\text{p}}^2$, can be applied.

Then, Darcy source terms for the clog region are defined as below for $\vec{u}$, k, and ω, respectively.

$$\vec{S_u} = -\frac{\mu}{K_{\text{per}}}\vec{u}. \tag{3.24}$$

$$S_k = -\frac{\mu}{K_{\text{per}}}k. \tag{3.25}$$

$$S_\omega = -\frac{\mu}{K_{\text{per}}}\omega. \tag{3.26}$$

3.5 Non-isothermal clogging

If the melt superheat is low, and the heat loss from the SEN wall is high, the steel may freeze on the SEN wall. Rackers and Thomas [71] stated that when an alumina network forms on the SEN wall, the steel may solidify in the pores. The solidified steel reinforces the whole clogging region. In the other words, the solidified steel can increase the clog strength; the clog can withstand against the melt flow and cannot be washed away by the flow drag force. It can be also concluded that solidification within the SEN will increase clogging rate. The practical evidence in steel plant [1] showed that increasing SEN preheating temperature reduces the clogging tendency within SEN. It means that SEN preheating prevents or postpones solidification of steel within the clog material. Therefore,

the performance of the SEN is improved. Moreover, post-mortem microscopic analysis of clog materials always shows solidified steel filling clog networks [78]. However, it is not clarified that the solidification of steel has occurred during the casting process or the steel inside the clogging material was in liquid state and solidification occurs after sampling. Here, the model is upgraded to consider the non-isothermal conditions and solidification of steel in the clog. An enthalpy based solidification model of mixture continuum is implemented. The mixture comprises three phases: liquid (ℓ), solid (s), and particle (p), as shown in Figure 3.7 schematically. Therefore,

$$f_s + f_\ell + f_p = 1. \tag{3.27}$$
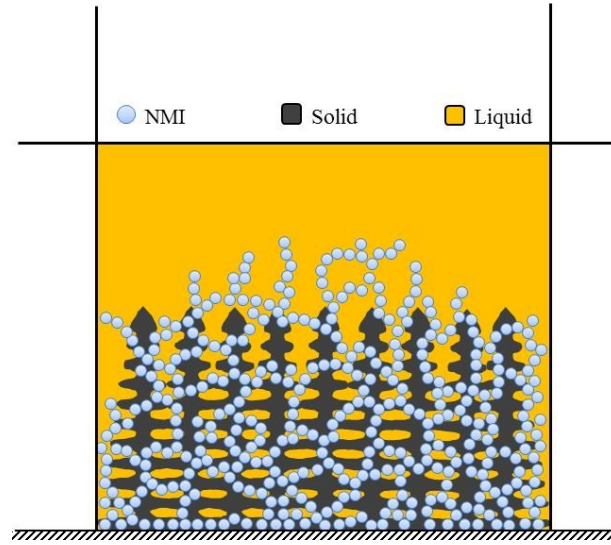
Figure 3.7 Schematic of three phases in a computational cell.

The enthalpy equations for these three phases are

$$\begin{cases} \frac{\partial}{\partial t}(f_\ell \rho_\ell h_\ell) + \nabla \cdot (f_\ell \rho_\ell \overrightarrow{u_\ell} h_\ell) = \nabla \cdot (f_\ell k_\ell \nabla T_\ell) + Q_{\ell s} - Q_{\ell p} + Q_\ell^s \\ \frac{\partial}{\partial t}(f_s \rho_s h_s) \qquad\qquad = \nabla \cdot (f_s k_s \nabla T_s) + Q_{\ell p} - Q_{sp} + Q_s^s, \\ \frac{\partial}{\partial t}(f_p \rho_p h_p) \qquad\qquad = \nabla \cdot (f_p k_p \nabla T_p) + Q_{\ell p} - Q_{sp} \end{cases} \tag{3.28}$$

where $Q_{\ell p}$, $Q_{\ell p}$, and Q_{sp} are enthalpy exchange terms which balance the temperature among all phases: $T_\ell \approx T_s \approx T_p = T$. Q_ℓ^s and Q_s^s are source terms which consider the latent heat: $Q_\ell^s = f_\ell L M_{\ell s}$ and $Q_s^s = f_s L M_{\ell s}$. $M_{\ell s} = \rho_s \frac{\partial f_s}{\partial t}$ is the mass transfer rate from liquid to solid steel by solidification.

If enthalpy equations for three phases are added together,

$$\frac{\partial}{\partial t}\begin{pmatrix} f_\ell \rho_\ell h_\ell \\ +f_s \rho_s h_s \\ +f_p \rho_p h_p \end{pmatrix} + \nabla \cdot (f_\ell \rho_\ell \overrightarrow{u_\ell} h_\ell) = \nabla \cdot \begin{pmatrix} f_\ell k_\ell \nabla T_\ell \\ +f_s k_s \nabla T_s \\ +f_p k_p \nabla T_p \end{pmatrix} + (1 - f_p) L \rho_\ell \frac{\partial f_s}{\partial t}. \tag{3.29}$$

Assuming an average heat conductivity $\bar{k} = f_\ell k_\ell + f_s k_s + f_p k_p$ and mixture velocity $\vec{u} = f_\ell \overrightarrow{u_\ell}$, the enthalpy equation is reduced as

$$\frac{\partial}{\partial t}\begin{pmatrix} f_\ell \rho_\ell h_\ell \\ +f_s \rho_s h_s \\ +f_p \rho_p h_p \end{pmatrix} + \nabla \cdot (\rho_\ell \vec{u} h_\ell) = \nabla \cdot (\bar{k} \nabla T) + (1 - f_p) L \rho_\ell \frac{\partial f_s}{\partial t}. \tag{3.30}$$

If a similar Boussinesq approximation is made for the enthalpy equation by assuming that particle phase has similar thermal properties of steel, i.e. $\rho_p = \rho_\ell$ and $h_p = h_\ell$, the enthalpy equation for the mixture is simplified to

$$\frac{\partial}{\partial t}(\rho h) + \nabla \cdot (\rho \vec{u} h) = \nabla \cdot (\bar{k} \nabla T) + (1 - f_p) L \rho \frac{\partial f_s}{\partial t}. \tag{3.31}$$

When solidification is taken into account, the drag of the solidifying mushy zone on the melt flow has to be considered in addition to drag of the clog ($S_{clog,\phi}$), defined in equations (3.25) - (3.27). Hence, a corresponding source term is defined for the mushy zone.

$$S_{\text{solidification},\phi} = \frac{(1-f_\ell)^2}{(f_\ell)^3} \frac{\mu}{6 \times 10^{-4} (\lambda_1)^2} \phi, \tag{3.32}$$

where λ_1 is the primary dendrite arm spacing and ϕ can be velocity, kinetic turbulence energy, or its dissipation rate.

The applied source term is an average of the clog and the solidification terms according to the particle volume fraction (f_p).

$$S_\phi = f_p S_{clog,\phi} + (1 - f_p) S_{solidification,\phi}. \tag{3.33}$$

4. Validation

4.1 Benchmark

A laboratory device as used to investigate the nozzle clogging Figure 4.1 is simulated [63,80,103,142,144]. This device is made from a pilot scale induction furnace and a nozzle with circular section as situated at the bottom of the furnace. The nozzle is heated to a temperature above the melting point of the melt, to prevent the nozzle from freezing during the run of the experiment. Steel is melted in the induction furnace and deoxidized with aluminum. After a certain holding time for de-oxidation, the nozzle is opened and the molten steel flows through the nozzle. The melt is poured into a container from the nozzle. The mass flow rate is dynamically monitored by weighing the mass of the steel as it is collected by the container. The poured melt is exposed to air and the oxidation of the melt might affect the measurement of the mass flow rate. However, an experimental study on oxidation rate of molten steel [145] showed that the oxidation rate in the still state is controlled by the diffusion of oxygen in the oxide film and in the stirred state is controlled by the diffusion of oxygen in the gas phase. In both cases the diffusion is a very slow step; therefore, the effect of the melt oxidation on the weight measurement is negligible.

Dimensions of the computational domain with enmeshment are shown in Figure 4.2. A finer mesh is generated in the nozzle region where clogging may occur. The minimum cell size,

$5.63 \times 10^{-12} \, \text{m}^3$, is located near the nozzle wall; the maximum cell size, $1.3 \times 10^{-5} \, \text{m}^3$, is located in the furnace.
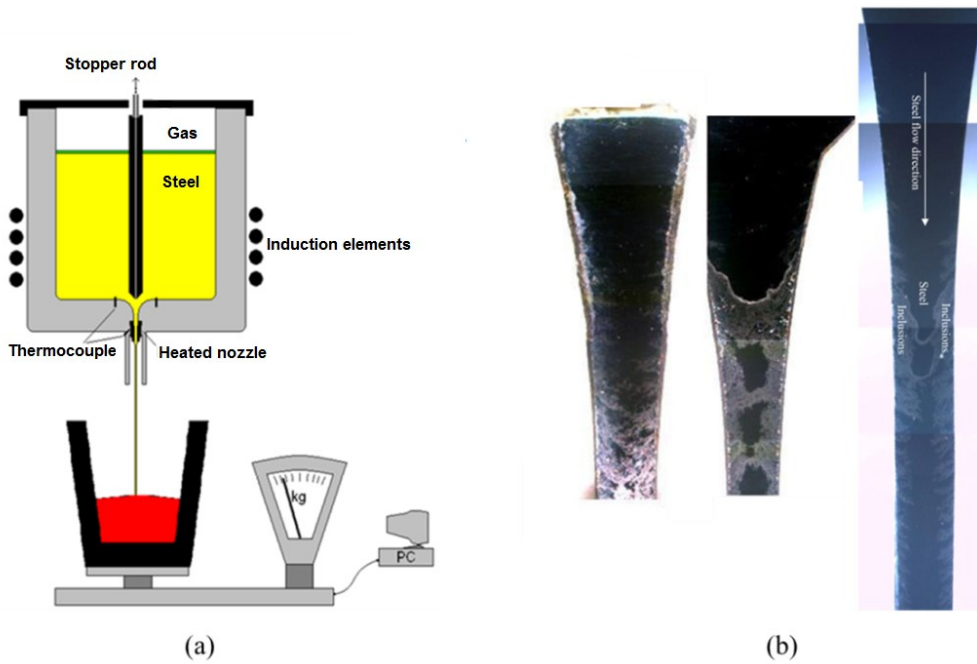
Figure 4.1 Schematic of a laboratory device to investigate the clogging (a) and typical macrographs of as-clogged nozzle (b). The narrowest part of the clean nozzle (non-clogged nozzle) has a diameter of 5 mm [144].
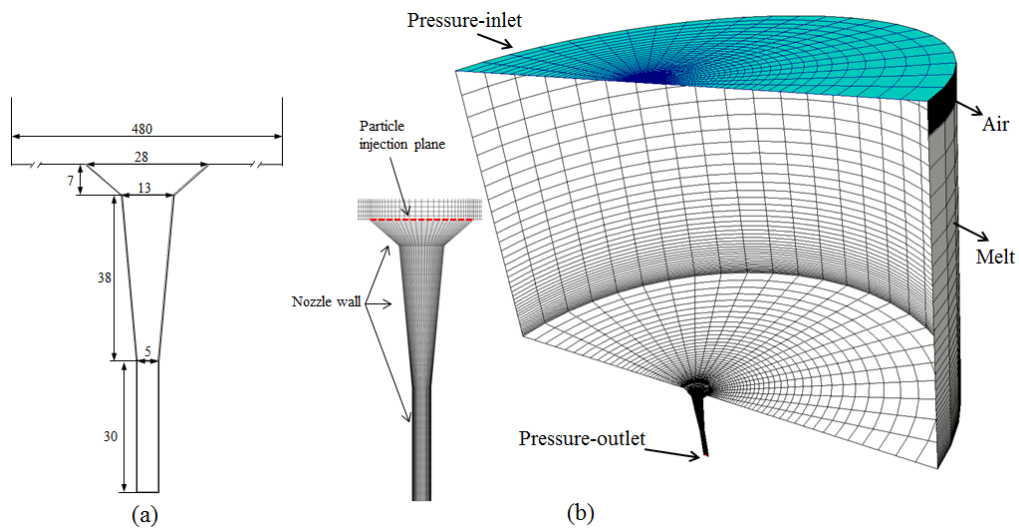
Figure 4.2 Dimensions in mm of the computational domain (a) and illustration of the mesh with boundary conditions (b).

A volume of fluid (VOF) method is applied to calculate the two-phase (melt and gas) flow.

In laboratory experiments using this device, liquid argon is added to provide an Ar

atmosphere in the furnace in order to prevent any possible re-oxidation of the steel. However, here, simply the density and viscosity of air are taken for the gas phase, like the previous simulation for this device [116]. On the top surface of the furnace, a pressure-inlet boundary condition with atmospheric pressure is set for the air. For the nozzle outlet, a pressure-outlet is applied for the melt flow. Non-slip boundary conditions are valid on all other walls. 350 kg of steel melt is filled in the furnace before running the experiment. To this end, the melt height is 0.275 m and there is a layer of air 20 mm thick on top of the melt. The velocity, turbulence kinetic energy k, and specific dissipation rate ω are set to zero as initial conditions. The melt drains through the nozzle by gravity, and the air continuously flows in through the pressure-inlet. The initial roughness height on the nozzle wall is 2×10^{-5} m, which increases as the particles deposit.

To save computation time and avoid redundant calculations of particle tracking in the furnace, particles are injected on the connection plane between the bottom of the furnace and the top of the nozzle, as shown in Figure 4.2. A previous simulation has demonstrated that particle distribution in the induction furnace is quite uniform due to two reasons. Firstly, the melt is agitated by electromagnetic force. Secondly, the particle size is only a few micrometers. The drag force of the melt on the particles is dominant; hence particles follow the melt flow in the furnace. The particle mass-injection-rate is set proportionally to the mass flow rate of the melt. When the mass flow rate of the melt decreases due to clogging, the particle mass-injection-rate is reduced proportionally. The diameter of each particle is set at 3 μm regarding the average diameter of alumina inclusions as reported in [80]. Since accurate mass-injection-rates are not available, it is assumed to be ~9.79×10^{-6} kg/s initially as a suitable parameter; this value is discussed in §4.2 .

Physical properties of different phases (steel melt, alumina particles, and air) and other parameters as required by the model are listed in Table 4.1. A full 3D calculation is made and the numerical model is implemented in the commercial CFD code ANSYS-FLUENT

14.5 with the extended user defined functions (UDFs) for considering the particle motion near the wall and the clog growth. Shear-stress transport (SST) k-ω model is used to model turbulent flow which effectively blends the precision and robustness of k–ω model in the near-wall region with the bulk liquid k–ε modeling in the far field. A key point of this model is insensitivity of flow to grid spacing near the wall. A detailed explanation can be found in [146,147]. The absolute convergence criteria for all transport equations are set to 1×10^{-4} and the under-relaxation factor is 0.3, 0.5, 0.8, and 0.8 to solve equations of continuity, momentum, k, and ω, respectively. Time step size is defined as 0.01 s during the simulation. Computation is done on a high-performance computer cluster with 6 CPUs (2.9 GHz), and the computation for each simulation takes approximately 6 days.

Table 4.1 Physical properties, process and numerical parameters

Property	Unit	Value
Density		
Steel melt	$kg.m^{-3}$	7020
Alumina (solid)		3700
Air		1.225
Viscosity		
Steel melt	$kg.m^{-1}.s^{-1}$	0.006
Air		1.7894×10^{-5}
Particle diameter	m	3.0×10^{-6}
Time step for flow	s	0.01
Lagrangian time scale (T_L)	s	1.0×10^{-5}
Average volume fraction of solid particles ($\bar{f}_p$)	-	0.5
Pore diameter in clog (D_{pore})	m	3.0×10^{-5}
Initial melt height in the furnace	m	0.275
Initial nozzle wall roughness	m	2.0×10^{-5}
Initial particle mass-injection-rate	$kg.s^{-1}$	9.79×10^{-6}
N-factor *	-	600

* N-factor is an artificial factor explained in §5.1.2 .

4.2 Illustrative results

The flow pattern before injecting the particles is depicted in streamlines (Figure 4.3(a)). At this moment, the nozzle wall is considered to be 'clean', i.e. the wall has only the initial

wall roughness without any particle deposition on it. In Figure 4.3(b)-(c), the velocity magnitude and turbulence kinetic energy contours are presented on a symmetry plane before and after clogging, respectively. Prior to clogging, the melt flows smoothly through the nozzle. Turbulence begins to appear from the upper part of the nozzle and becomes stronger along the nozzle wall with the gradually-converged nozzle section. After clogging, the striking feature of the flow pattern is the dramatic increase in turbulence with incremental clogging. The maximum velocity does not alter significantly, it even drops slightly. However, the turbulence kinetic energy increases by 5 orders of magnitude in the lower part of the nozzle due to the bumpy clog front and the reduced cross-section of the flow passage (Figure 4.3(c)).
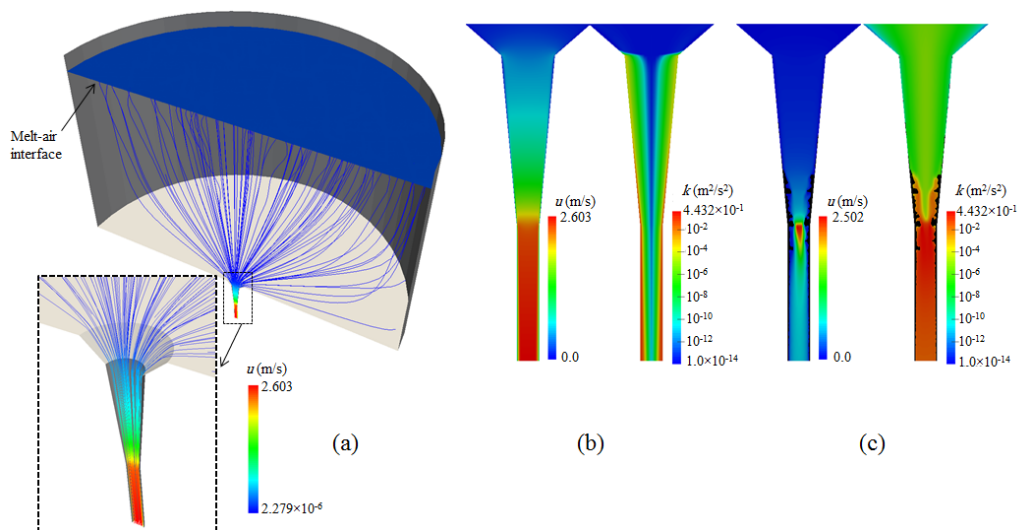
Figure 4.3 Characteristics of the flow patterns with and without considering clogging. (a) Flow pattern in streamlines; (b) velocity magnitude and turbulence kinetic energy of the melt in the nozzle without considering clogging; (c) velocity magnitude and turbulence kinetic energy of the melt in the nozzle considering clogging (200 s after particle injection). The velocity magnitude is shown with color in linear scale, while the turbulence kinetic energy in logarithmic scale. In the case considering clogging, the clog is shown in black.

Possible trajectories of particles are displayed in Figure 4.4. Two different scenarios are analyzed: one is the early stage and the other is the later stage of clogging. During the early

stage of clogging, the nozzle wall is 'clean' with its initial wall roughness, or it is only covered by few deposited particles. This early stage clogging is referred to as the change of the wall roughness height. During the later stage, the growth of the clog is considered, i.e. the front of the clog is tracked explicitly.

Illustratively, three particle trajectories are selected, representing three different fates of the particles.

(1) A particle can follow the bulk turbulent flow and exit from outlet.

(2) A particle is initially transported into the turbulent boundary layer near the wall. Due to the interactions between the coherent flow structures and the particle, the particle is 'ejected' from the wall and returns to the bulk flow [139]. Trajectories of particles, which pass the boundary layer, are represented in green.

(3) A particle is firstly transported into the turbulent boundary layer near the wall and then adheres to the wall. Due to the interactions between the coherent flow structures and the particle, the particle is propelled towards the wall by the 'sweep' action [139].

Similarly, three scenarios for particles exist during the late stage of clogging (Figure 4.4(b)). The clog region is represented in yellow, and the trajectories of particles are shown in blue lines. No turbulent boundary layer can be determined near the front of clog. However, a numerical treatment is performed for the volume element which includes the front of clog. Here the portion of the trajectory is also marked in green when a particle enters the volume element of clog front. A particle entering this clog front element adheres to the clog front, or returns to the bulk flow, depending on the minimum distance the particle can reach the clog front.
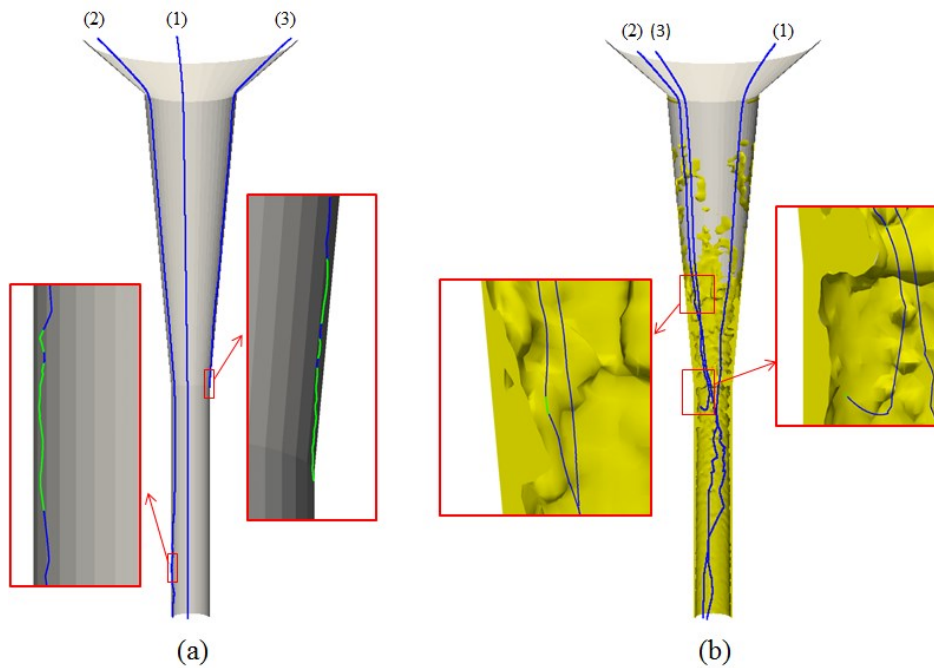
Figure 4.4 Trajectories of particles in the initial stage (a) and later stage of clogging, i.e. 200 s after particle injection (b). Trajectories of three particles are selected to illustrate their different fates: (1) passing through the nozzle with the bulk melt; (2) being transported in the near-wall or partially clogged region, then returned into the bulk melt; (3) being transported in the near-wall or partially clogged region, then adhering to the wall or the clog front. The trajectory of the particle in near-wall or partially clogged region is highlighted in green.

Evolution of clogging is depicted in Figure 4.5(a). At 50s, the narrowest section and a portion of the middle section of the nozzle are covered by a smooth layer of clog. In these sections, the flow near the wall has the largest turbulence kinetic energy (Figure 4.3(b)), which promotes the transverse motion of particles. It appears to be erratic as to where the particle deposition occurs in the middle section. Note that individual particles or tiny amounts of particles deposited on other the uncovered wall of the nozzle may not at all be visible in Figure 4.5. With the continuous deposition of particles on the nozzle wall, the clog starts to grow and some asperities of the clog front can be seen in the period between 100 and 150 s. Snapshots at 200 and 250 s show some bulges of the clog, which grow much faster than those in neighboring regions, and a branched structure develops to a certain

degree. These branched structures are more pronouncedly visible in the transition region between the middle section and the narrowest section of the nozzle. Finally, the branched clogging structures now grow continuously until they meet in the nozzle center, and the cross-section of the nozzle is blocked. In Figure 4.5(b) a zoomed view of clog, overlaid with the flow field in streamlines, is displayed at 200 s. It demonstrates that the formation of the irregular clog front adapts the flow field (streamlines), leading to the formation of eddies. As a result, the adapted flow field influences the trajectories, hence the 'fates' of the particles. For example, the eddy under the necking area causes the trajectory of the particle (3) to bend upwards (Figure 4.4(b)). The particle rises and then adheres to the clog front.
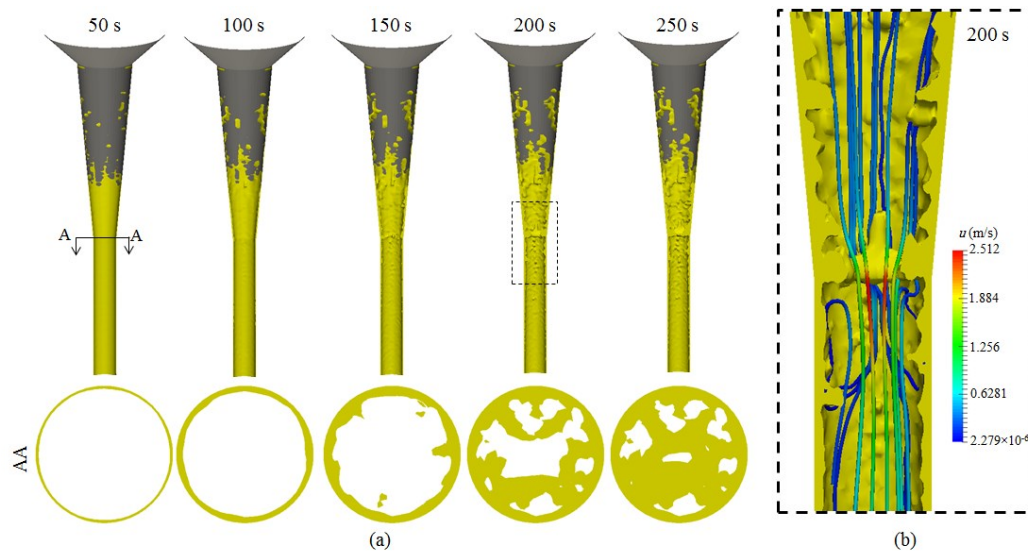
Figure 4.5 Evolution of clogging in the nozzle. (a) View of the clog region from the vertical section and a cross-section A-A of the nozzle; (b) Zoomed view of the flow streamlines and a partially clogged section at 200 s. The clogged section is shown in yellow. The magnitude of the flow velocity is shown in a color scale along the streamlines.

The total mass of the clog, i.e. the mass integral of particles as deposited on the nozzle wall and on the clog front, and the deposition rate are plotted as functions of time in Figure 4.6(a). The curve of the total particle deposition mass appears relatively smooth, but the mass deposition rate varies significantly. This variation coincides with the aforementioned

periods of clogging, as shown in Figure 4.6(b). (1) The initial covering of the nozzle wall by the deposited particles. The deposition rate increases initially, then decreases and fluctuates until 80 s. (2) The build-up of the bulged clog front. The deposition rate is almost constant with minor fluctuations. This period lasts from 80 to 180 s. (3) The build-up of the branched structures of clog. The deposition rate decreases rapidly. This period starts at about 180 s, ending with complete blockage of the nozzle. Totally, ~34% of the injected particles entering the nozzle attach to the wall/clog and stop the flow after about 250 s.
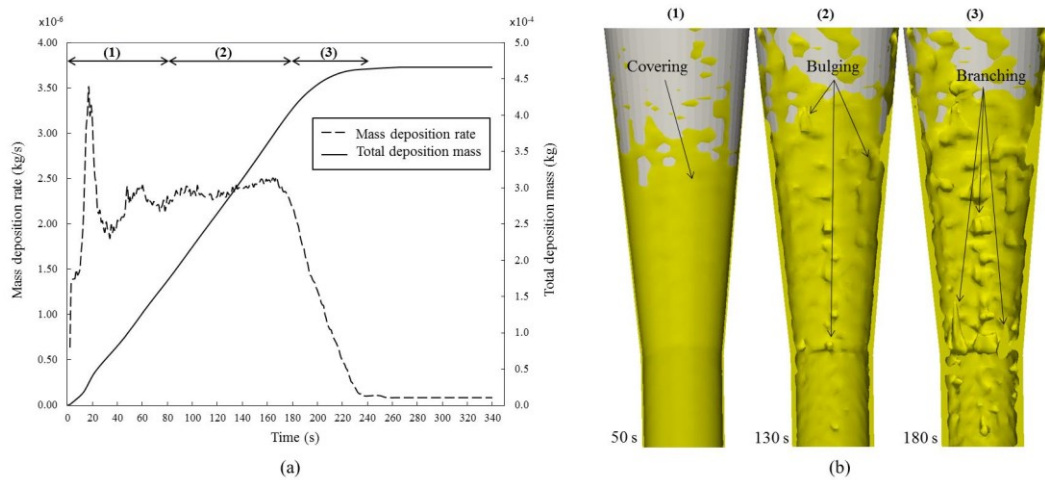
Figure 4.6 Numerically calculated total mass of the clog, i.e. the mass integral of particles as deposited on the nozzle wall and on the clog front, and the mass deposition rate are plotted as functions of time (a). Three periods of clogging evolution are indicated (b): (1) initial covering of the nozzle wall by the deposited particles, (2) developing a bulged clog front, and (3) developing the branched clog structure.

The as-clogged nozzle section obtained by simulation is similar to typical experimental ones. The experiment demonstrates that inclusions tend to deposit on the narrow passage of the nozzle (Figure 4.1(b)) [63,144], and this is well 'reproduced' by the model, as can be seen in Figure 4.5. We, therefore, claim that the model is able to predict the clog growth qualitatively sufficiently well. A quantitative comparison of melt flow rates between the simulation and experimental results exhibits some differences (Figure 4.7). For instance, in

the simulation the flow is stopped by clogging sooner than was the case in the experiment. In the final step of the clogging, after clog branches begin to develop, only small holes are left in the clogged nozzle-section, as depicted in Figure 4.5(a). Owing to the fact that the current mesh size (as limited by the computer hardware) is not able to resolve the holes precisely, the melt flow is blocked earlier in the simulation than it does in reality. It is anticipated that if the mesh is fine enough to resolve the clog front properly, the time of nozzle blockage will be later, closer to what is the case in reality. Another reason for the inaccuracy in the calculation might be due to the volume average method. This method is not oriented to the structural details of the clog at the microscopic scale, but to a reasonable approximation of the clog growth.

The particle deposition rate is definitely related to the particle number density in the melt, i.e. the particle mass-injection-rate, as set in the model; a higher mass-injection-rate leads to faster clogging. The value for the particle mass-injection-rate used in the validation simulation, $\sim 9.79 \times 10^{-6}$ kg/s, is around 67 times smaller than what was obtained from the melt analysis during the experiment [80], $\sim 6.55 \times 10^{-4}$ kg/s. Applying the experimental values in the model leads to rapid blockage of the nozzle, therefore, it is not applicable to the simulation. According to the data from a steel plant for ULC IF steel grades [148], the mass fraction of alumina inclusions in the steel melt would be 4.25×10^{-5}–8.5×10^{-5}, while the mass fraction of alumina inclusions was $\sim 7.3 \times 10^{-3}$ for the laboratory experiment [80]. It illustrates that reported values of the number density of inclusions in the laboratory experiment, extracted from melt samples, may be calculated inaccurately or they do not represent the number density of inclusions which enter the nozzle. The mass fraction of inclusions in the simulation is 3.26×10^{-5}, which coincides well with the data from the steel plant. From an alternative perspective, in the current model, the sticking probability of a particle when it reaches the nozzle wall or clog front is considered to be 100%. This assumption may underestimate the number density of inclusions required to block the

nozzle. Therefore, deeper investigations and more robust evidence are going to be required to ascertain the sticking probability.

4.3 Comparison with experimental data

The numerically predicted clogged nozzle, shown in Figure 4.5, is qualitatively comparable with typical as-clogged cross-sections of the nozzle from laboratory experiments (Figure 4.1(b)). The total mass and the mass flow rate of the steel melt as drained-out from the nozzle are measured experimentally, and they are plotted as functions of time [80]. A Comparison with the numerically simulated results is made in Figure 4.7. Generally, the tendencies of the experimental curves are well-predicted by the numerical simulation, but the details of the experimental curves are still not ideally 'reproducible'. For example, the model underestimates the mass flow rate for the first 60 s, overestimates it between 60 and 180 s, and again underestimates it after 200 s. One reason for this deviation is the model's inaccuracy, but it is also noteworthy that the experimental data was obtained by measuring the force as applied by the exiting melt on the container (Figure 4.1(a)). The momentum impact of the falling melt stream is ignored in this experiment. Additionally, the model might overestimate the clogging. As seen from Figure 4.7, the nozzle is predicted to be fully clogged at about 230 s, while the experiment shows that the mass flow through the nozzle does not halt until around 300 s.

Figure 4.7 The total mass and the mass flow rate of the steel melt as drained from the nozzle are measured and plotted as functions of time [80]. They are then compared with the numerically simulated results.

4.4 Numerical uncertainties

4.4.1 Problem description

To facilitate the model verification, a reduced calculation domain was taken into account, as shown in Figure 4.8. Correspondingly, a free-slip condition for the side surface and a constant mass flow rate for the inlet at the top surface are applied. The nozzle's geometry and the boundary conditions for the nozzle walls remain unchanged (Figure 4.2). With these simplifications, no air phase is involved. The initial roughness height of the nozzle wall is 2×10^{-5} m. The mass flow rate for the melt at the inlet is 0.3 kg/s, the same as the initial mass flow rate in the laboratory experiment (Figure 4.7). Particles with a mass rate of 5.02×10^{-5} kg/s and a diameter of 5 μm are injected onto a horizontal section, 10 mm above the nozzle. Note that these special boundary conditions and settings have been designed for the purpose verifying this model, and they are not compatible with the previous experiment.

Constant mass flow rate

25 mm   60 mm   Free-slip

Non-slip

Pressure-outlet
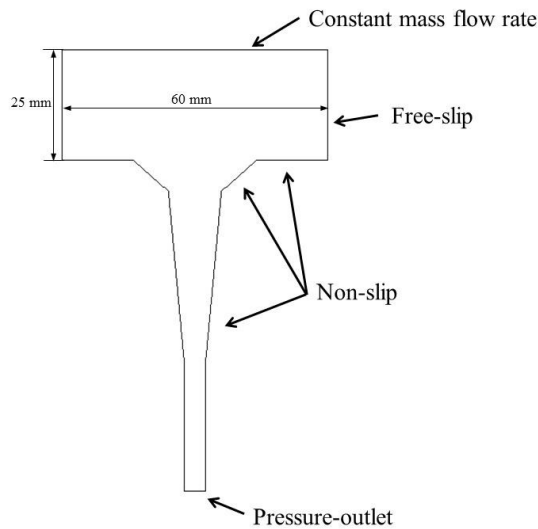
Figure 4.8 Geometry and boundary conditions of the calculation domain are adapted for the purpose of model verification.

4.4.2 Mesh size sensitivity

Different mesh sizes have been created for this study, and distribution of the mesh is not homogenous in the computational domain. The near-wall region is the most important, hence the finest mesh, as noted by its cell thickness (mm), is adjacent to the nozzle wall. Four cases have been calculated with a minimum cell thickness of 0.06, 0.08, 0.10 and 0.15 mm, respectively.

In Figure 4.9(a), the total particle deposition mass as a function of time is evaluated. With the special setting of this benchmark, i.e. imposed constant mass flow rate of the melt, two typical changes of the curvature of the curves are evident: the first change is at ~2 s and the second one is at around 42–46 s. The first change corresponds to the early stage of clogging, while the second corresponds to the morphological transition of the clog front from the bulged front to the branched structure (Figure 4.9(b)). During the early stage of clogging, the case with the largest mesh size, 0.15 mm, appears to calculate more deposition mass, while results of other cases, mesh sizes ≤0.1 mm, are similar, i.e. their curves are close to each other until 24 s. The growth of the clog front (Figure 4.9(b)) in the case with the

coarsest mesh is also significantly divergent from other cases. Therefore, based on similar results of cases with mesh size ≤0.08 mm, it is suggested that the case with smallest mesh size of 0.08 mm adjacent to the nozzle wall is sufficient to solve the clogging problem during the early stage; this mesh size is also selected for other simulations. There is a substantial difference between the four degrees of mesh fineness observed during the late stage of clogging (after the bulge-branch transition). It should be mentioned that a relatively coarse mesh size (~3 times larger than the smallest mesh size adjacent to the nozzle wall) is used in the interior of the nozzle. These coarse mesh sizes might not be sufficient to solve the late stage of clog growth precisely.

(a)

(b)
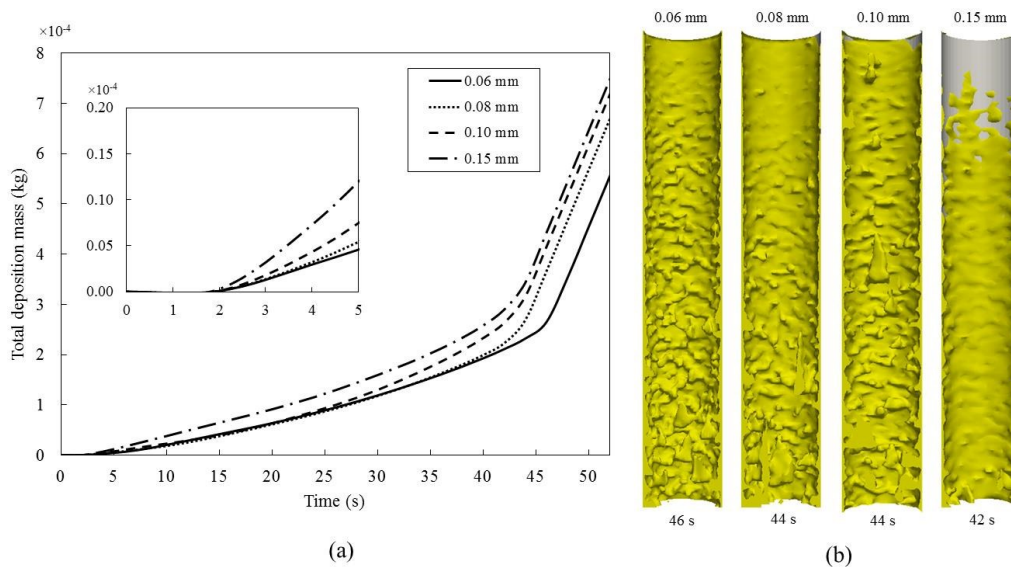
Figure 4.9 Sensitivity of the calculated total particle deposition mass in relation to the mesh size. Four calculations with a different mesh fineness, respectively, are calculated and compared. Values in the legend stand for minimum cell thickness adjacent to the nozzle wall. (a) Total particle deposition mass as a function of time; (b) Clog front profile as predicted at the moment of branching.

4.4.3 Lagrangian time scale

The Lagrangian time scale (T_L) is a numerical parameter which is used in the stochastic model of particle tracking in the turbulent boundary layer. Results of the total deposition

mass of particles for different values of T_L (2–10 µs) are evaluated in Figure 4.10. Since T_L is applied only for the early stage of clogging, the curves are plotted until 6 s. It shows that three values of T_L lead to similar deposition mass. The value of 2 µs T_L leads to a slightly smaller amount of deposition, meaning there is a prediction of the smaller deposition mass. To confirm this finding, a further study of the effect of T_L on the particle deposition is to be performed. In a wall-bounded cell at 0.03 m from the outlet, 1000 particles are injected at identical time and position. The fates of these particles are tracked by using different T_L (2, 6, 10 µs). The model is inherently stochastic and results of one simulation trial are different from those of others even same settings are made. Therefore, for each T_L the simulation is repeated 10 times and then average values are compared. According to the new results, as shown in Figure 4.11, the number fraction of particles (in percentage) as adhered to the wall for the cases with $T_L = 6$ and 10 µs are almost the same, whereas, for the case with $T_L = 2$ µs, it is ~0.5% smaller. Again, it transpired that the case with $T_L = 2$ µs predicts the smaller deposition mass. The standard deviation for the 10 times of repeated calculations, identified by error bars, is also shown in Figure 4.11. The standard deviation seems to increase with T_L. Therefore, T_L should not be too large. If the value of T_L is excessive, this is not desirable, because it may cause a particle to cross the computational cell in one step. If T_L is too small, particles would hardly come into contact with the wall, due to the state of particle motion (sweep, diffusion, or ejection) changes too frequently. As shown in Figure 4.10, the case with $T_L = 2$ µs has a lower deposition rate than the case with $T_L = 6$ and 10 µs. To the author's knowledge, there is no reliable criterion to identify T_L under different conditions.
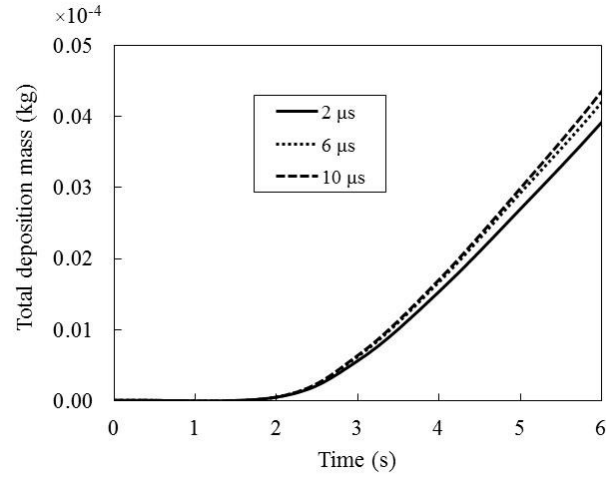
Figure 4.10 Influence of the Lagrangian time scale T_L on the total particle deposition mass.
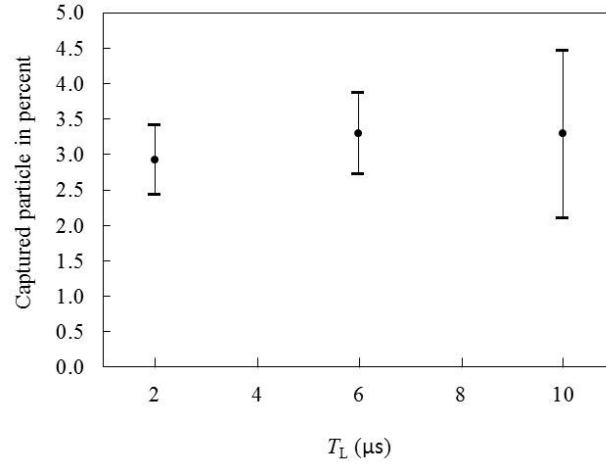
Figure 4.11 Influence of the Lagrangian time scale T_L on the number fraction of particles that adhere to the wall. Error bars represent standard deviation.

4.4.4 Correction power for permeability of clog

In the current model, according to the postmortem analysis of the clog structure [80], clog is assumed to be a uniform, isotropic, porous medium. In a partially clogged cell, the average permeability is calculated as:

$$K_{\text{per}} = \frac{\left(1-\bar{f}_p\right)\left(1-\bar{f}_p^{1/3}\right)}{108\left(\bar{f}_p^{1/3}-\bar{f}_p\right)} D_{\text{pore}}^2 \frac{1}{f_{\text{clog}}^n}, \tag{4.1}$$

where n is the correction power. For a fully-clogged cell, n plays no role. In Figure 4.12(a), $1/K_{per}$ as a function of f_{clog} is plotted for different n's. $1/K_{per}$ is used to calculate a Darcy source term in momentum, k, and ω equations. A value of 1 for n means a linear interpolation of $1/K_{per}$ between $f_{clog} = 0$ and $f_{clog} = 1$. In this case, a very small change of f_{clog} initially would lead to an immediate increase of $1/K_{per}$. In other words, with a small amount of particle deposition in a new computation cell, the permeability of this cell decreases rapidly. This, however, does not make sense physically. Thus, a larger value for n should be selected. In Figure 4.12(b), total deposition mass vs. time is shown for different values of n (1, 2, 5, 10). Logically, until 35 s, there is no difference to be identified between the different cases, as the formulations for permeability (equation (4.1)) influence only the inner region of the clog. Substantial deference is evident during the late stage of clogging after the bulge-branch transition and a greater value of n results in earlier branching.
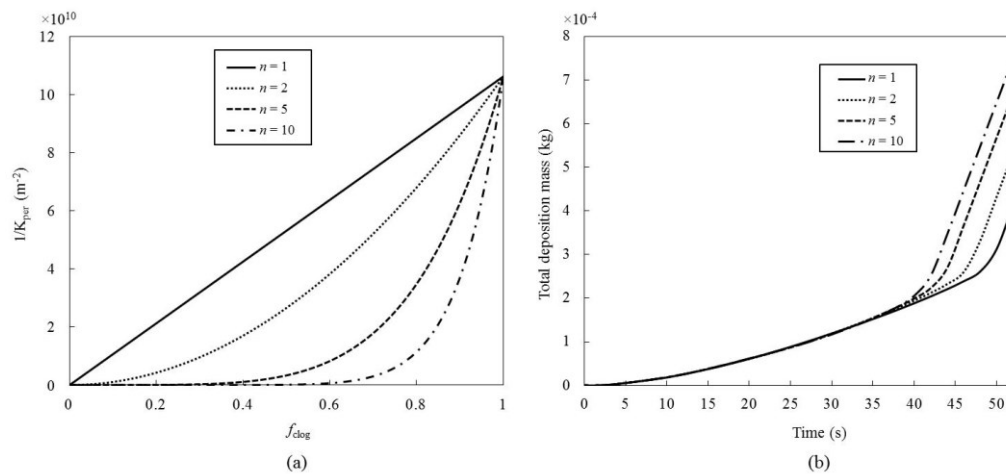
Figure 4.12 Influence of the correction power in the permeability formulation on the total deposition mass. (a) $1/K_{per}$ as a function of f_{clog}; (b) total deposition mass as a function of time.

According to Figure 4.12(b), when a larger value is applied for the correction power (n) in the interpolation of clog permeability, the bulge-branch transition of the clog occurs sooner.

The larger the n value, the more permeable the partially clogged cells become. When a particle enters one of these cells, it can leave this cell into its neighboring partially clogged cells with greater ease; the bulge-branch transition occurs sooner. An excessive n value leads to an unphysical overestimation of permeability. Additionally, if n is too large, this introduces a convergence problem, because it makes the curve of $1/K_{per}$ (Figure 4.12 (a)), or Darcy source term, as a stepwise function. With $n = 1$, i.e. linear interpolation, the permeability of a cell decreases too much, resulting in a tiny amount of particle deposition, which is not reasonable.

4.4.5 **Porosity of clog**

The porosity of clog material is described by the process parameters, d_p, $\bar{f}_p$ and D_{pore}. They must be determined experimentally. Since $\bar{f}_p$ and D_{pore} are related to each other and one of them cannot change independently, as listed in Table 4.2, three sets of $\bar{f}_p$ and D_{pore} are suggested (Case 1-3). The porosity parameters of Case 2 are used for previous verification studies (§4.4.2 - §4.4.4). For Case 4, the assumption of being an open pore structure is not valid. Therefore, in Case 4 the porous medium is assumed to be formed with randomly packed spheres, for which the Kozeny-Carman permeability law is applicable. For all cases, $d_p = 5$ μm. Particle deposition mass is presented in Figure 4.13(a). Clog front morphology at the moment of bulge-branch transition is shown in Figure 4.13(b). Observations show that while for Case 1-3 bulge-branch transition happens at 36, 44, and 46 s, respectively, Case 4 shows no sign of this transition until 60 s. The deposition rate prior to the bulge-branch transition, i.e. slope of the curve of deposition mass, increases with $\bar{f}_p$.

Table 4.2 Properties of porosity in different cases

	$\bar{f}_p$	D_{pore} (µm)
Case 1	0.400	60
Case 2	0.500	50
Case 3	0.550	45
Case 4*	0.634	-
*For this case Kozeny-Carman permeability is used.		
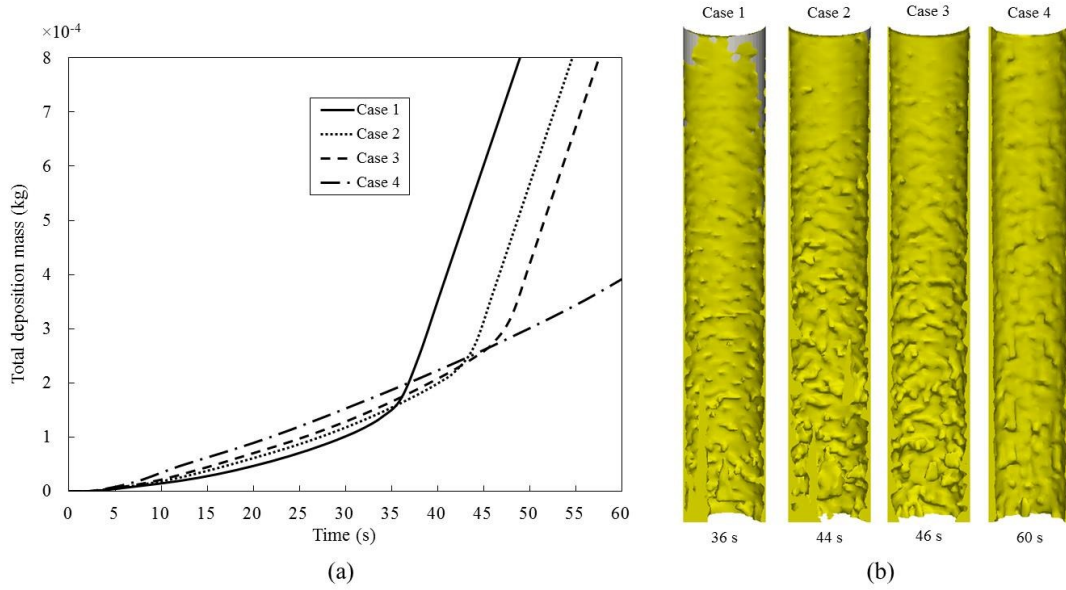
Figure 4.13 Influence of porosity parameters of the clog on the total particle deposition mass and the clog front morphology. (a) Total particle deposition mass as a function of time and (b) clog front morphology for four different cases as defined in Table 4.2.

5. Application in industry process

In the previous chapter, the model has been validated against experimental data in a laboratory scale and numerical uncertainties have been studied. In this chapter, extension of the model to industry scale is presented. At first, model accuracy and calculation efficiency challenges are investigated (§5.1); then, simulation in industry scale is performed (§5.2).

5.1 Calculation accuracy and efficiency

To model the clogging in the SEN of industry scale, one numerical issue is the mesh type (tetrahedron, hexahedron). Due to the complex geometry of SEN, it is much more convenient to create tetrahedron mesh in the nozzle region. However, the numerical tracking of the clog front based on the tetrahedron mesh is to be evaluated. The use of tetrahedron mesh is known to influence the accuracy of flow calculation in some cases, but it is not clear how this imperfection influences the clogging simulation.

Another challenge to a numerical model for such engineering application is the huge number of NMI particles. The real number of particles is estimated in the order of 10^{11} particles (with average size of 5 μm) per ton of molten steel. During the practice of continuous casting, the clogging event would occur after 10^2 tons of casting for the worst case. If all particles were accounted individually, a total number of 10^{13} particles would be involved. It is out of the capacity of the current computer hardware if a Lagrangian

approach is used. To overcome this problem, an artificial factor, named as 'N-factor', is necessarily introduced to the numerical model. This N-factor is equal to the "number of representative particles". The motion of individual particle is tracked in the molten steel by accounting its interactions with the turbulent flow, but this particle will represent N particles as it deposits on (or is captured by) the clog front or SEN wall. It means that with this numerical trick the calculation efficiency will be enhanced (or the calculation time will be reduced) by the N-factor. However, the influence of introducing this N-factor on the calculation accuracy is not clear, to be studied here.

5.1.1 Mesh type effects

5.1.1.1 Test cases

It is well-known that the CFD (Computational Fluid Dynamics) calculation of flow field depends on the mesh quality. In order to validate the algorithm for clog growth (§3.4), two case studies are separately performed: (1) an ideal case of 'pure' clog growth due to the particle deposition without the effect of fluid flow, and (2) a reality-close case of clog growth combining the particle deposition and the effect of fluid flow.

Although the case (1) is not realistic, it helps to study exactly the effect of the mesh type on the modeling accuracy for the clog growth. As depicted in Figure 5.1(a), a simple cubic calculation domain is designed, where no flow is involved. Alumina particles are injected with a uniform distribution from the inlet (top) vertically downwards, and they move with equal speed towards the wall (bottom). Particles stop once they meet the wall or clog front. The diameter of particle is 10 μm, and 45 million particles are injected in total.

For the case (2), which includes the effect of fluid flow, the computational domain is depicted in Figure 5.1(b). Two parallel walls with 5 mm distance are designed. A fully developed flow with mean velocity of 5 m/s is assigned to inlet at the top boundary and pressure-outlet is imposed for outlet at the bottom boundary. The values for average fluid

velocity and distance between two walls are extracted from typical results of flow of molten steel through the gap between stopper and SEN during continuous casting of steel. The front and back boundaries are symmetrical planes. On the walls, no-slip conditions with an initial roughness height (10 μm) are applied. To have better visualization of the clog growth, a certain area of the walls is defined for the particle deposition, as highlighted (dark gray) in Figure 5.1(b). In the other area of the wall (light gray), rebound boundary condition is imposed for particles. Alumina particles with a diameter of 10 μm are injected at inlet with a constant mass injection rate. Since two walls are exposed to same conditions, only one wall is considered and the calculation domain is from left wall to a parallel plane exactly located in the middle of two walls, i.e. a half of the geometry as shown in Figure 5.1(b) is simulated.

As shown in Figure 5.1(c), three types of mesh are studied for both cases (1) and (2). Hexahedron and tetrahedron are mostly used in CFD calculation. Sometimes a combination of wedge mesh near the wall and tetrahedron in the inner region is used as well.
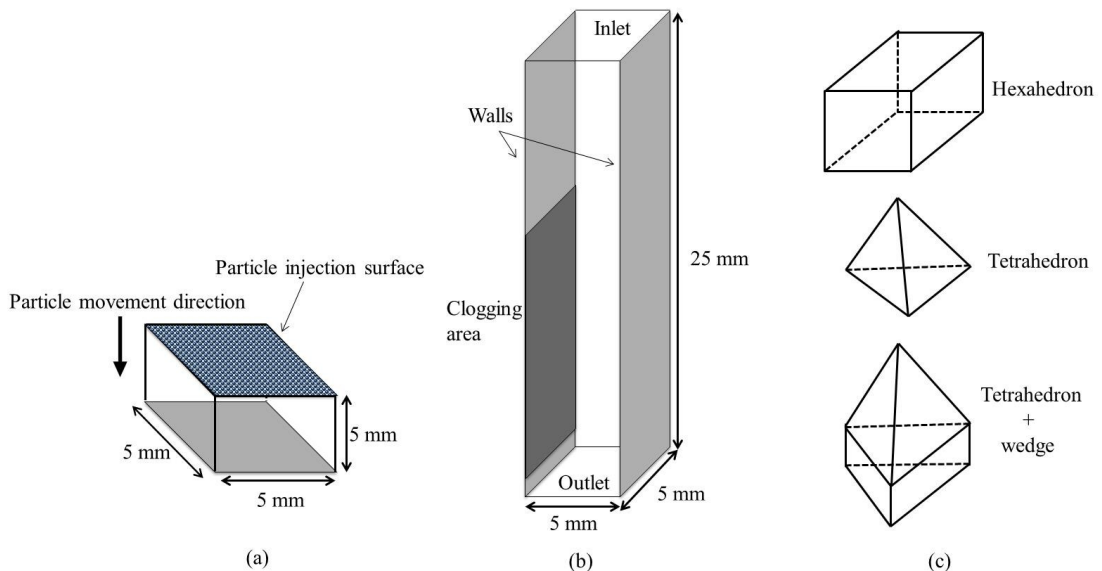
Figure 5.1 Computational domain and boundary conditions to study mesh dependency of the clog growth algorithm without (a) and with (b) the effect of the fluid flow, and different mesh types used in the current study (c).

5.1.1.2 **Transient clog growth**

Modeling results of the transient clog growth (Case 2, with flow) are shown in Figure 5.2. The partially-clogged cells, with light gray, surround the fully-clogged cell, shown by dark gray. The fully-clogged cells can be seen on the left section. The wall roughness height enhanced by particle deposition at the initial stage is shown by contours (color scale) on the wall. At 10 s, a band of fully- and partially-clogged cells form on the top of the clogging area. In the rest part of the wall (clogging area), particles are mostly deposited to enhance the wall roughness (at the initial stage of clogging). The enhanced wall roughness (diameter of the equivalent sand-grain), shown by color scale, is still smaller than half of the cell size, hence no partially-clogged or fully-clogged cell is observed.

The clog tends to grow against the flow direction, as seen from the results at 20, 30, 40, 50 s. Other fully- and partially-clogged cells are distributed erratically (randomly) on the clogging area, preferably near the symmetry planes. A zoomed view of the flow streamlines with partially- and fully-clogged cells is shown for the result at 50 s (Figure 5.2). This view indicates how clog growth results in change in the flow pattern and consequently changes in the deposition of the particles.
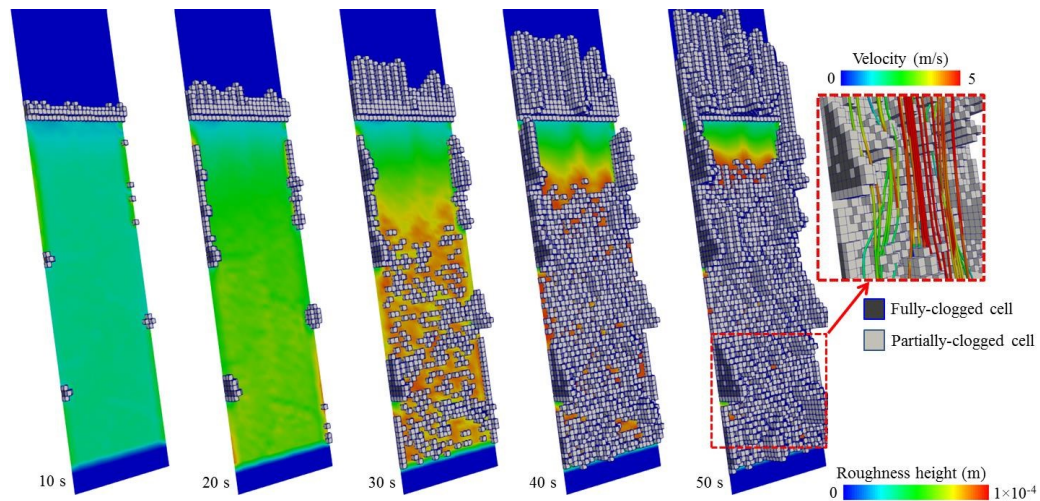
Figure 5.2 Modeling result of the transient clog growth for the case 2. The fully-clogged cells (dark) and partially-clogged cells (light) are shown. Roughness height of the wall (diameter of the equivalent sand-grain) enhanced by the particle deposition is shown by color scale. A zoomed view with flow streamlines is shown for the moment at 50 s. Mesh type is hexahedron.

5.1.1.3 **Clog growth without flow (Case 1)**

The pure clog growth under the simplified circumstance without flow is calculated, and the calculation domain is described in Figure 5.1(a). The calculation results of the clog front, using different mesh types, are shown in Figure 5.3. The partially-clogged cells (yellow) define the clog front; for clearness the fully-clogged cells (below the clog front) are not shown. The result with hexahedron mesh represents the precise result. The clog front is (should be) smooth and flat, as the particles are uniformly injected from the inlet (top), and homogenously deposited on the wall/clog front. The calculation with the tetrahedron mesh shows, however, that the clog front is not flat, and some partially-clogged cells are even embedded in the fully-clogged region (this should not occur in this case). Because the size and orientation of each cell in tetrahedron mesh is different, some cells, in preferable orientation, would be more easily occupied by the clog than other cells. If the cells in the upstream direction are occupied sooner than the downstream cells, these downstream cells would remain partially-clogged (never become fully-clogged). In the case with wedge mesh

near the wall and tetrahedron mesh in the bulk, some cells are also left below the clog front as partially-clogged cells. However, in the wedge region, no partially-clogged cell is seen, except for few cells which are located adjacent to wedge-tetrahedron border. At the border, some tetrahedron neighbor cells, in preferable orientation, are occupied sooner than some wedge cells below. The tetrahedron mesh region (above the wedge region) behaves similarly as the last case, and some partially-clogged cells remain below the clog front. As a conclusion to this study, both hexahedron mesh and wedge mesh are suitable for tracking the clog front. The current algorithm for tracking the clog front does not apply for tetrahedron mesh.
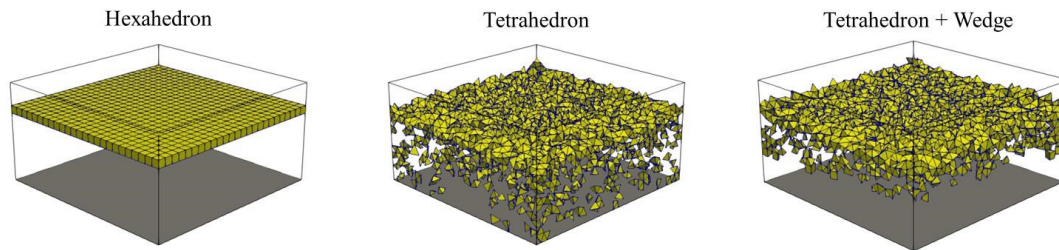
Figure 5.3 Effect of mesh type on the tracking of clog front. Only partially-clogged cells are shown (yellow). This result is shown when all injected particles (45 million) are deposited.

5.1.1.4 Clog growth with flow (Case 2)

For this study, the calculation domain is shown in Figure 5.1(b). Typical clog growth was described in §5.1.1.2 (Figure 5.2). The total particle deposition mass (kg), i.e. the integral of the mass of clog materials over the whole wall, is plotted as a function of time (Figure 5.4(a)). The mass deposition rate (kg/s), i.e. the time derivative of the total particle deposition mass, is plotted in Figure 5.4(b). The results as calculated with different mesh types are compared. Since clogging is a self-accelerating phenomenon, and imposed constant mass flow rate is applied at the inlet, the deposition mass rates increase with the time for all mesh types. The results indicate that until 10 s deposition mass and its rate for hexahedron mesh and tetrahedron with wedge are very close. After 10 s, the deposition rate

for tetrahedron with wedge increases with larger slope than that for hexahedron. The deposition rate for tetrahedron mesh at the early stage of clogging is small, but after around 5 s it increases suddenly with a larger slope than that for two other mesh types. This behavior results in a big difference in the total deposition mass between different mesh types. At 30 s, deposition mass rate for the tetrahedron mesh is about 2 times larger than that for the hexahedron mesh, and it is significantly overestimated.
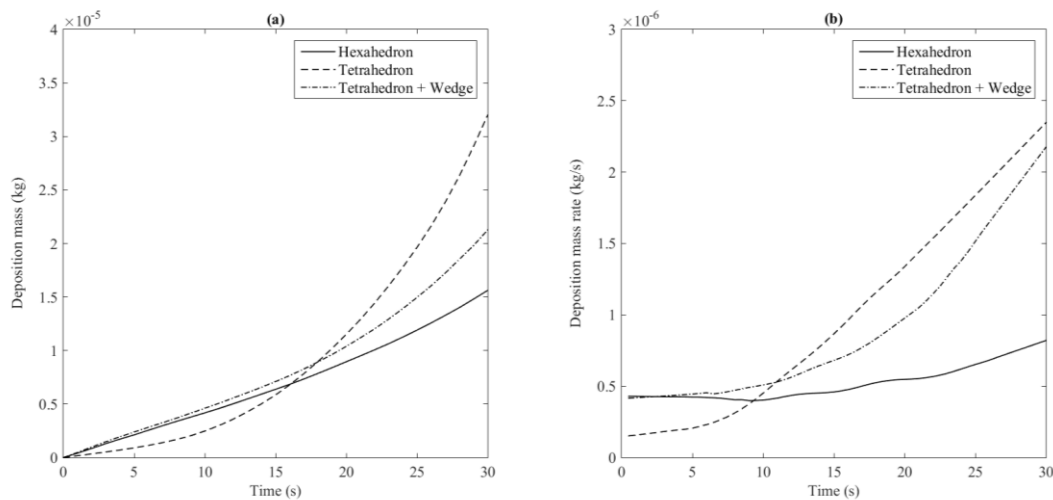
Figure 5.4 Total particle deposition mass (a) and its rate (b) as a function of time for different mesh types.

The results of Figure 5.3 indicate that tetrahedron mesh does not work properly with the clog growth algorithm. As shown schematically in Figure 5.5, when an unstructured tetrahedron mesh is used, some cells may be filled sooner than the other neighbor cells. For example, cell 'A' is fully-filled before cell 'B'. Then, cell 'A' is converted to fully-clogged and its neighbor cells should be exposed to the particle deposition as partially-clogged cells ('C' and 'D'). The new partially-clogged cell 'C' may be fully filled sooner than cell 'B' which is located in the downstream direction. Therefore, the old partially-clogged cell 'B' might be isolated and stays as a partially-clogged cell forever. Owing to the fact that the clog is a network of the deposited particles, it is assumed that the clog acts as a filter. So, particles cannot go through the clog and are captured by partially-clogged cells.
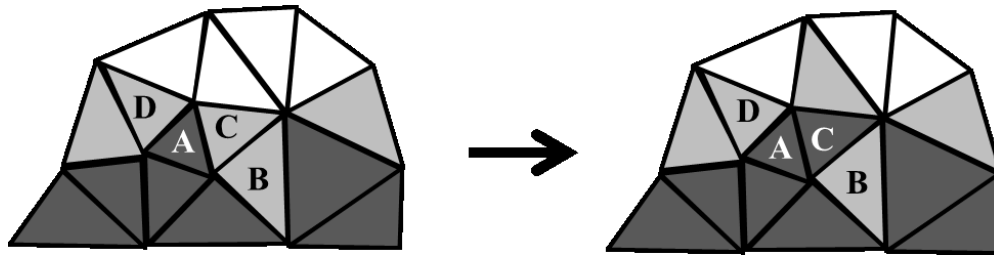
Figure 5.5 Schematic illustration of how a partially-clogged cell may be surrounded by fully-clogged cells in an unstructured tetrahedron mesh. Fully-clogged and partially-clogged cells are shown with dark and light gray, respectively.

For the current version of the clogging model, tetrahedron mesh would lead to an unreliable result. With the improvement of the measurement of the particle distance from the clog in partially-clogged cells, this issue would be solved. In cases with complex geometry, like submerged entry nozzle, where the creation of a mapped hexahedron mesh is too difficult, a combined mesh of tetrahedron cells in the bulk and wedge cells close to the walls can be used. According to the results of Figure 5.3 and Figure 5.4, the clog growth model works well with this kind of mesh under both conditions without and with the flow, respectively. Note that the clog growth should be tracked only in the wedge cells region. From CFD point of view, to have a more accurate fluid flow the wedge mesh near the wall is also recommended instead of tetrahedron mesh.

5.1.2 Number of representative particles (N-factor)

5.1.2.1 Test case

This study is performed with the benchmark configuration of Figure 5.1(b), i.e. the flow effect is included for consideration. To study the sensitivity of the model to N-factor, 29 simulations were made, as listed in Table 5.1, by varying the N-factor, particle diameter (d_p) and number injection rate. The total mass injection rate of particles from the inlet in each simulation case is kept constant, 1.33×10^{-5} kg/s. For example, for the simulation case (N-factor = 1; d_p = 2.0 µm), the particle number injection rate at the inlet must be 860 million

per second; for another case (N-factor = 1257; d_p = 2.0 μm), the particle number injection rate at the inlet must be 0.684 million per second. It should be mentioned that under the condition of constant mass injection rate at the inlet, N-factor cannot be always an integer number; however, here, the rounded value of N-factor is reported which looks integer. With the increase of N-factor, the total number of particles for the simulation decreases by a factor of N; to treat the flow-particle (hydrodynamic) interactions, each particle represents only one particle; as soon as the particle deposits on (or be captured by) the clog front, one particle represents N particles.

Table 5.1 Numerical studies of the effects of N-factor on the clogging (The total mass injection rate of particles at the inlet is constant: 1.33×10^{-5} kg/s).

d_p (μm)	N-factor	Particle number injection rate (million particles per second)
2	1, 10, 25, 78, 157, 314, 628, 1257	860, 85.5, 34.2, 10.944, 5.472, 2.736, 1.368, 0.684
4	1, 6, 10, 31, 78, 157	102.6, 17.1, 10.26, 3.42, 1.368, 0.684
6	1, 3, 6, 9, 23, 47	30.78, 10.26, 5.472, 3.42, 1.368, 0.684
8	1, 3, 5, 10, 20	12.996, 4.788, 2.736, 1.368, 0.684
10	1, 3, 5, 10	6.84, 2.052, 1.368, 0.684

The evolutions of the mass deposition (kg/m^2) on the wall for selected simulation cases (N-factor = 10, 25, 157, 628; d_p = 2 μm) are presented in Figure 5.6. The mass deposition at the initial stage (resulting in enhancement of the wall roughness) is also included. In principle, all 4 cases are similar. Before 20 s, almost no difference can be seen for all 4 cases; a horizontal clogging band is seen on the top edge of the clogging area and several spots are shown near the symmetry planes, corresponding to the result of Figure 5.2. After 30 s, for two first cases (N-factor = 10, 25), the results are almost identical; two other cases (N-factor = 157, 628) show slightly more difference, but the difference is not evident.
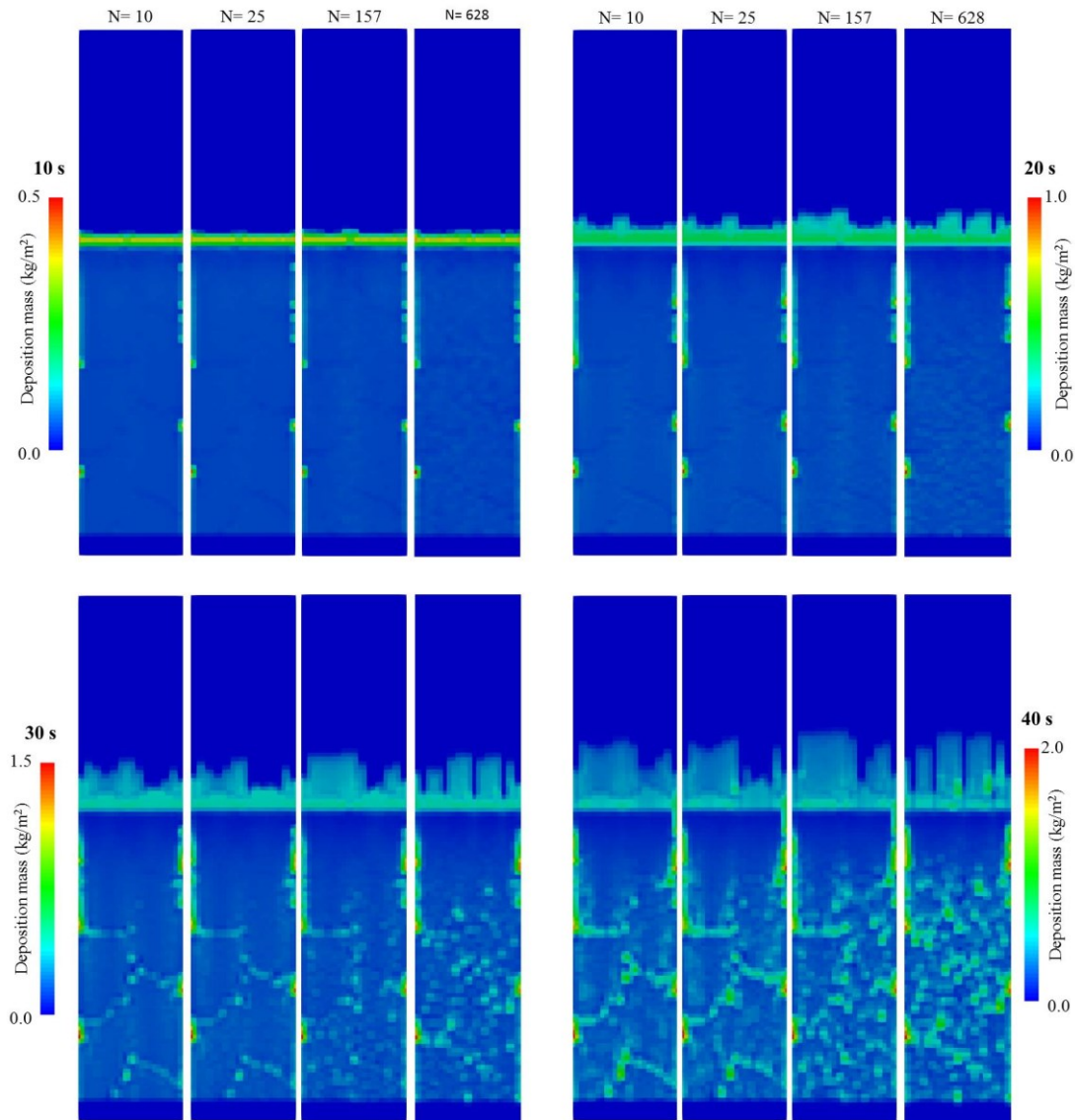
Figure 5.6 Evolutions of the mass deposition (kg/m^2) on the wall for selected simulation cases with N-factor (10, 25, 157, 628; $d_p = 2$ μm). Results of 4 different moments (time = 10, 20, 30, 40 s) are shown. The deposition mass [kg/m^2] in color scale represents the total mass of deposited particles, which is projected onto the wall (facilitating a 2D presentation).

In Figure 5.7, the particle deposition mass (kg), i.e. the integral of the mass of clog materials over the whole wall, and the mass deposition rate (kg/s), i.e. the time derivative of the total particle deposition mass, are analyzed. The effect of N-factor on the clogging can be more quantitatively identified. Obviously, all curves with different N-factors are almost identical before 20 seconds. After 20 seconds, generally, the higher value of N-factor leads

to a higher deposition mass. However, the curves for N<100 are almost overlaid with each other.
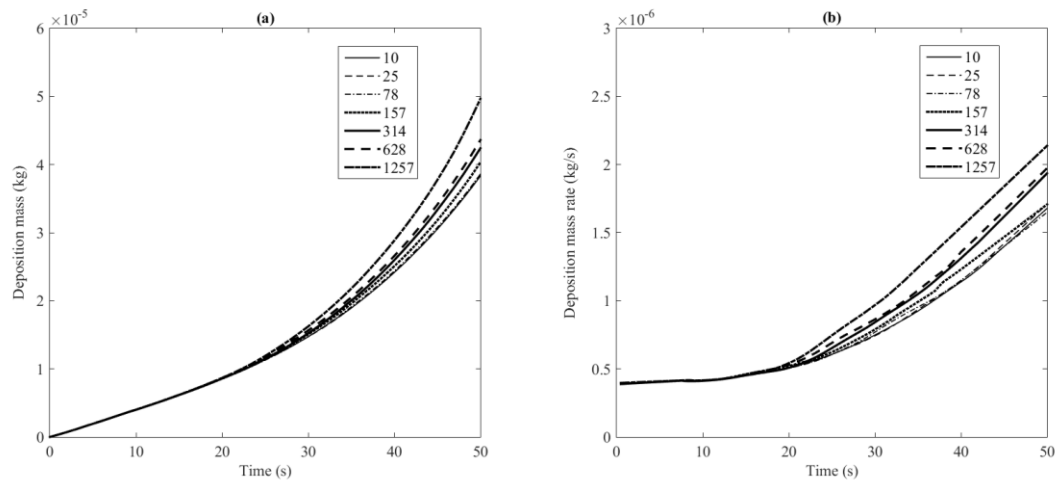
Figure 5.7 Total particle deposition mass (a) and its rate (b), and their dependence on the N-factors. $d_\mathrm{p} = 2$ µm.

As explained before, the numerical model (algorithm) treats the clogging process in two stages: the initial stage of particle deposition on the wall which enhances the wall roughness; and the second stage of clog growth (to consider the clog growth as a porous medium). A hypothesis to explain the effect of N-factor on the clogging, as shown in Figure 5.7, is due to the transition to the second clog growth stages. The algorithm for the initial stage with the enhanced wall roughness ignores the potential build-up of the network of a porous medium. Note that the initial roughness of the SEN wall is set ~10 µm, which is close to the size of the NMIs. It implies that deposition of few layers of particles with size of 2 - 10 µm can enhance the wall roughness in the order of the initial wall roughness.

To further verify the above hypothesis, the mass deposition is separated due to the initial clog growth (enhanced wall roughness) from the total mass deposition by defining a so-called 'contribution of mass deposition by wall roughness enhancement' (mass%). Results of calculations with different N-factors are shown in Figure 5.8. The curves start from 100%, i.e. all mass deposition is initially due to the algorithm by the wall roughness

enhancement. With the time, the contribution due to this algorithm reduces gradually. To the moment of 20 s, about 60% of the deposition mass is to be consumed to enhance the wall roughness; correspondingly, the rest of 40% of the mass is for the growth of clog as a porous medium. After 30 s, the second stage of clog growth (porous medium) becomes dominant. The period between 20 and 30 s would be a transition period. The all curves for different N-factors show very similar trends, but in the transition period (from 20 to 30 s) some differences are observed. A larger N-factor leads to a smaller mass contribution of the initial clog growth stage. In addition, the slope of the curves increases with the increase of N-factor in the transition period.
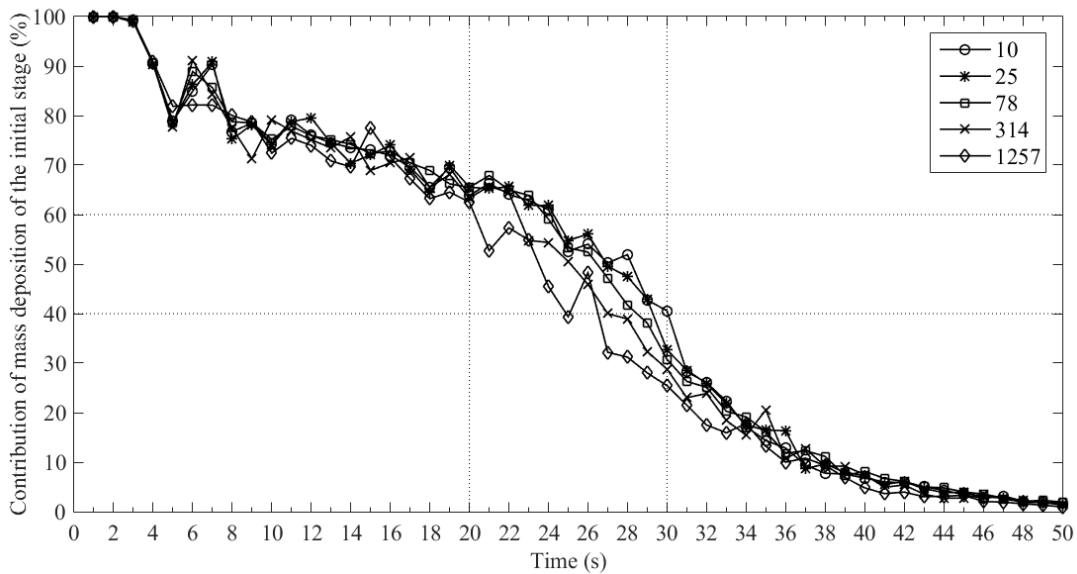
Figure 5.8 Contribution of mass deposition by means of wall roughness enhancement in every 1 second. It is calculated as a fraction of mass deposition due to the initial clog growth (enhancing the wall roughness) respecting to the total mass deposition [mass %]. $d_\mathrm{p} = 2\ \mu m$.

The aim of introducing N-factor is to reduce calculation time with sacrifice of calculation accuracy. Here a deviation parameter, Δ, is introduced to quantify the calculation accuracy.

$$\Delta = \frac{M_N - M_1}{M_1} \times 100,$$ (5.1)

where M_N stands for the total deposition mass when N-factor = N and M_1 is the total deposition mass when N-factor = 1 (the reference case: the calculation is most accurate). The variations of Δ with N-factor for cases with different particle size are shown in Figure 5.9(a). For the smallest particle size (2 μm) Δ is negligible when N<100. However, for the largest particle size (10 μm) when N<10, Δ is larger than 30%. It means that dependency of the total mass deposition on the N-factor increases with an increase in particle size. It indicates that the particle size should be taken into account as a factor influencing the Δ-N dependency. Hence a dimensionless number, α, is further defined.

$$\alpha = \frac{N \times V_p}{V_{cell}}, \tag{5.2}$$

where V_p and V_{cell} are the volume of particle and volume of the computational cell, respectively. This parameter, α, can also be understood as scaled (or dimensionless) N-factor. Coincidently, a linear correlation is obtained between Δ and α, as shown in Figure 5.9(b). It indicates that numerical calculation accuracy increases with the decrease of α. According to Figure 5.9(b), if 10% of Δ is accepted as a criterion for most engineering calculation, α should be smaller than 0.0002. In the other words, to have modeling result independent on N-factor, α should be chosen to be smaller than 0.0002.

The results of Figure 5.6 and Figure 5.7 indicate that the deposition mass until 20 s is almost identical in both distribution of the clog and total deposition mass for all values of N-factor. In addition, the results of Figure 5.7 and Figure 5.8 show that after 20 s, when the second stage of the clog growth is dominant, the influence of N-factor on the deposition mass is observable. This issue happens for larger N-factor earlier than for the smaller ones, which is understandable from the transition period shown in Figure 5.8. Therefore, the sensitivity of the clog growth to N-factor comes from the particle motion and deposition in the partially-clogged cells, i.e. the second stage of the clog growth.
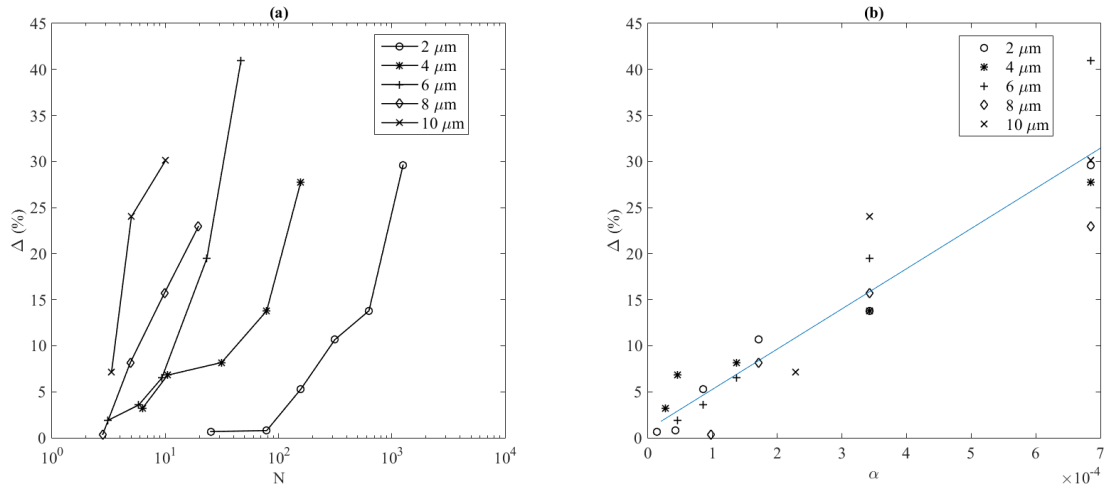
Figure 5.9 Numerical study of the calculation accuracy and its dependency on N-factor. (a) The deviation factor Δ as a function of N-factor; (b) the deviation factor Δ as a function of α. The clogging result is evaluated for different particle sizes at the moment of 50 s.

Assume that a certain mass of particles with the same size enters a partially-clogged cell. If a larger N-factor is chosen, fewer particles enter the partially-clogged cell. In the severest situation, i.e. the largest N-factor, only one particle would be in the partially-clogged cell. If this particle reaches the clog front, the whole mass, which is equal to the mass of a single particle multiplied by N, will be added to the clog. While, with smaller N-factor several particles enter the cell. Some of them may reach the clog and the others may escape to the neighbor cells. That is, if N-factor is small, for a certain mass of the particles, there is more freedom for particles to escape from a partially-clogged cell to the other neighbor cells. Therefore, the deposition mass in the partially-clogged cell does not increase excessively at once. Hence, the smaller N-factor results in less deviation in particle deposition than the larger N-factor, as shown in Figure 5.7.

By changing the particle size, the effects of N-factor on the particle deposition change, as can be concluded from Figure 5.9. Therefore, a dimensionless number α is defined for a reasonable N-factor according to Figure 5.9(b). Although Figure 5.9(b) may not be valid for every simulation conditions, α can be used to study the dependency of the deposition mass

on this number. For example, for a process of industry scale, where simulation with the real number of particles is not feasible and a relatively large N-factor should be selected, it is better to examine the particle deposition mass dependency on α, as what is always done for the mesh dependency during CFD calculations.

5.2 Simulation of clogging for industry scale SEN

Clogging generally comprises successive steps: (1) transport of particles to the wall; (2) deposition of particles on the wall; (3) growth of the clog; and (4) possible fragmentation (detachment) of particles. Most numerical models of SEN clogging consider two initial steps of clogging, i.e. transport of particles by fluid flow towards the wall and deposition on the wall [7,75,112]. In these models, the deposited particle is removed from the calculation and the effects of the deposited particle on the fluid flow are ignored. The effects of the clog on the melt flow are also investigated by initial changing the geometry manually [26,28]; however, the dynamic behavior of the build-up of the clog and its interaction with the flow are ignored. The current model can really cover transient two-way coupling between fluid flow and particle deposition, including steps (1) - (3). Here, the model is applied to industry scale SEN. Effects of process parameters, like SEN diameter and tundish level, are also investigated.

5.2.1 Simulation settings

The simulation of clogging considering the whole tundish and SEN is not possible because of huge calculation costs. The domain is big and a large number of computational cells should be created (cell size must be controlled); the process time is in the order of hour; number of particles in the domain is huge. On the other hand, tracking of particles in the tundish is not necessary for the clogging simulation. Due to the very small size of the

particles ($< 10\ \mu m$), they follow the melt flow to the SEN; floatation of particles of such size occurs rarely. Tracking of particles with Lagrangian approach (even considering N-factor) in the whole tundish for duration of 30 min is out of current computers' capability. Therefore, only the upper part of SEN, near the stopper rod, is considered for the current clogging simulation (Figure 5.10(b)). The geometry of the SEN and the stopper is defined, but vertical position of the stopper, i.e. gap size between the stopper and the SEN, for a certain casting speed is unknown. In order to find the correct gap size for a certain melt flow rate, related to the casting speed, the process simulation is done in two steps. In step 1, the whole tundish with the upper part of the SEN is simulated (Figure 5.10(a)). The purpose is to find the position of the stopper rod, and proper flow boundary conditions for the clogging simulation, i.e. step 2, in a reduced calculation domain, shown in Figure 5.10(b). In step 1, the stopper rod position is varied until the aimed mass flow rate of steel melt is reached. A two-phase flow of steel melt and air using VOF approach is considered. With the achieved information of the stopper rod position, the geometry for the near stopper region is designed for clogging simulation (step 2). Tundish level ($h_{tundish}$) and SEN diameter (d_{SEN}) are variable. In the reference simulation, $h_{tundish} = 0.8\ m$ and $d_{SEN} = 75\ mm$.

The real number of solid particles entering into SEN is estimated. If the oxygen content of the steel melt in the tundish is around 30 ppm [148] and if all of the oxygen is assumed to react with dissolved aluminum in the steel melt to produce Al_2O_3 (the common NMI in SEN), the concentration of Al_2O_3 in the steel melt would be 1.24×10^{-4} vol%. For the domain shown in Figure 5.10(b) with total volume of $0.018\ m^3$, ~20 billion particles with $d_p = 6\ \mu m$ should be calculated in this domain. Simulation of such large number of particles is not feasible. Therefore, use of the number of representative particles (N-factor) is inevitable for the simulation of SEN clogging.
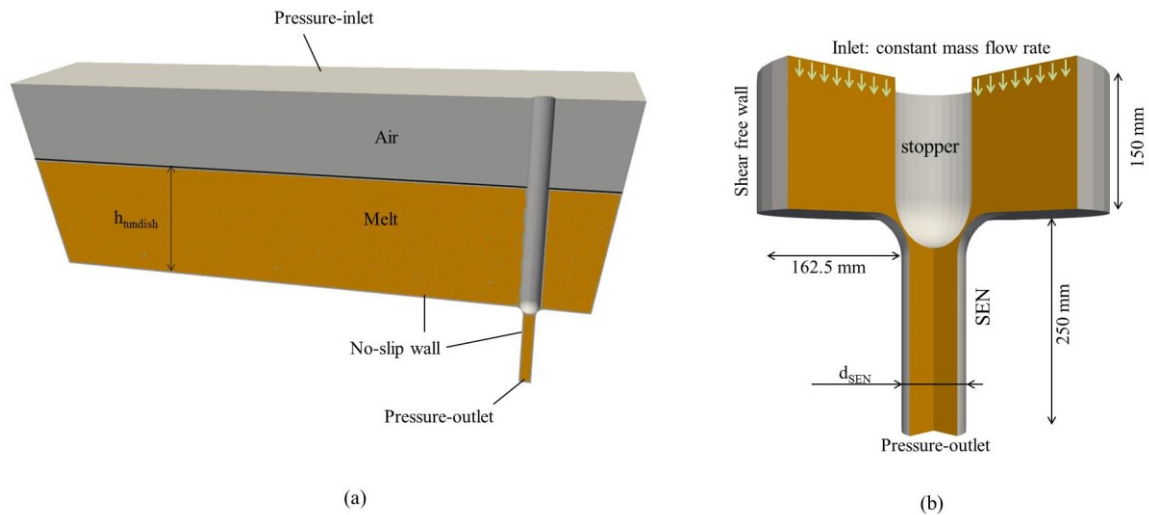
Figure 5.10 Geometry and boundary conditions for process simulation of clogging: (a) step 1, global flow calculation and (b) step 2, clogging simulation.

In the simulation of clogging, 30 min of the process is simulated. The target melt flow rate is 58.25 kg/s. Alumina particles with diameter of 6 μm are injected with mass-injection-rate of 4.3×10^{-9} kg/s. Here, N-factor is set to 1000, corresponding to $\alpha = 6 \times 10^{-5}$. The calculation time on a high performance computer with 12 CPUs (2.9 GHz) is around 75 hours. Hence, by introducing N-factor, simulation for an industry process can be feasible.

5.2.2 Simulation results

In Figure 5.11, the clog front in SEN is shown along with a zoomed view of the thickness of the clog formed on the nozzle wall after 30 min. The critical regions to start clogging are found, i.e. the upper region of the nozzle in the stopper gap. It should be noticed that clogging is a transient phenomenon and the critical position of clogging might change during the casting process due to the change in fluid flow by clogging.
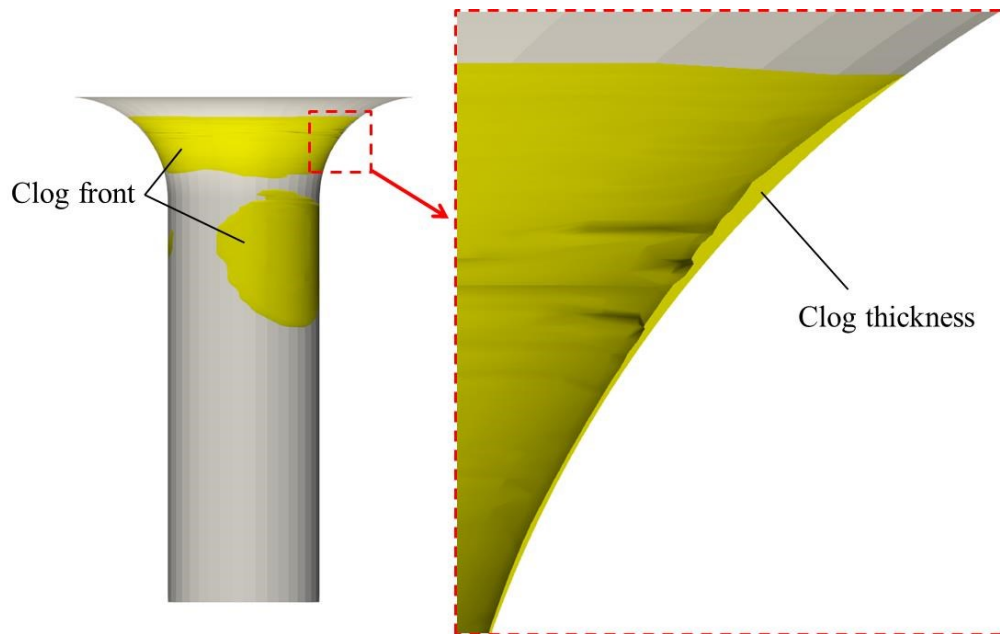
Figure 5.11 Distribution of clog in the SEN of industry scale after 30 min.

To depict the importance of two-way coupling between fluid flow and clog growth, an additional simulation for the purpose of comparison is performed by ignoring the clog growth (other settings are unchanged). This is made by removal of NMI particles after hitting the wall. To have better comparison between these two cases, with and without clog growth, the distribution of particle deposition mass on the SEN wall at different times is shown in Figure 5.12.

For the simulation case considering the clog growth, the deposition mass in the interior computational cells is projected on the wall boundary cells. This projection allows a comparison of the deposition mass results between two cases. The particle injection rate in the domain for both simulations is 1.21×10^{-4} kg/s. The results show that the critical areas of particle deposition, i.e. clogging, are different for two cases. Without considering clog growth, the critical area is below the gap region. Taking the clog growth into account shows additional deposition, i.e. the gap seems also critical for clogging. Therefore, a numerical model neglecting the effect of clog growth could cause a misleading result.
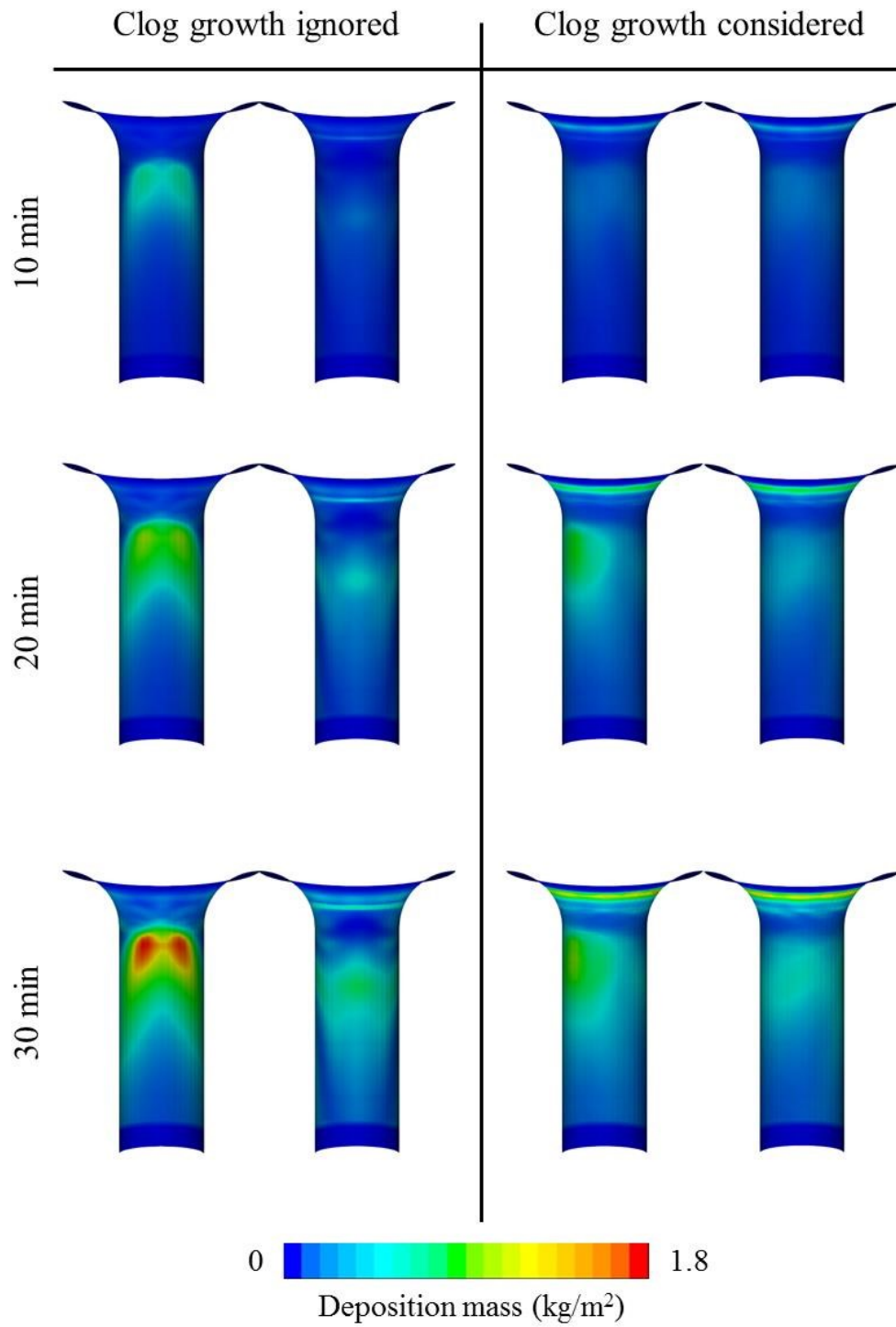
Figure 5.12 Distribution of particle deposition mass on the two halves (front and back) of SEN wall at different times, when clog growth is ignored (left) and considered (right).

5.2.3 Parameter study

Different process parameters (like tundish level, casting speed, etc) and geometrical parameters (like SEN diameter, stopper shape, etc) can influence the SEN clogging. Here, effects of tundish level and SEN diameter on clogging are studied using the developed clogging model.

5.2.3.1 Tundish level

Two tundish levels are compared (0.5 m and 0.8 m). Different tundish levels mean different metallostatic pressure. Hence, to provide a predefined melt flow rate, the stopper gap must be adapted corresponding to the tundish level. As explained for Figure 5.10, at first trial flow simulations are done in whole tundish domain to find the gap size corresponding to the predefined melt flow rate (58.25 kg/s). Then, in the reduced domain the clogging simulation is performed. All other simulation settings are kept unchanged in two simulation cases.

Deposition along the SEN wall is plotted in Figure 5.13. No significant difference is found between the considered cases, although industrial experience showed that increasing the tundish level can lead to the reduction of clogging [1]. Different tundish level practically may change the size and number of inclusions entering the SEN because of different residence time of inclusions in tundish. Coagulation and dynamic change of particle size and particle number inside the tundish could not be considered in the model currently. This may be an explanation for the negligible influence of tundish level on the clogging in the simulation.
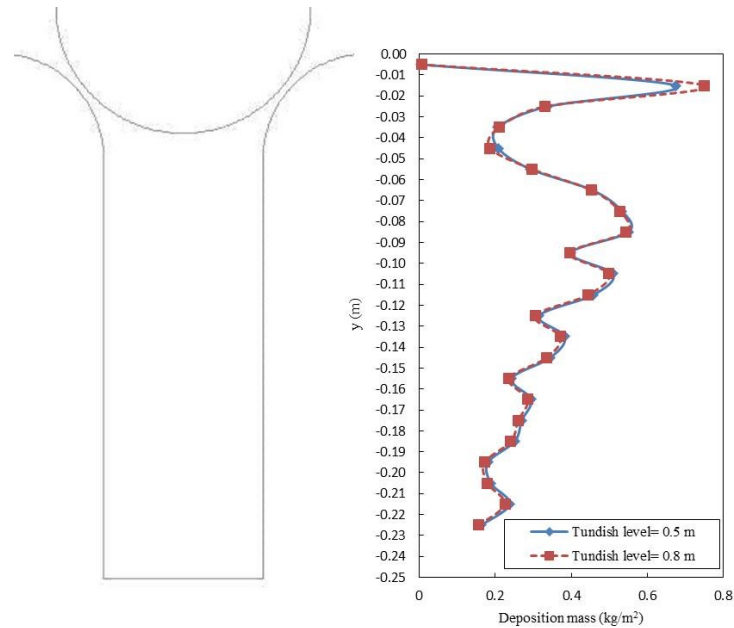
Figure 5.13 Particle deposition mass along the length on SEN wall for two tundish levels after 27 min.

5.2.3.2 SEN diameter

Another study is conducted on the influence of the SEN diameter on clogging. Again, two simulations are compared. The geometries of the near stopper region for both cases are similar. Only the SEN inner diameter is different, one is 75 mm and the other is 80 mm. Therefore, two numerical domains are created with different SEN diameter and different gap sizes to keep the melt flow rate identical for both cases. Here, again the gap size is defined by performing the whole tundish simulations. The results of particle deposition mass for two SEN diameters are shown in Figure 5.14. The results indicate that the smaller SEN diameter leads to smaller amount of clogging and more uniform deposition of particle along the SEN wall.
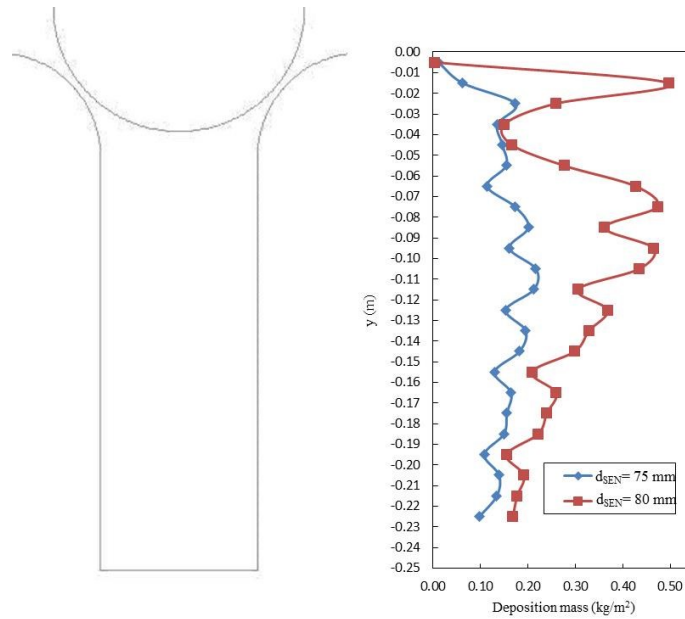
Figure 5.14 Particle deposition mass along the length on the SEN wall for two SEN diameters after 15 min.

The difference in the particle deposition can be found in different flow pattern appearing in two cases. Figure 5.15 and Figure 5.16 show velocity and turbulence kinetic energy during time for two cases, respectively. It can be seen that for the larger SEN the gap size has to be smaller due to keeping the melt flow rate identical. Hence, the velocity magnitude in the gap is enhanced. The enhanced velocity results in more turbulent flow. As the particle deposition on the SEN wall is result of the turbulence kinetic energy, a higher deposition mass is expected for the case with $d_{SEN}=80$ mm than that for the case with $d_{SEN}=75$ mm.
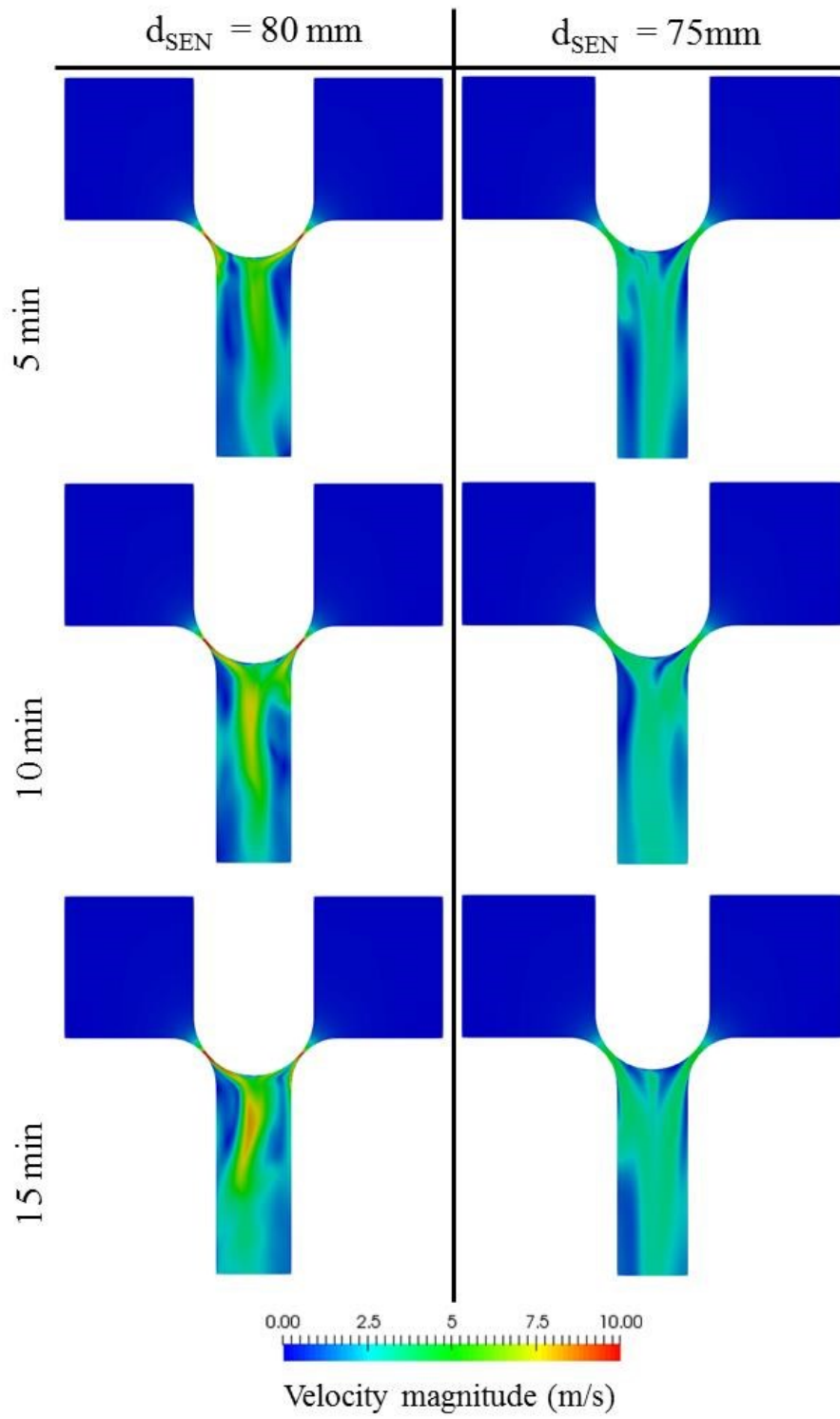
Figure 5.15 Velocity magnitude on a symmetry plane at different times for two SEN diameters.
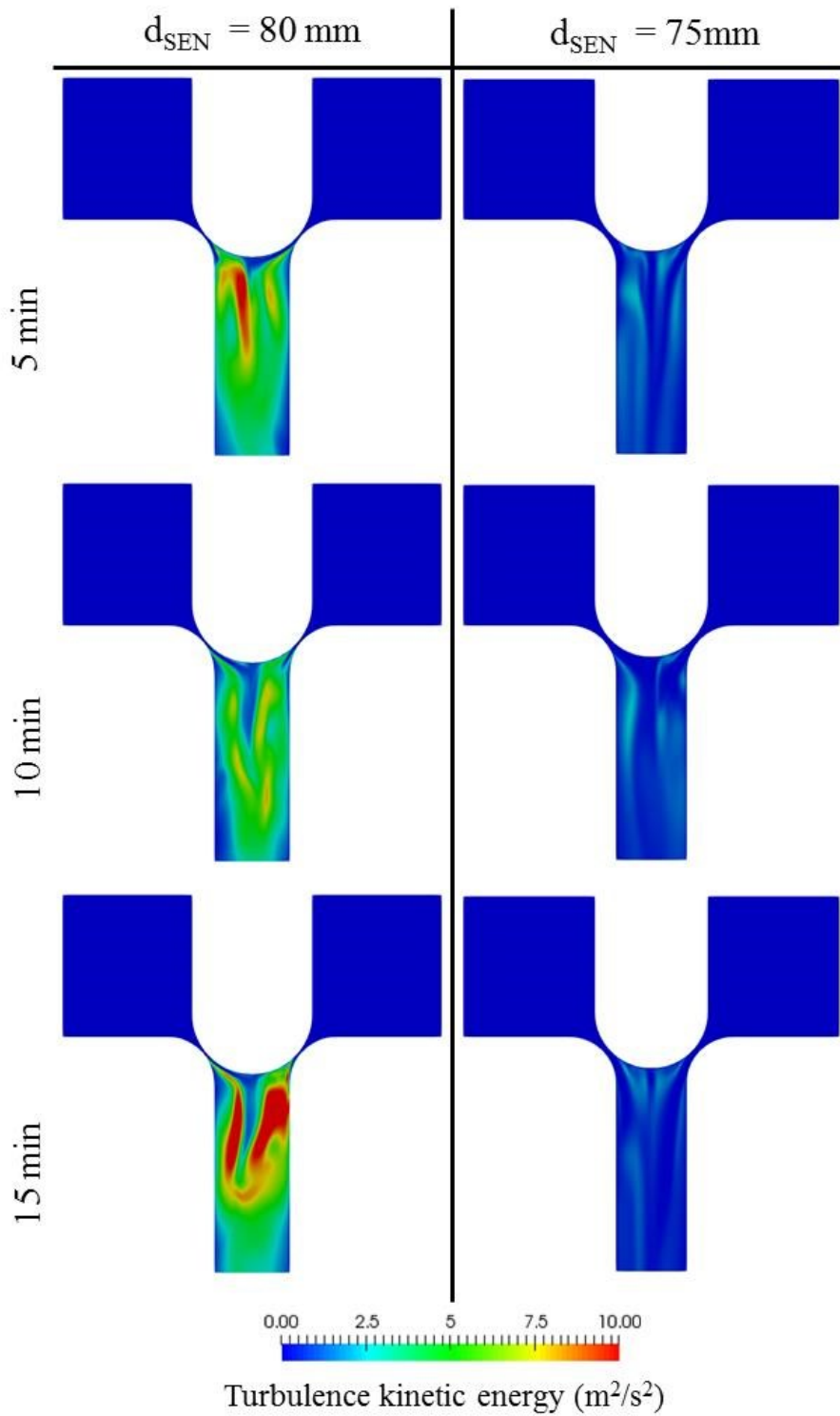
Figure 5.16 Turbulent kinetic energy on a symmetry plane at different times for two SEN diameters.

5.3 Solidification during clogging

Modeling of non-isothermal clogging, considering solidification, has been described in §3.5
. In this part, a non-isothermal clogging simulation is done with aim of investigation of possible solidification in the clog material. The SEN is simplified to a cylindrical domain. For the sake of calculation time, 2D axisymmetric conditions are considered. In Figure 5.17(a), a schematic presentation of continuous casting machine is shown. The computational domain is chosen from the tube shape region of SEN where the outer surface is exposed to the air (Figure 5.17(b)).

(a)   (b)
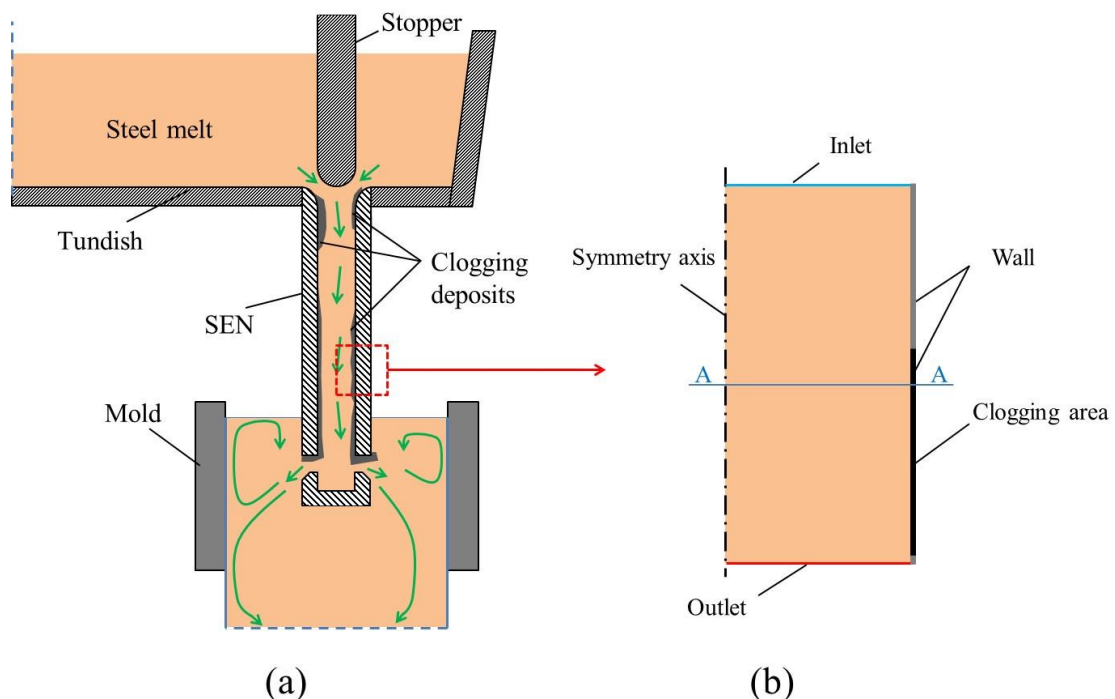
Figure 5.17 (a) Schematic presentation of continuous casting machine, (b) 2D-axisymmetric domain and boundary conditions used in the current simulation.

The dimensions, boundary conditions, and physical properties of materials are summarized in Table 5.2. The heat transfer coefficient of wall is an efficient value including heat conduction through SEN wall (with ~50 mm thickness) and heat convection by air on the outer side of the SEN.

Table 5.2 The dimensions, boundary conditions, and physical properties of materials

Dimensions of domain		Physical properties	
Radius	20 mm	Steel	
Height	60 mm	Density	7020 kg/m³
Boundary conditions		Viscosity	0.0052 kg/(m.s)
Inlet		Specific heat	700 J/(Kg.K)
Velocity	0.85 m/s	Thermal conductivity	26 W/(m.K)
Temperature	1822 K	Liquidus temperature	1807 K
Turbulence kinetic energy	0.00078 m²/s²	Solidus Temperature	1780 K
Specific dissipation rate (ω)	175.76 1/s	Latent heat	243 kJ/kg
Particle mass injection rate	0.0374 kg/s	Alumina	
Outlet		Density	3700 kg/m³
Pressure-outlet	-	Specific heat	880 J/(Kg.K)
Wall		Thermal conductivity	35 W/(m.K)
No-slip	-	Particle diameter	10 μm
Heat transfer coefficient	100 W/(m².K)	$\bar{f}_p$	0.55
Free stream temperature	300 K	D_{pore}	20 μm

The steady state temperature and velocity profiles along a horizontal line (line AA in Figure 5.17(b)), when the no clogging occurs, are shown in Figure 5.18. This result shows that temperature drop near the wall is about 4 K; the wall temperature is still 11 K above the liquidus temperature. Since the flow velocity is high enough to wash the cold melt close to the wall, solidification never happens on the SEN wall.
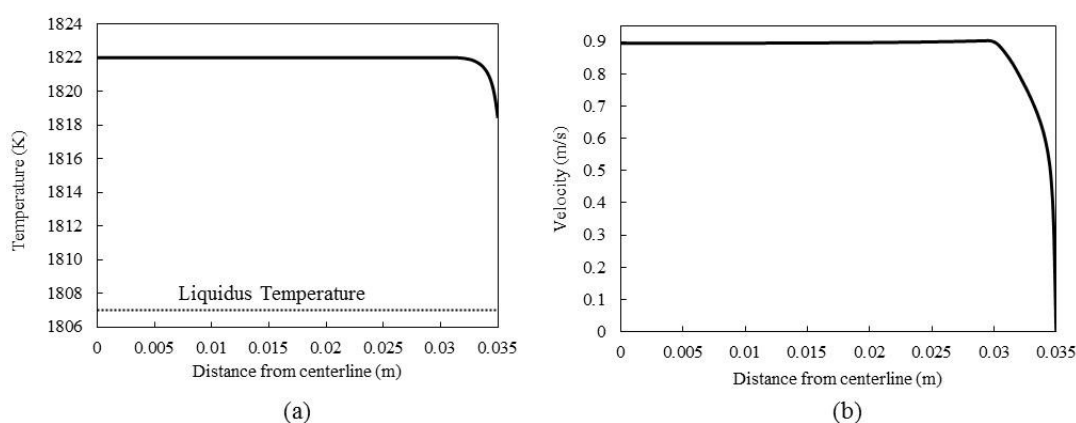
Figure 5.18 Steady state temperature (a) and velocity (b) profiles along AA line shown in Figure 5.17(b).

In the practical conditions of continuous casting, clogging may happen after several hours. Therefore, simulation of real conditions is not feasible due to the too long calculation time

for clogging. To overcome this problem, an exaggerated number of particles is injected in the computational domain to see the clog growth in a shorter time. Hence, the clog growth rate in the current simulation is faster than that in reality. A rough estimation shows that the real injection rate of alumina particles would be around 8.15×10^{-5} kg/s (particle diameter is 10 μm). In the current simulation, the particle injection rate is set to 0.0374 kg/s.

In Figure 5.19, the evolution of clogging is depicted. In the top row, the flow and temperature fields are shown. The thick and thin solid lines represent the clog front and the liquidus isoline of the melt, respectively. In the bottom row, the solid fraction is illustrated. Note that in the clog, the average volume fraction of particle ($\bar{f}_p$) is 0.55. As $f_s + f_\ell + f_p = 1$, the maximum value of f_s can be 0.45, when all of the steel melt in a control volume solidified. Evolution of temperature and velocity profiles along line AA is also indicated in Figure 5.20. The results show that the clog grows from the wall due to the continuous deposition of particles. The clog growth changes the flow field; consequently, the convective heat transfer by the fluid flow is changed. Therefore, the temperature field is adjusted by the clog growth. Due to the very low velocity of the melt in the pores of the clog, the temperature in this region decreases.

After 30, the temperature in the clog is still higher than liquidus temperature. At 40 s, a layer of steel solidifies in the clog. In Figure 5.19, the liquidus temperature actually indicates the position of solidification front, considered in the simulation. At 50 s, the clog thickness increases significantly; therefore, a noticeable solidified metal shell forms in the clog. The results at 40 and 50 s declare that there always is a gap between the clog front and the solidification front (liquidus temperature). One can conclude that solidification during clogging is a consequence of weak melt flow in the clog pores. However, solidification in SEN cannot promote the clog growth because the clog front always is in a temperature close to the bulk temperature and far from the liquidus temperature.

As can be seen in Figure 5.19, clogging starts with covering of the nozzle wall by deposition of the particles (20 and 30 s). The growth of the clog front is not smooth. After a while, some bulges grow at different positions (40 and 50 s). Finally, bulges turn into branches. By impingement of the branches, the flow passage is blocked (this step is not shown in Figure 5.19). When the bulges form on the clog front, the melt flow through the bulges is weakened. Therefore, the heating of the clog front by melt flow decreases. In this case (like 50 s), solidification front can be closer to the clog front than when the clog front is almost smooth (like 30 s).
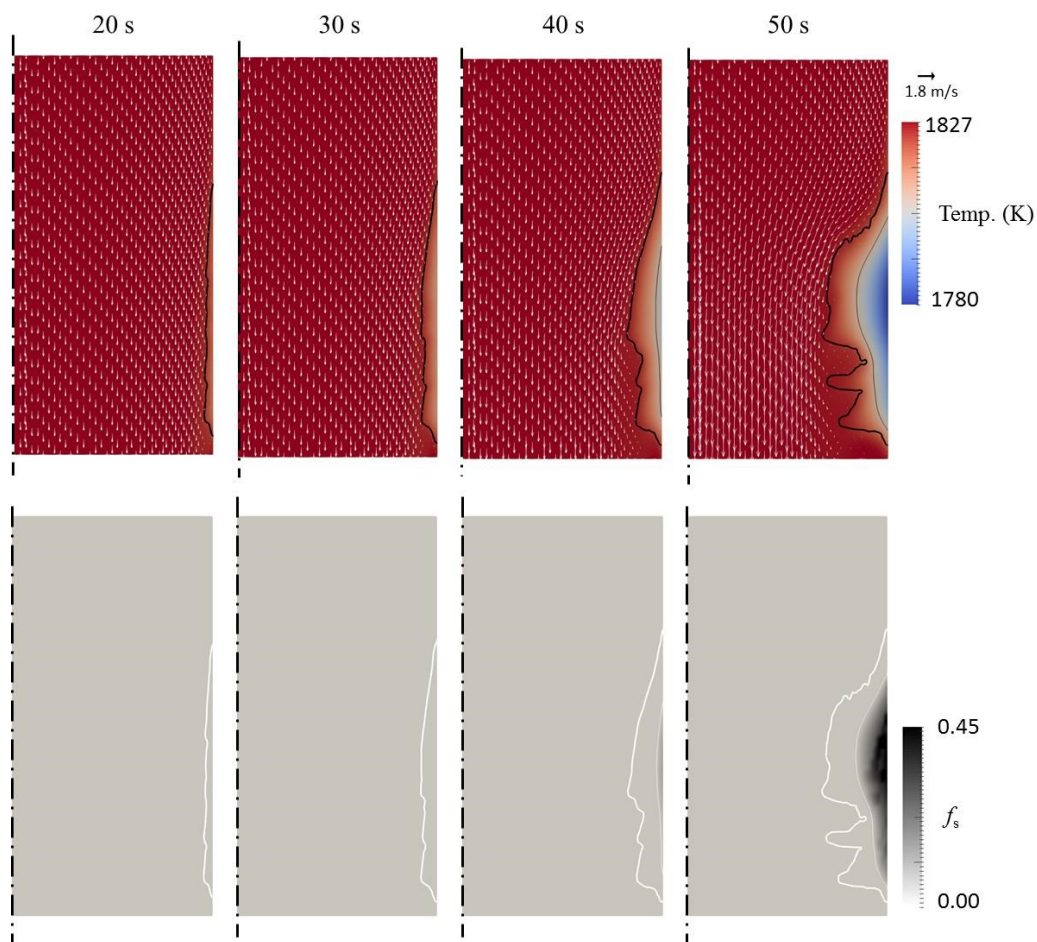
Figure 5.19 Evolution of clogging and its interaction with solidification. The temperature and flow fields are shown on the top row and the solid fraction of steel is indicated on the bottom row. The thick and thin solid lines represent the clog front and liquidus isoline (indicating solidification front), respectively.
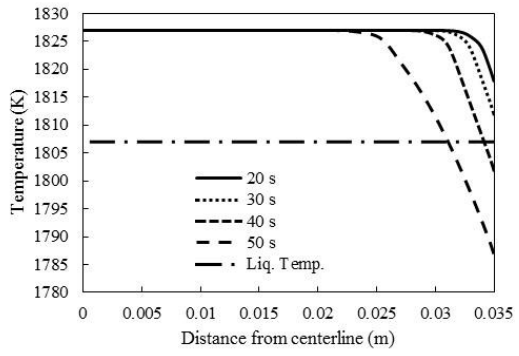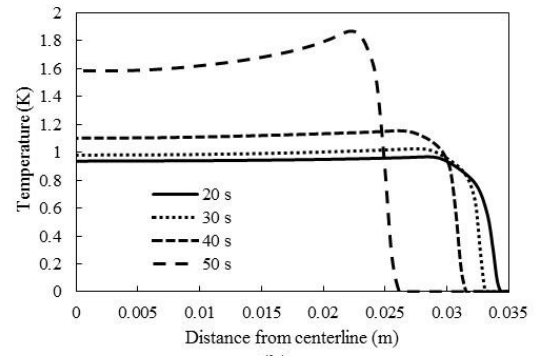
Figure 5.20 Evolution of temperature (a) and velocity (b) profiles along AA line shown in Figure 5.17(b).

6. Discussions

In this chapter, capabilities of the developed clogging model from the numerical and practical point of views are discussed. Moreover, the missing features, required to be implemented in the model to have a comprehensive modeling of clogging process, are addressed.

6.1 Model capabilities

In various fields of study, critical steps of clogging have been investigated, as recently reviewed by Henry and co-workers [108,131], but most available numerical models are valid only for one individual clogging step or combine two steps, and the dynamic growth of the clog and its influence on the flow were ignored. To the author's knowledge, only one recent work has reported a model which has considered the aforementioned three steps of clogging [114]. Similarly, the step of resuspension or fragmentation was not included. In modeling of SEN clogging in continuous casting, models also are limited to transport of NMIs in the steel melt and deposition on the SEN wall while the growth of clog and its influences on the melt flow have been neglected.

Most significant innovations of the current clogging model are as follows.

- Turbulence near the wall determines clogging initialization or deposition of the first layers of particles. The dynamic change of wall roughness by the initial deposition

of non-metallic inclusions (NMIs) on the wall is incorporated into the model, which influences the flow field and turbulence. Therefore, a model considering two-way coupling between particle deposition and fluid flow is provided for the early stage of clogging. If the wall-bounded cell size is much larger than the particle size, a long time is needed for particles to occupy half of the cell, and form a porous medium. Therefore, there is a noticeable delay in the effect of clogging on the flow pattern. Using the dynamic change of wall roughness would overcome this problem and would help to mimic the transient behavior of clogging.

- A new clog growth algorithm on the base of volume average approach is proposed. The clog front is explicitly tracked with a cell marker. The progress of the clog front is governed by continuous deposition of NMIs at the clog front, i.e. in the cells of clog front. According to the volume fraction of the clog in the cell, volume averaged permeability is applied to treat the interactions between the clog and the flow.

- A formulation for isotropic porous media with open pores [143] is employed to calculate permeability of the clog. It is more compatible with the clog structure as observed experimentally than what has been assumed with morphology of homogenously packed spheres. The later may overestimate pressure drop in the clog.

- A volume average interpolation is used to find permeability in the partially-clogged cells (clog front cells). This method is more reliable than simply considering the clog front cell as a uniform porous medium with actual particle fraction (f_p). It has been verified that a simple treatment (considering the clog front cell as a uniform porous medium) would lead to an unrealistic modeling result by overestimating the drag effect of the clog front on the flow. Note that the flow near the clog front will directly influence the deposition rate of the NMIs.

- Using the volume average approach for clog growth, the requirements on computational resources will be reduced. Demands on computational resources are often a limiting factor for most clogging models, especially for industrial cases.

- The model is able to consider non-isothermal conditions and solidification of steel on the SEN wall during continuous casting process. Solidification of steel is an ongoing debate as one of the clogging mechanisms.

- Introducing N-factor (number of representative particles) enhances calculation efficiency. Particle calculation dominates the calculation time in the current clogging model.

Simulation results demonstrate the model capabilities for clogging. Different features of clogging are to be considered:

(1) calculation of particle trajectory with emphasis on near-wall region;

(2) deposition of particle based on its distance to the wall or clog front;

(3) effect of the initial wall roughness and dynamic adaptation of the wall roughness due to particle deposition at the early stage of clogging;

(4) growth of the clog as porous material due to particle deposition;

(5) effect of clogging on fluid flow accordingly in the early stage (by change in wall roughness), and in the later stage (by applying Darcy source term);

(6) non-isothermal melt flow and possible solidification of steel;

(7) simulation of clogging in industry scale.

The numerical model provides a valuable tool to achieve a deeper understanding of clogging, which would never be realized experimentally. The model verifies that clogging is a highly transient, stochastic and self-accelerating process.

The model can be used in industry scale to study real clogging process. Sometimes it is not easy to create mapped hexahedron mesh because of complex geometry of SEN. In this case, a combination of wedge mesh close to the wall, for tracking the clog growth, and

unstructured tetrahedron mesh in the inner regions is recommended. By selecting a proper N-factor, the number of particles is reduced noticeably and calculation speed is increased but real mass of particles is taken into account for clogging. Therefore, clogging simulation of a real SEN can be done in a feasible time. Critical clogging areas can be found transiently and SEN design can be optimized with regard to critical clogging areas.

6.2 Missing points to be included in future model

The current model considers several features of clogging. However, some points are missing or over-simplified. The model can treat the clog as a porous medium, either with large open pores or with randomly packed spheres. This is determinable by the post-mortem analysis of the clog structure. In fact, the clog structure is the outcome of the particle-particle and particle-fluid interactions. These interactions differ for different fluids and particles. Therefore, to perform a reliable simulation, it is crucial to have a sound knowledge of clog structures. Currently, the correlation of clog structures with the inclusion types and steel grades is not well-established. Therefore, the present model is limited to experimental data analysis after clogging for certain conditions. Further numerical and experimental studies will be required to obtain correlations of the clog structure with the NMIs and melt.

NMIs in steel melt are not only spherical, they are often found in the form of clusters, column, or faceted particles [61,77–80]. The shape of the particle influences the clogging behavior. For example, in the laboratory experiments, when major inclusions are in the form of large clusters, the nozzle is found to be blocked by clogging in the upper section [63,144]. This, hence, means that new features should be implemented in the model to deal with different shapes of particles. A further point is the sticking probability of the particle when it hits the nozzle wall. A sticking probability of 100% is here assumed according to

the evidence as found in the literature [81,82,86], but it is also believed that the sticking probability might depend on the wall roughness, local temperature, and the wettability of wall and particles by the melt [108].

The current model is based on many model assumptions. Some of them are necessary, because a precise description of some physical or chemical processes is not available, while some assumptions can be improved in future, i.e. more physical or more chemical processes will be included in the model. They are discussed as follows.

- Transport of particle in the bulk melt and in the near-wall region has to be considered differently. The border between bulk and near-wall regions is defined by $y^+ = 100$ according to the boundary layer theory. However, the near-wall model is applied only for wall-bounded cells due to the difficulty in the calculation of y^+ in the interior cells during clog growth. However, the calculation might not ideally fulfill the condition for the whole thickness of the boundary layer. As a wall-bounded cell is >50% occupied by the clog layer, it is numerically treated as a cell of porous medium. The flow might not behave in coherent structures in the neighboring cell (or cells) anymore. Then there is no wall boundary; instead, there is only clog front with porous medium.

- Currently, when a particle reaches the wall or clog front, there is no chance of it returning to the bulk fluid, i.e. the 'sticking probability' is set 100%. This assumption seems reasonable according to some observations [87]. However, it is still believed that this sticking probability could depend on following chemical or physical processes: chemical reactions on the SEN wall or on the NMI surface which alter their wettability, presence of gas bubble or liquid film of other phases near the wall [9], and energy barrier or repulsive forces when the particle is approaching the wall, etc.; further study is needed.

- Parameters for describing the clog morphology, d_p, $\bar{f}_\mathrm{p}$ and D_pore, are assumed as constants. Average values are estimated, based on the post-mortem analysis of the clog sample. Conducting a study on the variation/distribution of above parameters could be the subject of future investigations.

- Solidification of steel during clogging considered in this work is a simplified mixture model of solidification. The computational control volume is assumed to be mixture of three phases: liquid steel, solid steel and solid particle. More advanced model about solidification in porous medium considering different phases separately would improve knowledge about this topic.

- Argon purging in SEN is a common method in continuous casting. However, in the current version of the clogging model, interactions between inclusion particle and Ar bubble are not considered. Finding accurate interactions between main components (bubble, particle, and wall) in the turbulent boundary layer in microscopic scale requires a deeper study which is out of the scope of the current thesis. To best knowledge of the author providing a precise statement about the effects of Ar purging on SEN clogging is difficult. In fact, it has contradictory effects. Ar purging decrease the pressure loss inside the SEN and leads to less drawing oxygen through the SEN refractory pores. Drawing oxygen into the inner SEN wall and reaction of the oxygen with the steel melt to form oxides is known as one of the clogging mechanisms. Ar bubble may collect inclusions. When a bubble including particles is close to the wall, the chance of reaching to the wall is smaller than when individual particles are at similar location. An alumina particle can pass thin laminar layer adjacent to the wall more easily than a bubble. Therefore, by purging Ar deposition of particles on the wall should be decreased. However, purging Ar bubbles leads to more turbulent flow in the SEN. Hence, the deposition of particles due to the turbulent flow is increased.

- The physics and chemistry of NMI are not constant during the casting process, especially when NMIs are in tundish. The size and shape of a NMI may change based on the chemical composition of the steel alloy and residence time of the NMI in the melt before adhering to SEN wall [78,80,142]. Therefore, a thermodynamic model along with the current clogging model can give more accurate estimation of shape, size, and chemistry of NMIs in the clog material. Moreover, reaction between melt and SEN wall can alter the properties of the wall (like wettability by steel melt and roughness); consequently, the sticking probability of particles on wall may change during the casting process. Chemical reaction in the melt is one of the complex influencing parameters in the SEN clogging.

- The last step of clogging, i.e. fragmentation/detachment of clog material, is not included in the current clogging model. The fragmentation of clog is source of new inclusions enter the mold region, may be captured by solidifying shell, and lead to defects in the final product [63]. Implementation of this step in the clogging model makes it more realistic and gives more statistical information about inclusion distribution.

7. Summary

In this thesis, a new transient model is proposed for simulating the clogging phenomenon in a submerged entry nozzle (SEN) during continuous casting of steel. Development and evaluation of the model with target of simulation of clogging in industry-scale SEN have been done by the following works.

- The model has been made with focus on particle motion in the near-wall region and transient build-up of clog material.

- The model has considered critical steps of the clogging: transport of particles by turbulent flow towards the wall; wall-fluid interactions and adhesion mechanism of deposition; formation and growth of the clog due to the particle deposition.

- The model has been validated by reproducing a laboratory experiment, which was designed to study clogging in SEN. The numerically-calculated clogged section of the nozzle was qualitatively comparable with typically as-clogged sections in laboratory experiments. Quantitatively, the calculated mass flow rate through the nozzle during the clogging process as a function of time also agreed with the experimentally-monitored results.

- Uncertainties for modeling parameters such as mesh size, Lagrangian time scale (T_{L}), correction factor (n) in the interpolation of clog permeability, and porosity in the clog materials, have been studied.

- The model has been evaluated referring to its sensitivity to the mesh type. The dependency of the model on mesh type has been studied, because the geometry of SEN is complex and creation of unstructured tetrahedron mesh is more convenient than mapped hexahedron mesh.

- The model has been verified with regard to accuracy and efficiency of calculation. Due to the huge real number of particles in SEN, all particles cannot be accounted individually. Therefore, N-factor has been necessarily introduced to improve the calculation efficiency.

- The model has been upgraded to a non-isothermal model and solidification of steel during the SEN clogging in continuous casting has been investigated.

- Parameter studies have been done to investigate effects of a process parameter (tundish level) and a SEN design parameter (SEN diameter) on clogging behavior of industry-scale SEN.

The main conclusions of the aforementioned works can be summarized as follows.

- New knowledge about clogging can be derived from the laboratory scale modeling results: (1) Clogging is a transient process, and it includes the initial coverage of the nozzle wall with deposited particles, the evolution of a bulged clog front, and then the development of a branched structure. (2) Clogging is a stochastic and self-accelerating process.

- The modeling result on particle deposition becomes insensitive to T_L and n when they are set at close to 6 μs and 5, respectively.

- When creation of hexahedron mesh is too difficult, it is recommended to use a combination of wedge mesh close to the wall, for tracking the clog growth, and tetrahedron mesh in the inner regions. Wedge mesh behaves similarly to hexahedron mesh regarding the clog growth.

- The calculation results of particle deposition are not sensitive to the N-factor at the initial clogging stage when particle deposition is taken into account by enhancement of the wall roughness. However, during the late stage of clogging when particle deposition mostly leads to the growth of a porous medium, N-factor would affect the model accuracy, depending on the particle size and mesh size.

- By selecting an appropriate N-factor (1000, corresponding to $\alpha = 6 \times 10^{-5}$), the calculation time for clogging in an industry-scale SEN would be reduced to a reasonable time (~75 hours), i.e. the calculation efficiency is significantly improved.

- Clogging promotes the solidification inside the clog.

- No significant difference is found between the cases with different tundish levels (0.5 and 0.8 m).

- SEN with 75 mm diameter leads to smaller amount of clogging and more uniform deposition of particle along the SEN wall than those of SEN with 80 mm diameter.

In order to simulate the clogging with more quantitative accuracy, following points are needed to be included in future:

- particles with non-spherical shapes;

- effects of argon purging in SEN as well as interactions between argon bubble, NMI and SEN wall;

- porosity and morphological structure of clog as a function of the size and shape of particles;

- more accurate physical or chemical mechanisms of particle sticking to the nozzle wall;

- chemical reactions on SEN wall;

- fragmentation (detachment) of clog material.

8. References

[1]   S. Rödl, H. Schuster, S. Ekerot, G. Xia, N. Veneri, F. Ferro, S. Baragiola, P. Rossi, S. Fera, V. Colla, others, New strategies for clogging prevention for improved productivity and steel quality, 2008.

[2]   www.stahl-online.de, (n.d.).

[3]   Q. Yuan, B.G. Thomas, S.P. Vanka, Study of transient flow and particle transport in continuous steel caster molds: Part II. Particle transport, Metall. Mater. Trans. B. 35 (2004) 703–714. doi:10.1007/s11663-004-0010-z.

[4]   H. Bai, B.G. Thomas, Turbulent flow of liquid steel and argon bubbles in slide-gate tundish nozzles: Part II. Effect of operation conditions and nozzle design, Metall. Mater. Trans. B. 32 (2001) 269–284. doi:10.1007/s11663-001-0050-6.

[5]   H. Bai, B.G. Thomas, Turbulent flow of liquid steel and argon bubbles in slide-gate tundish nozzles: Part I. model development and validation, Metall. Mater. Trans. B. 32 (2001) 253–267. doi:10.1007/s11663-001-0049-z.

[6]   M. Mohammadi-Ghaleni, M. Asle Zaeem, J.D. Smith, R. O'Malley, Computational Fluid Dynamics Study of Molten Steel Flow Patterns and Particle–Wall Interactions Inside a Slide-Gate Nozzle by a Hybrid Turbulent Model, Metall. Mater. Trans. B. 47 (2016) 3056–3065. doi:10.1007/s11663-016-0729-3.

[7]   M. Mohammadi-Ghaleni, M. Asle Zaeem, J.D. Smith, R. O'Malley, R. O'Malley, Comparison of CFD Simulations with Experimental Measurements of Nozzle Clogging in Continuous Casting of Steels, Metall. Mater. Trans. B. 47 (2016) 3384–3393. doi:10.1007/s11663-016-0798-3.

[8]   M. Javurek, M. Thumfart, R. Wincor, Investigations on Flow Pattern and Pressure inside SEN below Stopper Rod, Steel Res. Int. 81 (2010) 668–674. doi:10.1002/srin.201000119.

[9]   M. Thumfart, M. Javurek, Low Pressure Effects in SEN-Stopper Region in Continuous Casting, Steel Res. Int. 86 (2015) 25–32. doi:10.1002/srin.201300448.

[10]   R. Chaudhary, G.-G. Lee, B.G. Thomas, S.-H. Kim, Transient Mold Fluid Flow with Well- and Mountain-Bottom Nozzles in Continuous Casting of Steel, Metall. Mater. Trans. B. 39 (2008) 870–884. doi:10.1007/s11663-008-9192-0.

[11]   L. Zhang, D. Chen, M. Long, H. Chen, Y. Huang, Z. Dong, Study on the Fluid Flow in a Semi-Open-Stream-Poured Beam Blank Continuous Casting Mold with Submerged Refractory Funnels by Multiphase Modeling, Metals (Basel). 6 (2016).

[12] W.V. Gabriel, J.J.M. Peixoto, C.A. Silva, C.A. da Silva, I.A. da Silva, V. Seshadri, The influence of the geometry of a three orifice nozzle on the flow field inside a beam blank mold, J. Mater. Process. Technol. 245 (2017) 232–240. doi:https://doi.org/10.1016/j.jmatprotec.2017.02.014.

[13] D. LI, Z. SU, K. MARUKAWA, J. HE, Simulation on Effect of Divergent Angle of Submerged Entry Nozzle on Flow and Temperature Fields in Round Billet Mold in Electromagnetic Swirling Continuous Casting Process, J. Iron Steel Res. Int. 21 (2014) 159–165. doi:https://doi.org/10.1016/S1006-706X(14)60025-X.

[14] I. Calderon-Ramos, R.D. Morales, Influence of Turbulent Flows in the Nozzle on Melt Flow Within a Slab Mold and Stability of the Metal--Flux Interface, Metall. Mater. Trans. B. 47 (2016) 1866–1881. doi:10.1007/s11663-015-0569-6.

[15] R. Sambasivam, Clogging resistant submerged entry nozzle design through mathematical modelling, Ironmak. Steelmak. 33 (2006) 439–453. doi:10.1179/174328106X118198.

[16] F.M. Najjar, B.G. Thomas, D.E. Hershey, Numerical study of steady turbulent flow through bifurcated nozzles in continuous casting, Metall. Mater. Trans. B. 26 (1995) 749–765. doi:10.1007/BF02651721.

[17] B. Greis, R. Bahrmann, A. Rückert, H. Pfeifer, Investigations of Flow Pattern in the SEN Regarding Different Stopper Rod Geometries, Steel Res. Int. 86 (2015) 1469–1479. doi:10.1002/srin.201400319.

[18] S. Wu, J. Zhang, Z. Li, Mathematic Model of SEN Clogging During Continuous Casting of Steel, J. Iron Steel Res. Int. 17 (2010) 6–9. doi:10.1016/S1006-706X(10)60119-7.

[19] Y.-H. Ho, C.-H. Chen, W.-S. Hwang, Analysis of Molten Steel Flow in Slab Continuous Caster Mold, ISIJ Int. 34 (1994) 255–264. doi:10.2355/isijinternational.34.255.

[20] C.A. Real-Ramirez, I. Carvajal-Mariscal, F. Sanchez-Silva, F. Cervantes-de-la-Torre, J. Diaz-Montes, J. Gonzalez-Trejo, Three-Dimensional Flow Behavior Inside the Submerged Entry Nozzle, Metall. Mater. Trans. B. 49 (2018) 1644–1657. doi:10.1007/s11663-018-1281-0.

[21] C.A. Real-Ramirez, R. Miranda-Tello, I. Carvajal-Mariscal, F. Sanchez-Silva, J. Gonzalez-Trejo, Hydrodynamic Study of a Submerged Entry Nozzle with Flow Modifiers, Metall. Mater. Trans. B. 48 (2017) 1358–1375. doi:10.1007/s11663-016-0863-y.

[22] R. Sánchez-Pérez, L. García-Demedices, J.P. Ramos, M. Díaz-Cruz, R.D. Morales, Dynamics of coupled and uncoupled two-phase flows in a slab mold, Metall. Mater. Trans. B. 35 (2004) 85–99. doi:10.1007/s11663-004-0099-0.

[23] C. Pfeiler, B.G. Thomas, M. Wu, A. Ludwig, A. Kharicha, Solidification and Particle Entrapment during Continuous Casting of Steel, Steel Res. Int. 79 (2008) 599–607. doi:10.1002/srin.200806172.

[24] Q. Fang, H. Ni, H. Zhang, B. Wang, X. Song, C. Liu, Influence of SEN on Flow, Solidification, and Solute Transport in Bloom Casting Mold, JOM. 70 (2018) 719–725. doi:10.1007/s11837-018-2770-y.

[25] Q. Fang, H. Ni, H. Zhang, B. Wang, Z. Lv, The Effects of a Submerged Entry Nozzle on Flow and Initial Solidification in a Continuous Casting Bloom Mold with

Electromagnetic Stirring, Metals (Basel). 7 (2017).

[26] H. Bai, B.G. Thomas, Effects of clogging, argon injection, and continuous casting conditions on flow and air aspiration in submerged entry nozzles, Metall. Mater. Trans. B. 32 (2001) 707–722. doi:10.1007/s11663-001-0125-4.

[27] C. Pfeiler, M. Wu, A. Ludwig, Influence of argon gas bubbles and non-metallic inclusions on the flow behavior in steel continuous casting, Mater. Sci. Eng. A. 413–414 (2005) 115–120. doi:https://doi.org/10.1016/j.msea.2005.08.178.

[28] L. Zhang, Y. Wang, X. Zuo, Flow Transport and Inclusion Motion in Steel Continuous-Casting Mold under Submerged Entry Nozzle Clogging Condition, Metall. Mater. Trans. B. 39 (2008) 534–550. doi:10.1007/s11663-008-9154-6.

[29] W. Zhang, J. Gao, P.K. Rohatgi, H. Zhao, Y. Li, Effect of the depth of the submerged entry nozzle in the mold on heat, flow and solution transport in double-stream-pouring continuous casting, J. Mater. Process. Technol. 209 (2009) 5536–5544. doi:https://doi.org/10.1016/j.jmatprotec.2009.05.009.

[30] B.G. Thomas, Q. Yuan, S. Sivaramakrishnan, T. Shi, S.P. Vanka, M.B. Assar, Comparison of Four Methods to Evaluate Fluid Velocities in a Continuous Slab Casting Mold, ISIJ Int. 41 (2001) 1262–1271. doi:10.2355/isijinternational.41.1262.

[31] Q. Yuan, B.G. Thomas, S.P. Vanka, Study of transient flow and particle transport in continuous steel caster molds: Part I. Fluid flow, Metall. Mater. Trans. B. 35 (2004) 685–702. doi:10.1007/s11663-004-0009-5.

[32] R. Singh, B.G. Thomas, S.P. Vanka, Large Eddy Simulations of Double-Ruler Electromagnetic Field Effect on Transient Flow During Continuous Casting, Metall. Mater. Trans. B. 45 (2014) 1098–1115. doi:10.1007/s11663-014-0022-2.

[33] R. Singh, B.G. Thomas, S.P. Vanka, Effects of a Magnetic Field on Turbulent Flow in the Mold Region of a Steel Caster, Metall. Mater. Trans. B. 44 (2013) 1201–1221. doi:10.1007/s11663-013-9877-x.

[34] R. Chaudhary, C. Ji, B.G. Thomas, S.P. Vanka, Transient Turbulent Flow in a Liquid-Metal Model of Continuous Casting, Including Comparison of Six Different Methods, Metall. Mater. Trans. B. 42 (2011) 987–1007. doi:10.1007/s11663-011-9526-1.

[35] R. Chaudhary, B.G. Thomas, S.P. Vanka, Effect of Electromagnetic Ruler Braking (EMBr) on Transient Turbulent Flow in Continuous Slab Casting using Large Eddy Simulations, Metall. Mater. Trans. B. 43 (2012) 532–553. doi:10.1007/s11663-012-9634-6.

[36] S.-M. Cho, S.-H. Kim, B.G. Thomas, Transient Fluid Flow during Steady Continuous Casting of Steel Slabs: Part I. Measurements and Modeling of Two-phase Flow, ISIJ Int. 54 (2014) 845–854. doi:10.2355/isijinternational.54.845.

[37] D. Li, Z. Su, J. Chen, Q. Wang, Y. Yang, K. Nakajima, K. Marukawa, J. He, Effects of Electromagnetic Swirling Flow in Submerged Entry Nozzle on Square Billet Continuous Casting of Steel Process, ISIJ Int. 53 (2013) 1187–1194. doi:10.2355/isijinternational.53.1187.

[38] H. Bai, M. Ersson, P. Jönsson, Experimental Validation and Numerical Analysis of the Swirling Flow in a Submerged Entry Nozzle and Mold by Using a Reverse TurboSwirl in a Billet Continuous Casting Process, Steel Res. Int. 88 (2017) 1600339. doi:10.1002/srin.201600339.

[39] P. Ni, L.T.I. Jonsson, M. Ersson, P.G. Jönsson, A New Tundish Design to Produce a Swirling Flow in the SEN During Continuous Casting of Steel, Steel Res. Int. 87 (2016) 1356–1365. doi:10.1002/srin.201500407.

[40] P. Ni, M. Ersson, L.T.I. Jonsson, T. Zhang, P.G. JÖNSSON, Numerical Study on the Influence of a Swirling Flow Tundish on Multiphase Flow and Heat Transfer in Mold, Metals (Basel). 8 (2018).

[41] S. Yokoya, R. Westoff, Y. Asako, S. Hara, J. Szekely, Numerical Study of Immersion Nozzle Outlet Flow Pattern with Swirling Flow in Continuous Casting, ISIJ Int. 34 (1994) 889–895. doi:10.2355/isijinternational.34.889.

[42] S. Yokoya, S. Takagi, M. Iguchi, Y. Asako, R. Westoff, S. Hara, Swirling Effect in Immersion Nozzle on Flow and Heat Transport in Billet Continuous Casting Mold, ISIJ Int. 38 (1998) 827–833. doi:10.2355/isijinternational.38.827.

[43] S. Yokoya, S. Takagi, M. Iguchi, K. Marukawa, S. Hara, Swirling Flow Effect in Immersion Nozzle on Flow in Slab Continuous Casting Mold, ISIJ Int. 40 (2000) 578–583. doi:10.2355/isijinternational.40.578.

[44] Y. Tsukaguchi, O. Nakamura, P. Jönsson, S. Yokoya, T. Tanaka, S. Hara, Design of Swirling Flow Submerged Entry Nozzles for Optimal Head Consumption between Tundish and Mold, ISIJ Int. 47 (2007) 1436–1443. doi:10.2355/isijinternational.47.1436.

[45] Y. Tsukaguchi, H. Hayashi, H. Kurimoto, S. Yokoya, K. Marukawa, T. Tanaka, Development of Swirling-flow Submerged Entry Nozzles for Slab Casting, ISIJ Int. 50 (2010) 721–729. doi:10.2355/isijinternational.50.721.

[46] B.G. Thomas, Review on Modeling and Simulation of Continuous Casting, Steel Res. Int. 89 (2018) 1700312. doi:10.1002/srin.201700312.

[47] R. Liu, B.G. Thomas, Model of Gas Flow Through Porous Refractory Applied to an Upper Tundish Nozzle, Metall. Mater. Trans. B. 46 (2015) 388–405. doi:10.1007/s11663-014-0198-5.

[48] K. Timmel, C. Kratzsch, A. Asad, D. Schurmann, R. Schwarze, S. Eckert, Experimental and Numerical Modeling of Fluid Flow Processes in Continuous Casting: Results from the LIMMCAST-Project, IOP Conf. Ser. Mater. Sci. Eng. 228 (2017) 12019. http://stacks.iop.org/1757-899X/228/i=1/a=012019.

[49] K. Jin, B.G. Thomas, X. Ruan, Modeling and Measurements of Multiphase Flow and Bubble Entrapment in Steel Continuous Casting, Metall. Mater. Trans. B. 47 (2016) 548–565. doi:10.1007/s11663-015-0525-5.

[50] L. Zhang, J. Aoki, B.G. Thomas, Inclusion removal by bubble flotation in a continuous casting mold, Metall. Mater. Trans. B. 37 (2006) 361–379. doi:10.1007/s11663-006-0021-z.

[51] J. Klostermann, H. Chaves, R. Schwarze, Investigation of the Gas-Liquid Flow in a Stopper Rod Controlled SEN, Steel Res. Int. 78 (2007) 595–601. doi:10.1002/srin.200706254.

[52] H.L. Yang, P. He, Y.C. Zhai, Removal Behavior of Inclusions in Molten Steel by Bubble Wake Flow Based on Water Model Experiment, ISIJ Int. 54 (2014) 578–581. doi:10.2355/isijinternational.54.578.

[53] V. Singh, S.K. Dash, J.S. Sunitha, S.K. Ajmani, A.K. Das, Experimental Simulation and Mathematical Modeling of Air Bubble Movement in Slab Caster Mold, ISIJ Int.

46 (2006) 210–218. doi:10.2355/isijinternational.46.210.

[54] Y. Kwon, J. Zhang, H.-G. Lee, Water Model and CFD Studies of Bubble Dispersion and Inclusions Removal in Continuous Casting Mold of Steel, ISIJ Int. 46 (2006) 257–266. doi:10.2355/isijinternational.46.257.

[55] B.G. Thomas, X. Huang, R.C. Sussman, Simulation of Argon Gas Flow Effects in a Continuous Slab Caster, Metall. Mater. Trans. B. 25 (1994) 527–547. doi:10.1007/BF02650074.

[56] B. Li, T. Okane, T. Umeda, Modeling of molten metal flow in a continuous casting process considering the effects of argon gas injection and static magnetic-field application, Metall. Mater. Trans. B. 31 (2000) 1491–1503. doi:10.1007/s11663-000-0034-y.

[57] H. Bai, B.G. Thomas, Bubble formation during horizontal gas injection into downward-flowing liquid, Metall. Mater. Trans. B. 32 (2001) 1143–1159. doi:10.1007/s11663-001-0102-y.

[58] T. Zhang, Z.G. Luo, C.L. Liu, H. Zhou, Z.S. Zou, A mathematical model considering the interaction of bubbles in continuous casting mold of steel, Powder Technol. 273 (2015) 154–164. doi:10.1016/j.powtec.2014.12.036.

[59] G. Wang, H. Zhou, Q. Tian, X. Ai, L. Zhang, Motion of Single Bubble and Interactions between Two Bubbles in Liquid Steel, ISIJ Int. 57 (2017) 805–813. doi:10.2355/isijinternational.ISIJINT-2016-670.

[60] L. Zhang, S. Taniguchi, Fundamentals of inclusion removal from liquid steel by bubble flotation, Int. Mater. Rev. 45 (2000) 59–82. doi:10.1179/095066000101528313.

[61] B.G. Thomas, Q. Yuan, S. Mahmood, R. Liu, R. Chaudhary, Transport and Entrapment of Particles in Steel Continuous Casting, Metall. Mater. Trans. B. 45 (2014) 22–35. doi:10.1007/s11663-013-9916-7.

[62] Z. Liu, F. Qi, B. Li, M. Jiang, Multiple Size Group Modeling of Polydispersed Bubbly Flow in the Mold: An Analysis of Turbulence and Interfacial Force Models, Metall. Mater. Trans. B. 46 (2015) 933–952. doi:10.1007/s11663-014-0255-0.

[63] N. Kojola, S. Ekerot, M. Andersson, P.G. Jönsson, Pilot plant study of nozzle clogging mechanisms during casting of REM treated stainless steels, Ironmak. Steelmak. 38 (2011) 1–11. doi:10.1179/030192310X12690127076398.

[64] Y. Miki, H. Kitaoka, T. Sakuraya, T. Fujii, Mechanism for separating inclusions from molten steel stirred with a rotating magnetic field, ISIJ Int. Vol. 32 (1992) 142–149. doi:10.2355/isijinternational.32.142.

[65] S. Basu, S.K. Choudhary, N.U. Girase, Nozzle Clogging Behaviour of Ti-bearing Al-killed Ultra Low Carbon Steel, ISIJ Int. 44 (2004) 1653–1660. doi:10.2355/isijinternational.44.1653.

[66] K. Sasai, Y. Mizukami, Reaction Mechanism between Alumina Graphite Immersion Nozzle and Low Carbon Steel., ISIJ Int. 34 (1994) 802–809. doi:10.2355/isijinternational.34.802.

[67] Y. Vermeulen, B. Coletti, B. Blanpain, P. Wollants, J. Vleugels, Material evaluation to prevent nozzle clogging during continuous casting of Al killed steels, ISIJ Int. 42 (2002) 1234–1240. doi:10.2355/isijinternational.42.1234.

[68] P.M. Benson, Q.K. Robinson, C. Dumazeau, New technique for the Prevention of Alumina Build-up in Submerged entry Nozzles for Continuous casting, in: Unitecr'93 Congr. Refract. New World Econ. Proc. Conf. Sao Paulo, 1993.

[69] G.C. Duderstadt, R.K. Iyengar, J.M. Matesa, Tundish nozzle blockage in continuous casting, JOM. 20 (1968) 89–94.

[70] J.W. Farrell, D.C. Hilty, Steel Flow Through Nozzles: Influence of Deoxidizers, in: Electr. Furn. Proc., 1971: pp. 31–46.

[71] K.G. Rackers, B.G. Thomas, Clogging in Continuous Casting Nozzles, in: 78th Steelmak. Conf. Proc., 1995: pp. 723–734.

[72] B.G. Thomas, H. Bai, Tundish nozzle clogging-application of computational models, in: Steelmak. Conf. Proc., 2001: pp. 895–912.

[73] S.N. Singh, Mechanism of alumina buildup in tundish nozzles during continuous casting of aluminum-killed steels, Metall. Trans. 5 (1974) 2165–2178.

[74] L. Trueba, K.D. Peaslee, J.D. Smith, M. Karakus, K. Trueba, K.D. Peaslee, J.D. Smith, M. Karakus, Effect of Nozzle Base Material on the Rate of Clogging during the Continuous Casting of Aluminum-Killed Steels, Steel Res. Int. 77 (2006) 37–47. doi:10.1002/srin.200606128.

[75] M. Long, X. Zuo, L. Zhang, D. Chen, Kinetic Modeling on Nozzle Clogging During Steel Billet Continuous Casting, ISIJ Int. 50 (2010) 712–720. doi:10.2355/isijinternational.50.712.

[76] L.F. Zhang, B.G. Thomas, State of the Art in Evaluation and Control of Steel Cleanliness, ISIJ Int. 43 (2003) 271–291. doi:10.2355/isijinternational.43.271.

[77] L. Zhang, W. Pluschkell, Nucleation and growth kinetics of inclusions during liquid steel deoxidation, Ironmak. Steelmak. 30 (2003) 106–110. doi:10.1179/030192303225001766.

[78] Z. Deng, M. Zhu, Y. Zhou, D. Sichen, Attachment of Alumina on the Wall of Submerged Entry Nozzle During Continuous Casting of Al-Killed Steel, Metall. Mater. Trans. B. 47 (2016) 2015–2025. doi:10.1007/s11663-016-0624-y.

[79] R. Dekkers, B. Blanpain, P. Wollants, F. Haers, B. Gommers, C. Vercruyssen, A morphological comparison between inclusions in aluminium killed steels and deposits in submerged entry nozzle, Steel Res. Int. 74 (2003) 351–355.

[80] D. Janis, A. Karasev, R. Inoue, P.G. Jönsson, A Study of Cluster Characteristics in Liquid Stainless Steel and in a Clogged Nozzle, Steel Res. Int. 86 (2015) 1271–1278. doi:10.1002/srin.201400316.

[81] K. Sasai, Y. Mizukami, Mechanism of Alumina Adhesion to Continuous Caster Nozzle with Reoxidation of Molten Steel., ISIJ Int. 41 (2001) 1331–1339. doi:10.2355/isijinternational.41.1331.

[82] E. Kawecka-Cebula, Z. Kalicka, J. Wypartowicz, Filtration of nonmetallic inclusions in steel, Arch. Metall. Mater. 51 (2006) 261–268.

[83] K. Sasai, Direct Measurement of Agglomeration Force Exerted between Alumina Particles in Molten Steel, ISIJ Int. 54 (2014) 2780–2789. doi:10.2355/isijinternational.54.2780.

[84] K. Sasai, Interaction between Alumina Inclusions in Molten Steel Due to Cavity Bridge Force, ISIJ Int. 56 (2016) 1013–1022. doi:10.2355/isijinternational.ISIJINT-

2016-038.

[85] K. Nakajima, S. Mizoguchi, Capillary interaction between inclusion particles on the 16Cr stainless steel melt surface, Metall. Mater. Trans. B. 32 (2001) 629–641. doi:10.1007/s11663-001-0118-3.

[86] F. Heuzeroth, J. Fritzsche, E. Werzner, M.A.A. Mendes, S. Ray, D. Trimis, U.A. Peuker, Viscous force - An important parameter for the modeling of deep bed filtration in liquid media, Powder Technol. 283 (2015) 190–198. doi:10.1016/j.powtec.2015.05.018.

[87] K. Uemura, M. Takahashi, S. Koyama, M. Nitta, Filtration Mechamism of Non-metallic Inclusions in Steel by Ceramic Loop Filter., ISIJ Int. 32 (1992) 150–156. doi:10.2355/isijinternational.32.150.

[88] T. Mizoguchi, Y. Ueshima, M. Sugiyama, K. Mizukami, Influence of Unstable Non-equilibrium Liquid Iron Oxide on Clustering of Alumina Particles in Steel, ISIJ Int. 53 (2013) 639–647. doi:10.2355/isijinternational.53.639.

[89] U. Dieguez Salgado, C. Weiß, S.K. Michelic, C. Bernhard, Fluid Force-Induced Detachment Criteria for Nonmetallic Inclusions Adhered to a Refractory/Molten Steel Interface, Metall. Mater. Trans. B. 49 (2018) 1632–1643. doi:10.1007/s11663-018-1271-2.

[90] U. Diéguez Salgado, P. Dorrer, S.K. Michelic, C. Bernhard, Experimental Investigation of the System Nonmetallic Inclusion-Molten Steel-Refractory System at High Temperatures, J. Mater. Eng. Perform. (2018). doi:10.1007/s11665-018-3468-6.

[91] S.K. Ray, M. Isac, R.I.L. Guthrie, Modelling performance of four-strand, 12 t, delta shaped continuous casting tundish fitted with different flow modifying arrangements for better steel quality, Ironmak. Steelmak. 38 (2011) 173–180. doi:10.1179/030192310X12816231892224.

[92] C.M. Fan, R.J. Shie, W.S. Hwang, Studies by mathematical and physical modelling of fluid flow and inclusion removal phenomena in slab tundish for casting stainless steel using various flow control device designs, Ironmak. Steelmak. 30 (2003). doi:10.1179/030192303225004015.

[93] A.K. Sinha, Y. Sahai, Mathematical Modeling of Inclusion Transport and Removal in Continuous Casting Tundishes., ISIJ Int. 33 (1993) 556–566. doi:10.2355/isijinternational.33.556.

[94] L. Zhang, S. Taniguchi, K. Cai, Fluid flow and inclusion removal in continuous casting tundish, Metall. Mater. Trans. B. 31 (2000) 253–266. doi:10.1007/s11663-000-0044-9.

[95] S. García-Hernández, J. de J. Barreto, J.A. Ramos-Banderas, G. Solorio-Diaz, S. Garćia-Hernández, J. De J. Barreto, J.A. Ramos-Banderas, G. Solorio-Diaz, Modeling Study of the Vortex and Short Circuit Flow Effect on Inclusion Removal in a Slab Tundish, Steel Res. Int. 81 (2010) 453–460. doi:10.1002/srin.200900152.

[96] K. Takahashi, M. Ando, T. Ishii, Numerical Investigation of Unsteady Molten Steel Flow and Inclusion Behavior in the Tundish in the Ladle Change Period, ISIJ Int. 54 (2014) 304–310. doi:10.2355/isijinternational.54.304.

[97] M.K. Sardar, S. Mukhopadhyay, U.K. Bandopadhyay, S.K. Dhua, Optimisation of Inclusion Chemistry by Improved Steel Cleanliness and Optimum Calcium

Treatment, Steel Res. Int. 78 (2007) 136–140. doi:10.1002/srin.200705870.

[98]   Z. Deng, M. Zhu, B. Zhong, D. Sichen, Attachment of Liquid Calcium Aluminate Inclusions on Inner Wall of Submerged Entry Nozzle during Continuous Casting of Calcium- Treated Steel, Metall. Mater. Trans. B. 54 (2014) 2813–2820. doi:10.2355/isijinternational.54.2813.

[99]   S. Sun, S. Waterfall, N. Strobl, D. Liao, D. Holdridge, Inclusion Control with Ca Treatment to Improve Castability of Low Carbon Aluminum-Killed Steel, in: J.-Y. Hwang, T. Jiang, M.W. Kennedy, O. Yücel, P.C. Pistorius, V. Seshadri, B. Zhao, D. Gregurek, E. Keskinkilic (Eds.), 8th Int. Symp. High-Temperature Metall. Process., Springer International Publishing, Cham, 2017: pp. 347–357.

[100] R. Tsujino, A. Tanaka, A. Imamura, D. Takahashi, S. Mizoguchi, Mechanism of Deposition of Inclusion and Metal in ZrO_2-CaO-C Immersion Nozzle of Continuous Casting, ISIJ Int. 34 (1994) 853–858. doi:10.2355/isijinternational.34.853.

[101] R.B. Tuttle, J.D. Smith, K.D. Peaslee, Interaction of alumina inclusions in steel with calcium-containing materials, Metall. Mater. Trans. B. 36 (2005) 885–892. doi:10.1007/s11663-005-0090-4.

[102] R.B. Tuttle, J.D. Smith, K.D. Peaslee, Casting Simulation of Calcium Titanate and Calcium Zirconate Nozzles for Continuous Casting of Aluminum-Killed Steels, Metall. Mater. Trans. B. 38 (2007) 101–108. doi:10.1007/s11663-006-0001-3.

[103] J.K.S. Svensson, F. Larsson, A. Memarpour, S. Ekerot, V. Brabie, P.G. Jönsson, Implementation of an YSZ coating material to prevent clogging of the submerged entry nozzle (SEN) during continuous casting of Ce-treated steels, Ironmak. Steelmak. 45 (2018) 105–113. doi:10.1080/03019233.2016.1245916.

[104] Y.H. Paik, H.C. Shin, J.M. Lee, Electrical charge of metal oxides in liquid metals, Met. Mater. 4 (1998) 995–1000. doi:10.1007/BF03025967.

[105] J. Yu, X. Yang, Z. Liu, X. Hou, Z. Yin, Anti-clogging of submerged entry nozzle through control of electrical characteristics, Ceram. Int. 43 (2017) 13025–13029. doi:https://doi.org/10.1016/j.ceramint.2017.06.133.

[106] X. Yang, J. Yu, Z. Liu, X. Hou, B. Ma, The charged characteristics of the submerged entry nozzle used for continuous casting, Ceram. Int. 43 (2017) 2881–2883. doi:https://doi.org/10.1016/j.ceramint.2016.11.012.

[107] W.-B. Dai, X.-L. Zhou, X. Yang, G.-P. Tang, D.-B. Jia, N.-L. Cheng, J.-K. Yu, Formation of Dense Inclusion Buildup on Submerged Entry Nozzle by Electric Current Pulse, Acta Metall. Sin. (English Lett. 29 (2016) 500–504. doi:10.1007/s40195-016-0418-x.

[108] C. Henry, J.-P.P. Minier, G. Lefèvre, Towards a description of particulate fouling: From single particle deposition to clogging, Adv. Colloid Interface Sci. 185–186 (2012) 34–76. doi:10.1016/j.cis.2012.10.001.

[109] E. Gutiérrez, S. Garcia-Hernandez, J. de J. Barreto, Mathematical Analysis of the Dynamic Effects on the Deposition of Alumina Inclusions inside the Upper Tundish Nozzle, ISIJ Int. 56 (2016) 1394–1403. doi:10.2355/isijinternational.ISIJINT-2016-076.

[110] E. Gutiérrez, S. Garcia-Hernandez, J. de Jesús Barreto, Mathematical Modeling of Inclusions Deposition at the Upper Tundish Nozzle and the Submerged Entry Nozzle, Steel Res. Int. 87 (2016) 1406–1416. doi:10.1002/srin.201500422.

[111] P. Ni, L.T.I. Jonsson, M. Ersson, P.G. Jönsson, On the deposition of particles in liquid metals onto vertical ceramic walls, Int. J. Multiph. Flow. 62 (2014) 152–160. doi:10.1016/j.ijmultiphaseflow.2014.02.002.

[112] P. Ni, L.T.I. Jonsson, M. Ersson, P.G. Jönsson, The Use of an Enhanced Eulerian Deposition Model to Investigate Nozzle Clogging During Continuous Casting of Steel, Metall. Mater. Trans. B. 45 (2014) 2414–2424. doi:10.1007/s11663-014-0145-5.

[113] D. Eskin, J. Ratulowski, K. Akbarzadeh, Modeling of particle deposition in a vertical turbulent pipe flow at a reduced probability of particle sticking to the wall, Chem. Eng. Sci. 66 (2011) 4561–4572. doi:10.1016/j.ces.2011.06.015.

[114] C. Caruyer, J.-P. Minier, M. Guingo, C. Henry, A stochastic model for particle deposition in turbulent flows and clogging effects, in: Adv. Hydroinformatics, Springer, 2016: pp. 597–612.

[115] C. Xuan, A. V. Karasev, P.G. Jönsson, K. Nakajima, Attraction Force Estimations of Al 2 O 3 Particle Agglomerations in the Melt, Steel Res. Int. 88 (2017) 1600090. doi:10.1002/srin.201600090.

[116] P. Ni, L.T.I. Jonsson, M. Ersson, P.G. Jönsson, Turbulent Flow Phenomena and Ce2O3 Behavior during a Steel Teeming Process, ISIJ Int. 53 (2013) 792–801. doi:10.2355/isijinternational.53.792.

[117] T. Schwarz, Heat transfer and fouling behaviour of Siemens PWR steam generators--long-term operating experience, Exp. Therm. Fluid Sci. 25 (2001) 319–327. doi:10.1016/S0894-1777(01)00080-2.

[118] M.S. Abd-Elhady, M.R. Malayeri, H. Müller-Steinhagen, Fouling Problems in Exhaust Gas Recirculation Coolers in the Automotive Industry, Heat Transf. Eng. 32 (2011) 248–257. doi:10.1080/01457632.2010.495612.

[119] I. Wilson, J. Chew, Fouling and cleaning in food processing 2010, Food Bioprod. Process. 88 (2010) 333–334. doi:10.1016/j.fbp.2010.11.011.

[120] L.D. Nghiem, S. Hawkes, Effects of membrane fouling on the nanofiltration of pharmaceutically active compounds (PhACs): Mechanisms and role of membrane pore size, Sep. Purif. Technol. 57 (2007) 176–184. doi:10.1016/j.seppur.2007.04.002.

[121] B. V Deraguin, L. Landau, Theory of the stability of strongly charged lyophobic sols and of the adhesion of strongly charged particles in solution of electrolytes, Acta Physicochim USSR. 14 (1941) 633–662.

[122] E.J.W. Verwey, J.T.G. Overbeek, K. van Nes, Theory of the Stability of Lyophobic Colloids: The Interaction of Sol Particles Having an Electric Double Layer, Elsevier Publishing Company, 1948. https://books.google.at/books?id=uEOMnQEACAAJ.

[123] F. Kuhnen, K. Barmettler, S. Bhattacharjee, M. Elimelech, R. Kretzschmar, Transport of Iron Oxide Colloids in Packed Quartz Sand Media: Monolayer and Multilayer Deposition, J. Colloid Interface Sci. 231 (2000) 32–41. doi:https://doi.org/10.1006/jcis.2000.7097.

[124] P. Bacchin, A. Marty, P. Duru, M. Meireles, P. Aimar, Colloidal surface interactions and membrane fouling: Investigations at pore scale, Adv. Colloid Interface Sci. 164 (2011) 2–11. doi:10.1016/j.cis.2010.10.005.

[125] L. Suresh, J.Y. Walz, Effect of Surface Roughness on the Interaction Energy between a Colloidal Sphere and a Flat Plate, J. Colloid Interface Sci. 183 (1996) 199–213.

doi:10.1006/jcis.1996.0535.

[126] E. Martines, L. Csaderova, H. Morgan, A.S.G. Curtis, M.O. Riehle, DLVO interaction energy between a sphere and a nano-patterned plate, Colloids Surfaces A Physicochem. Eng. Asp. 318 (2008) 45–52. doi:10.1016/j.colsurfa.2007.11.035.

[127] C. Henry, J.-P. Minier, G. Lefèvre, O. Hurisse, Numerical Study on the Deposition Rate of Hematite Particle on Polypropylene Walls: Role of Surface Roughness, Langmuir. 27 (2011) 4603–4612. doi:10.1021/la104488a.

[128] Z. Adamczyk, B. Siwek, M. Zembala, P. Belouschek, Kinetics of localized adsorption of colloid particles, Adv. Colloid Interface Sci. 48 (1994) 151–280. doi:10.1016/0001-8686(94)80008-1.

[129] R. V Magan, R. Sureshkumar, Multiscale-linking simulation of irreversible colloidal deposition in the presence of DLVO interactions, J. Colloid Interface Sci. 297 (2006) 389–406. doi:10.1016/j.jcis.2005.11.034.

[130] N. Filipovic, M. Kojic, A. Tsuda, Modelling thrombosis using dissipative particle dynamics method, Philos. Trans. R. Soc. A Math. Phys. Eng. Sci. 366 (2008) 3265–3279. doi:10.1098/rsta.2008.0097.

[131] C. Henry, J.P. Minier, Progress in particle resuspension from rough surfaces by turbulent flows, Prog. Energy Combust. Sci. 45 (2014) 1–53. doi:10.1016/j.pecs.2014.06.001.

[132] H. Friess, G. Yadigaroglu, Modelling of the resuspension of particle clusters from multilayer aerosol deposits with variable porosity, J. Aerosol Sci. 33 (2002) 883–906. doi:10.1016/S0021-8502(02)00049-6.

[133] M. Tregnaghi, A. Bottacin-Busolin, A. Marion, S. Tait, Stochastic determination of entrainment risk in uniformly sized sediment beds at low transport stages: 1. Theory, J. Geophys. Res. Earth Surf. 117 (2012) n/a-n/a. doi:10.1029/2011JF002134.

[134] M. Valyrakis, P. Diplas, C.L. Dancey, K. Greer, A.O. Celik, Role of instantaneous force magnitude and duration on particle entrainment, J. Geophys. Res. Earth Surf. 115 (2010). doi:10.1029/2008JF001247.

[135] F. Zhang, M.W. Reeks, M.P. Kissane, R.J. Perkins, Resuspension of small particles from multilayer deposits in turbulent boundary layers, J. Aerosol Sci. 66 (2013) 31–61. doi:10.1016/j.jaerosci.2013.07.009.

[136] K. Iimura, S. Watanabe, M. Suzuki, M. Hirota, K. Higashitani, Simulation of entrainment of agglomerates from plate surfaces by shear flows, Chem. Eng. Sci. 64 (2009) 1455–1461. doi:10.1016/j.ces.2008.10.070.

[137] ANSYS FLUENT 14.5 User's Guide, ANSYS, Inc, 2012.

[138] A. Soldati, C. Marchioli, Physics and modelling of turbulent particle deposition and entrainment: Review of a systematic study, Int. J. Multiph. Flow. 35 (2009) 827–839. doi:10.1016/j.ijmultiphaseflow.2009.02.016.

[139] M. Guingo, J.-P. Minier, A stochastic model of coherent structures for particle deposition in turbulent flows, Phys. Fluids. 20 (2008) 053303. doi:10.1063/1.2908934.

[140] J.-P. Minier, E. Peirano, The pdf approach to turbulent polydispersed two-phase flows, Phys. Rep. 352 (2001) 1–214. doi:10.1016/S0370-1573(01)00011-4.

[141] T. Adams, C. Grant, H. Watson, A Simple Algorithm to Relate Measured Surface

Roughness to Equivalent Sand-grain Roughness, Int. J. Mech. Eng. Mechatronics. 1 (2012) 66–71. doi:10.11159/ijmem.2012.008.

[142] E. Roos, A. Karasev, P.G. Jönsson, Effect of Si and Ce Contents on the Nozzle Clogging in a REM Alloyed Stainless Steel, Steel Res. Int. 86 (2015) 1279–1288. doi:10.1002/srin.201400344.

[143] X. Yang, T.J. Lu, T. Kim, An analytical model for permeability of isotropic porous media, Phys. Lett. Sect. A Gen. At. Solid State Phys. 378 (2014) 2308–2311. doi:10.1016/j.physleta.2014.06.002.

[144] N. Kojola, S. Ekerot, P. Jönsson, Pilot plant study of clogging rates in low carbon and stainless steel grades, Ironmak. Steelmak. 38 (2011) 81–89. doi:10.1179/030192310X12706364542704.

[145] K. Sasai, Y. Mizukami, Effect of Stirring on Oxidation Rate of Molten Steel, ISIJ Int. 36 (1996) 388–394. doi:10.2355/isijinternational.36.388.

[146] F.R. Menter, Two-equation eddy-viscosity turbulence models for engineering applications, AIAA J. 32 (1994) 1598–1605. doi:10.2514/3.12149.

[147] F.R. Menter, M. Kuntz, R. Langtry, Ten years of industrial experience with the SST turbulence model, Turbul. Heat Mass Transf. 4 (2003) 625–632.

[148] A. Jungreithmeier, E. Pissenberger, K. Burgstaller, J. Mortl, Production of ULC IF steel grades at Voestalpine Stahl GmbH, Linz., in: Iron Steel Soc. Int. Technol. Conf. Expo. 2003, 2003: pp. 227–240.

9. Publications

1. H. Barati, M. Wu, A. Kharicha, A. Ludwig, Assessment of Different Turbulence Models for the Motion of Non-metallic Inclusion in Induction Crucible Furnace, IOP Conf. Ser. Mater. Sci. Eng. 143 (2016) 12026.

2. H. Barati, M. Wu, A. Kharicha, A. Ludwig, A transient model for nozzle clogging, Powder Technol. 329 (2018) 181–198. doi:10.1016/j.powtec.2018.01.053.

3. H. Barati, M. Wu, T. Holzmann, A. Kharicha, A. Ludwig, Simulation of Non-metallic Inclusion Deposition and Clogging of Nozzle, in: L. Nastac, K. Pericleous, A.S. Sabau, L. Zhang, B.G. Thomas (Eds.), CFD Model. Simul. Mater. Process. 2018, Springer International Publishing, Cham, 2018: pp. 149–158.

4. H. Barati, M. Wu, A. Kharicha, A. Ludwig, Investigation on Mesh Sensitivity of a Transient Model for Nozzle Clogging, in: International Conference on Metallurgical and Materials Engineering, London, United Kingdom, 2018.

5. H. Barati, M. Wu, A. Kharicha, A. Ludwig, Discussion on possible solidification during SEN clogging in steel continuous casting, in: Solidification and Gravity VII, Miskolc-Lillafüred, Hungary, 2018.

6. H. Barati, M. Wu, A. Kharicha, A. Ludwig, Calculation accuracy and efficiency of a transient model for submerged entry nozzle clogging, Metall. Mater. Trans. B. (2018) Submitted.